SELF-ASSEMBLED NANO-PATTERNS BY GAS CLUSTER ION BEAM BOMBARDMENT

A Dissertation

Presented to

the Faculty of the Department of Physics

University of Houston

In Partial Fulfillment

of the Requirements for the Degree

Doctor of Philosophy

By

Buddhi Prasanga Tilakaratne

December, 2012

SELF-ASSEMBLED NANO-PATTERNS BY GAS CLUSTER ION BEAM BOMBARDMENT

Buddhi Prasanga Tilakaratne

APPROVED:

Dr. Wei-Kan Chu, Chairman

Dr. Gemunu H. Gunaratne

Dr. James K. Meen

Dr. John H. Miller

Dr. Haibing Peng

Dr. Mark A. Smith, Dean
Dean, College of Natural Sciences and Mathematics

Acknowledgments

I would like to express my deep gratitude to my advisor; Dr. Wei-Kan Chu for his patient guidance, enthusiastic encouragement, valuable support and critiques of this research work. I am also grateful to my dissertation commit members, Dr. Gemunu Gunaratne, Dr. James Meen, Dr. John Miller, and Dr. Haibing Peng for their guidance. Additionally, I would like to thank my group members; Dr. Quark Chen, Dr. Dharshana Wijesundera, Dr. Ananta Adhikari, Babu Bhandari, and Huy Dinh for their experimental suggestions and support. I thank Xuemei Wang for technical support and excellent training sessions during my dissertation work.

I am grateful to late Dr. Ki Ma for his unconventional research questions and guidance during my early days at the ion beam laboratory.

I wish to thank Dr. John Baglin, Dr. Jiming Bao, Dr. Stephan Garoff, and Dr. Fernanda Laezza for sharing their expertise and for their collaboration. I would also like to extend my thanks to Dr. Robert Bradley and Dr. Shivakumar Bhaskaran of the Nano Fabrication Facility at University of Houston for his help in offering me technical support in the scanning electron microscope and profilometer measurements. I am grateful to Dr. Gila Stein for permitting me to use her contact angle goniometer instrument.

I would like to extend my sincere gratitude to Dr. Riznia Jasim, Dr. Thiloshana Ranawaka, Dr. Upali Karunasiri, Dr. Indika Wallimuni, Dr. Milinda Abeykoon, Manori Gunasekera, and Deepal Weerasinghe. They helped me considerably.

Last but not least, I wish to extend my deepest gratitude to my parents, my brother Kamal and sister-in-law Sushama, and my sisters Thusharika and Udeshika for their love, encouragement, and unconditional support to overcome many challenges put before me. I dedicate this dissertation to my parents. Thank you for believing in me and guiding me through every step since the day I was born.

SELF-ASSEMBLED NANO-PATTERNS BY GAS CLUSTER ION BEAM BOMBARDMENT

An Abstract of a Dissertation

Presented to

the Faculty of the Department of Physics

University of Houston

In Partial Fulfillment

of the Requirements for the Degree

Doctor of Philosophy

By

Buddhi Prasanga Tilakaratne

December, 2012

Abstract

Morphological evolution of surfaces during the course of off-normal cluster ion beam bombardment is investigated. The objective is to realize the Ar cluster ion-induced self-assembled ripple shaped nano-pattern formation process on Si and Au surfaces. During cluster ion beam bombardment, surface atoms undergo three processes: (1) continuous sputtering into the vacuum due to high energy collisions, (2) initial re-deposition of atoms, and (3) surface diffusion of atoms.

The first process is an independent of applied dosage, thus carries a minimum impact on nano-ripple pattern formation. In the second process, atoms deposit close to the collision site, which acts as a barrier for the next set of sputtering atoms. Even though this starts to develop ripples, ripples become well-ordered and grow due to surface diffusion and upstream sputtering of atoms.

This investigation reveals that cluster ion-induced nano-ripple formation saturates comparatively sooner than that induced by monomer ions. Continuous bombardment creates sand dune-like nano-structures on the Si surfaces at 60^{o} angle of incidence measured from the surface normal. However, at a grazing incidence, surface becomes smooth. Further investigation on Au surfaces conform the above mentioned three-step process of nano-ripple formation. Additionally, it was found that these nano-rippled surfaces show anisotropic properties, which are useful in directional surface wetting and surface plasmonic applications.

Contents

List of Figures

List of Tables

Chapter 1

Introduction

Ion beam modification and synthesis of materials to transform the surface properties has introduced diverse applications in semiconductor, surface engineering and bio-medical industries. Ultra-shallow implantation and processing of smooth surfaces are important applications in semiconductor device fabrications. Additionally, engineering frictionless surfaces or roughening the surface provides cutting-edge technologies for machines scaling from macro to nano dimensions. Tunable surface nano-patterning allows macro molecules to adsorb onto the surface. Ion beam techniques provide precision, elemental and compound beams and the ability to modify a wide range of materials. Nano-patterning requires significant surface alterations, which are pre-dominantly caused by nuclear collision between ions and substrate atoms in less than 100 eV energy range. However, for a monomer ion beam extraction of a low energy beam is difficult due to space charge effect. This can be compensated by using a cluster ion beam. The capacity

to control current density, energy and size of clusters is important in creating micro-nano scale patterns. However, a considerable amount of research work must be done before commercialization of cluster ion patterned surfaces. In this dissertation I put forward a substantial amount of experimental results on semiconductor and metallic surfaces to build a fundamental understanding of cluster ion-induced surface patterns.

Cluster ions can be classified according to common ion beam terminologies by considering the energy per atom before the impact with the target substrate [1, 2]. Cluster ions having energies < 1 eV/atom, in thermal range, do not penetrate the surface and atoms in the cluster adsorb on the surface [3, 4]. In the 1-100 eV/atom energy range (Hyper thermal range) cluster ions interact with surface and sub-surface atoms [5, 6], and in the 100 eV-500 keV/atom medium energy range clusters penetrate the surface and large surface craters are formed and the dominant stopping mechanism is the nuclear stopping power [7]. Cluster ions with energies beyond 500 keV/atom are called swift cluster ions which penetrate deep into the target and electronic stopping power becomes dominant [8].

Emergence of gas cluster ion beam systems was an essence of surface modification research because of their capability to deliver low energy atoms with high beam current density and low charge per cluster. Designs and development of a Gas Cluster Ion Beam (GCIB) system was first done by Yamada and co-workers [9] in early 1990s. GCIB research and development has flourished in the past two decades as an industrial tool for surface smoothing, etching of semiconductor [5, 10], ultra-shallow chemical modification of materials for device fabrication [11], processing of surfaces for bio-medical implants

[12], and high sputtering yield applications in Secondary Ion Mass Spectroscopy analysis [13]. Cluster ion interactions with surface generate unique structural modifications compared to monomer ion beams, where cluster ions simultaneously arrive at the same location and disassociations close to the surface create synergetic reactions. This dissertation mainly focuses on clusters having energies in the hyper thermal range with few thousands of gaseous atoms and their effects on surfaces while bombarded at an off-normal angle at room temperature and also will include a brief description of temperature dependence of surface patterns. Gaseous large clusters with atoms carrying 10 eV/atom energies generate massive amounts of energy density proximate to the surface creating excessive modifications. Impact of a cluster ion produces a 10^4 K instantaneous temperature pulse [14], but the overall surface temperature remains stable at room temperature. In addition, a cluster ion with surface normal trajectory sputters target surface atoms parallel to the measured surface (lateral sputtering). Clusters initially sputter target surface peaks and fills in trenches, which smooth the surface and with persistent bombardment, surface atomic layers start to peel out already smoothed surface continuously. For examples, Chu, et al. [5] have tested gas cluster ion beam on $YBa_2Cu_3O_{7-\delta}$ (YBCO) high temperature superconducting thin film surfaces to smooth the uneven surface formed due to nucleation and growth during the deposition process [Figure 1(a)]. The YBCO surface smoothed from 13 nm to 0.8 nm with a 2×10^{16} clusters/cm^2 dose at 6.7 eV per atom energy and about Ar 3000 atoms in a cluster [Figure 1(b)]. However, cluster ions amorphize the surface of YBCO, but the crystalline structure can be recovered by thermal annealing or removed by chemical etching treatment [5].

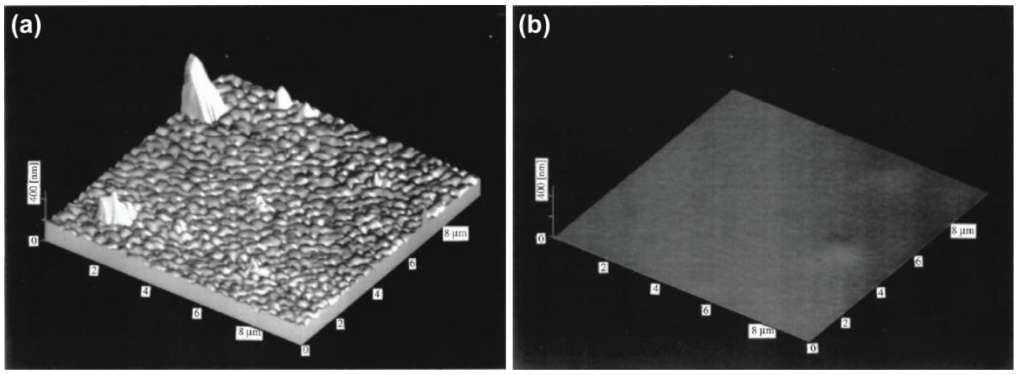

Figure 1.1: The atomic force microscope (AFM) image of a 900 nm thick YBCO sample. The scan area is 10μm with a height scale of 400 nm. (a) Non-bombarded surface with standard deviation of roughness of 13 nm, and (b) Ar cluster ion beam bombarded at 2×10^{16} clusters/cm^2 dosage normal to the surface the final surface standard deviation roughness was 0.8 nm.

Also most recent research activities that involved gas cluster ions conducted at University of Houston include smoothing of strain relaxed $Si_{0.7}Ge_{0.3}$ surface, which had cross-hatched patterns due to growth. These substrates were considered prospects for fabrication of high performance strained Metal Oxide Semiconductor Field Effect Transistors (MOSFET). Cluster ions with 10 eV/atom energy and 3000 Ar atoms smooth the $Si_{0.7}Ge_{0.3}$ surface to 0.7 nm [15]. Other interesting research involving cluster ions was to deposit C_{60} while continuously bombarding the deposited film at normal incidence to transform C_{60} film into diamond-like thin films [16].

In contrast, off-normal cluster ion beam surface interactions generate anisotropic surface patterns beyond a critical incident angle from the surface normal. Surface atoms attain forward momentum caused by synergetic reactions of cluster ions [17]. In the course of this surface atomic mass flow, patterns are generated depending on the angle of

incidence, energy and dose of the cluster ion, and on the surface material.

Despite extensive examinations carried out on GCIB surface smoothing processes, a good understanding of surface pattern formation is lacking. The purpose of this research study is to investigate pattern formation on surfaces experimentally using Ar cluster ion beam, and to investigate possible applications of these nano-structured surfaces. In Chapter 2 I will describe patterns found in nature and explain similarities of these patterns to nano scale structures seen on material surfaces. Also I will cover monomer ion sputtering and ripple formation models with an experimental briefing of monomer ion surface patterns.

In Chapter 3, I will briefly review different cluster ion beam forming technologies and explicitly I will describe the GCIB technology that was used in this dissertation study: Large argon clusters via gas cluster ion beam system, stagnated high pressure monoatomic gas adiabatically convert into clusters and transported through a small skimmer, which are then ionized by a cloud of electrons and accelerated toward a target with maximum energy of 30 keV per cluster.

Chapter 4 covers the experimental analysis techniques used to characterize cluster ion beam modified surfaces and thin films. Rutherford Backscattering Spectroscopy (RBS) provides a unique non-destructive technique to acquire information from a material; composition, thin film thickness, crystallinity and deformations are some examples. The surface alteration created by clusters can be mapped via Atomic Force Microscopy (AFM). AFM data provide information regarding surface roughness, and wavelength of surface patterns. I will also explain a second technique used to profile surface, specifically for bulk materials. Other techniques that I have been using include Scanning

Electron Microscopy (SEM), X-ray Photoelectron Spectroscopy (XPS), and also to determine applications of cluster modified materials contact angle goniometer, surface resonance plasmon were used. Results obtained from these techniques are discussed in Chapters 5 and 6.

Chapter 5 will include a discussion on pattern formation on silicon during large cluster ion beam bombardment, and compare these results to monomer ion-induced ripples on silicon. The cluster ion beam formed ripples ignores surface crystallinity since the cluster ion impact amorphizes the surface and ripples are formed on top of this amorphous layer. Intriguingly, prolonged bombardment on the silicon surface produces sand dune like structures on the surface. I will also discuss the recovery process of amorphized silicon surface by annealing and its impact on ripples pattern.

Chapter 6 covers the large gas cluster beam bombardment of gold (Au). I observed Au surfaces have a unique cluster ion incident angle for generating high surface nano-ripples. Surface sputtering and roughness variations with cluster ion incident angle, dose and energy show three processes that occur during ripple formation. GCIB produces high aspect ratio structures with applied dose. Nano-ripple structure formation provides an inexpensive technique that can be applied in many surface engineering industries. Furthermore, I will discuss the complexity associated with high dose bombardment and importance of surface element atomic mass and surface binding energy in ripple formation. Also I will discuss the maximum surface instability with cluster ion beam angle of incidence and surface geometrical shadowing process with bombardment time.

In chapter 7 I will discuss two exemplary applications of nano-ripples. Au nano-ripple

height, width, length, and well-orderedness produce unique surface wetting properties. Wetting is expressed in terms of contact angle, which is the angle between solid-liquid and liquid-vapor interfaces. I will discuss hydrophobic-hydrophilic interactions of nano-ripple surfaces and dependence of contact angle on surface roughness. I will also discuss anisotropic effects of these one-dimensional nano-ripples. Furthermore, I will discuss surface plasmon resonance effects of Au nano-ripples for different Ar-cluster ion beam bombardment conditions.

In Chapter 8 I will conclude the results of this research study and discuss future directions that are needed to be taken to produce unique surface patterns and to study multi element substrates.

Chapter 2

Background

2.1 Pattern Formation in Nature

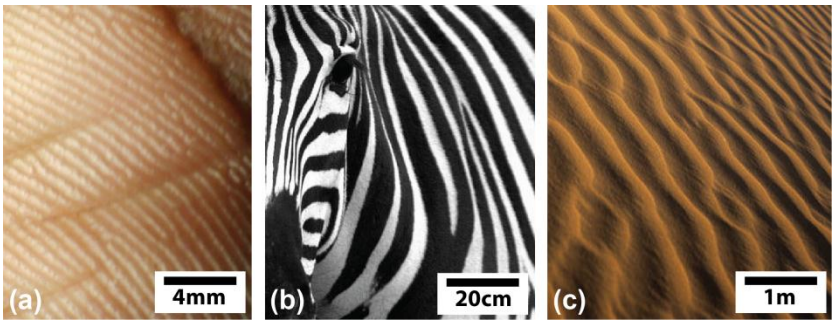

Figure 2.1: Patterns in nature resembling ripples (a) Lines on a palm of a hand, (b) Strips on a zebra skin, and (c) Aeolian sand ripples in a desert.

Ripple pattern formation on a surface observed in nano scale can be seen also in macroscopic scale. This universality of pattern formation can be used to deliberate nano-

ripple formations on material surfaces. For many years pattern formation in nature has brought amazement not only to the public eye but also to the scientific. Figures 2.1 (a) and (b) show a surface pattern of a human palm and (c) strips on a zebra respectively, both exhibit biological processes formed in entirely different chemical and biological methods, but in a more general point of view, we can observe similarities in these patterns, order, pattern dislocations and discontinuities to name a few. Figure 2.1 (c) shows an aeolian sand ripple pattern formed due to wind, these types of patterns is usually formed on deserts and sandy beaches. The universality occurs in pattern formation due to dynamical properties of a system, independent of whether the system is physical, chemical or biological. One example that is beneficial in understanding nano-pattern formation is the sand ripple formation. The behavior of sand under wind erosion conditions have been studied for over eighty years. Sand ripple and dune formation was first experimentally studied and modeled by R. A. Bagnold in 1931 [18]. In his early model, ripple-forming sand were dubbed “singing sand”. That is ripples are formed by sound waves generated by rapid vibration of top dry sand layers due to an external force, but later this model was dropped due to lack of clarification in merger and coarsening of ripples [19].

The most available explanation on aeolian sand ripple formation is that individual loose sand grains elevate with the wind and go into suspension before becoming heavy for the wind to hold up, and it deposits on the surface. Since these grains obtain potential energy as well as kinetic energy from wind during suspension, and they eject more sand grains when colliding with the surface [20]. The sand grains that initially eject due to wind are

called saltation grains and grains that eject with less energy due to saltation grain collisions are known as the reptation grains. Furthermore, some sand grains go through a creeping (rolling) process due to very low energy collisions. Saltation is maintained by the amount of grains that the wind carries per given time, and the energy gained while lifting from the sand bed [21]. Mitha et al. showed that sand grains' collision process can be illustrated by impacts of high speed steel spheres at an angle. Sphere impacts and secondary projection of spheres from the surface covered with similar spheres showed there were about eight projectiles formed during a single collision. The number of secondary projectiles depended on the speeds and angles of impacting spheres [22]. In 1987, R. S. Anderson introduced a model based on sand ripple experimental observations and Mitha's work, where he explained that saltation grains gain momentum and direction from wind and act as projectiles that collide with the surface and eject secondary grains, which hop into a different location. These hopping grains accumulate and become sources of aeolian sand ripples on sand beds [23].

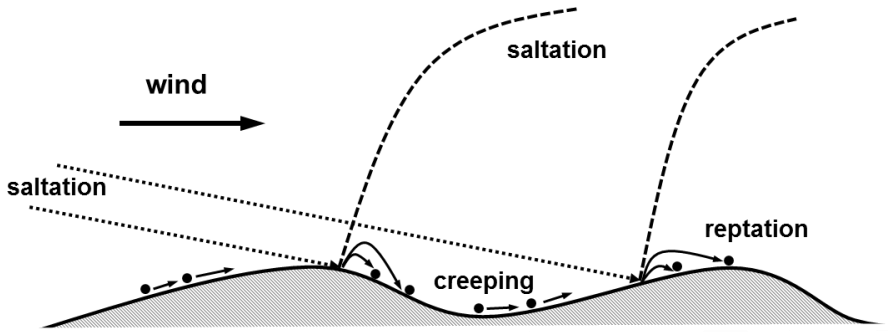

Figure 2.2: Sand grains elevate into suspension due to wind, and when the wind loses its grip on these grains, it dumps them back onto the surface. These sand grains known as saltation grains act as projectiles and upon colliding with the surface (sand bed) eject secondary grains. Some of these secondary grains go back into suspension and other; ejected with low energy, hop into a new location. These are called reptation sand grains and also grains creep along the surface. Alignment ripples depend on the wind direction [24].

Saltation, reptation, and creeping of sand grains can be related to cluster ion-induced ripple formation processes as described above and Anderson's aeolian sand ripple formation formulism and a hydrodynamic approach can be adapted to describe nano-ripple formation on material surfaces.

2.2 Ion – Solid Interaction

An ion bombarding a target material undergoes various processes depending on the ion energy, mass, and angle of incidence, which include penetration into the material, displacement of target material, backscattering, and adsorption on the surface. Ion target collision and subsequent stopping of the ion in the material is classified according to two types of energy loss: (1) electronic and (2) nuclear energy loss [25, 26]. Ions with medium energy and higher (>10 keV) interact inelastically with the target and lose energy by electronic excitation. Nuclear energy loss occurs due to ion surface atom elastic collisions and kinetic energy transfer into the material from the colliding ion. For metal and semiconductor materials, when atoms displace due to elastic collision, an interstitial atom and a vacancy is produced; these are called Frenkel pairs. If an ion has hyper-thermal energy (1 – 100 eV) the main energy loss mechanism is nuclear energy loss.

2.3 Brief Description of Surface Patterns Induced by Monomer Ion Bombardment

Surface self-assembled patterns due to monomer ion bombardment have been studied for nearly five decades. The first self-assembled pattern formation study was done by Navez et al. in 1962 [27]; the main observed patterns were ripples. They modified a glass surface by a charged beam of air with 4 keV energy and found that when the angle of incidence of the beam shifts from surface normal to grazing angles, the ripple orientation changed from perpendicular to parallel to the direction of the beam. The ripple formation and mechanism behind the process was not speculated on until decades later when Bradley and Harper first derived a model for ripple formation on solid materials [28].

In recent years the researches on ripples and other self-assembled surface have increased due to nano-scale applications. Experimental observations of monomer ion-induced nano structures are discussed extensively [29-34] and this dissertation will be limited to available theoretical model descriptions on ripple formation. In Chapter 5 I will cover a discussion of experimental comparisons between monomer and gas cluster ion-induced ripples. The Appendix A of this dissertation includes the Bradley and Harper model [28], the Makeev, Cuerno, and Barabási extended, Bradley and Harper Model [30], the Ehrlich-Schwoebel instability and the diffusional roughening model for temporal variations of ripples on crystalline metals [32, 35], the geometrical shadowing effect based model, which considers shadowing of ions by surface ripple geometries [36], and finally discuss the Muñoz-Garcia, Castro, and Cuerno hydrodynamic model [37].

2.4 Gas Cluster Ions vs. Monomer Ions

The sputtering phenomenon was first observed in a laboratory experiment by Grove [38] in 1853. The sputtering-induced surface instability depends on the ion beam angle of incidence, energy and mass of ion, applied dose, and material. Directional ion bombardment generates ripple patterns on a surface. The amplitude of these surface features shows an initial linear variation with applied dose, but after a critical dose, amplitude to wavelength ratio maximizes which causes saturation of ripple amplitudes. Monomer ion-induced self-assembled nano-pattern formation experimental investigations have been conducted in medium energy (100 eV < E < 10 keV's) and high dose ranges from ~10^{18} to 10^{22} ions/cm^2 and in general the maximum surface instabilities for monomer ions appear between 50^o to 70^o from the surface normal for metal and semiconductor materials [29-34], but there are some contradictory observations reported by Ziberi et al. [39,40], where ripples form at an incidence angle of 20^o and then again surface roughening at 60^o to 80^o. Medium energy monomer ions penetrate the solid surface and undergo collision cascade events and surface sputtering occurs when an atom gains sufficient energy from an energetic nearest neighbor atom to overcome the surface binding energy barrier of the material [28, 30].

However, gas cluster ions consisting of hundreds to thousands of atoms with very low energies, a few eV's, generate high energy density collisions at the surface and sputter large amount of atoms. Gas cluster ions formed due to condensation are held together by van der Waal forces. Formation and instrumentation of large gas cluster ions are discussed in detail in Chapter 3. Moreover, the cluster ion sputtering rate shows linear

variation with applied cluster ion energy [17], whereas monomer ion momentum conservation creates a square root of energy deviation. Time-evolution Monte Carlo simulation calculations done by Yamamura [41] suggest three interior processes within a gas cluster ion at the moment of impact normal to the surface. (1) Highly packed first in row atoms backscatter after the impact; (2) These backscattering atoms interact with interior cluster atoms and produce parallel velocity components; and (3) Atoms move laterally and interact with peaks and smoothed the surface. Since the total energy of a cluster ion is conserved, Toyoda et al. from experimental observations interpreted that atoms within a cluster ion undergo inelastic collisions resulting in atom-atom bond breaking in a cluster which produces synergism [42]. Figure 2.3 shows the angular distribution of sputtered Cu atoms due to normal incident monomer Ar^+ ions at 20 keV energy and Ar_{2000} cluster ions at 10 keV and 20 keV energies at 1×10^{17} clusters/cm^2 dosage [43]. Monomer ion sputtering shows a cosine law distribution, whereas clusters produce flatter lateral sputtering distribution. Furthermore, when cluster ions are incident at 60^o from the normal, surface atoms sputter forward in the direction of cluster ion impact (figure 2.4). These advancing atoms contribute to the surface roughening process. Nevertheless, the spatiotemporal evolution of advancing surface atoms and nano-structure (ripple patterns) formation due to off-normal cluster ion bombardment has not been researched extensively. In this dissertation, the author discusses the evolution of ripples formed on silicon and gold surfaces.

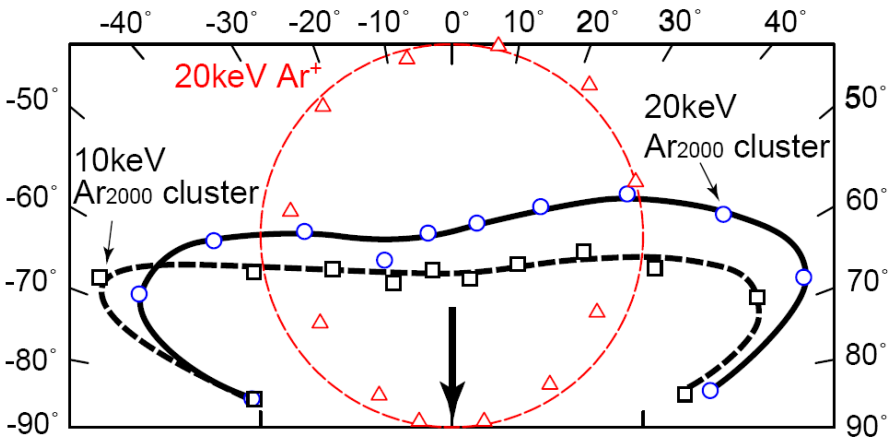

Figure 2.3: Angular distributions of sputtered Cu atoms due to monomer Ar^+ ions at 20 keV energy and Ar_{2000} cluster ions at 10 keV and 20 keV energies bombarded normal to the surface. [43].

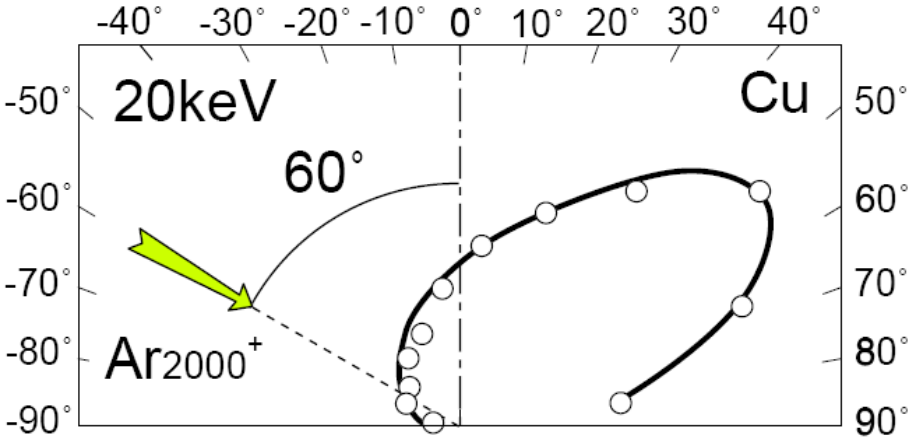

Figure 2.4: Angular distribution of atoms sputtered by Ar cluster ions at several incident angles. The average cluster size and acceleration energy are 2000 atoms/cluster and 20 keV, respectively [43].

Chapter 3

Gas Cluster Ion Beam (GCIB) System

This chapter is an introduction to types of cluster ion-forming techniques and a detailed description of GCIB System.

3.1 Cluster Ion Sources

Clusters of gaseous and metal atoms can be acquired through an expanding nozzle flow with necessary conditions. The first such discovery of clusters was conducted by Becker et al. in 1956 by studying condensation of individual vapor expanding out of a small nozzle into a vacuum and the cluster ion beam was detected via a modified ion gauge [44]. Cluster ions may take the form of dimers, molecules or large cluster up to about 10 nm in diameter with thousands of atoms. The characteristic properties of cluster ion include segregation of atoms more closely to the surface and they are loosely bonded

compared to inner atoms and give rise to different interactions with materials compared to monomer ions. One important aspect of cluster ion beams is their beam intensities and the specific charge effect. Low specific charge is desired to obtain a high beam current for energies ranging up to 10 keV/atom [45], with comparison of current and charge density. The use of cluster ions with specific size ***N/Z*** increases mass current and density by a factor of ***N/Z***, where ***N*** is the number of atoms in the cluster, and ***Z*** is the atomic number of the cluster ion element. Also heavy clusters have limited space charge effects. There are various types of cluster ion forming sources that vary depending on the need of the research on hand.

(a) *Supersonic Expansion*

A high pressure gas expands into a vacuum through a de Laval nozzle (an asymmetric hour glass-shape tube that is squeezed in the middle) creating an adiabatic expansion of the gas by limiting the velocity of the gaseous atoms which condense and form clusters. The temperature of the clusters is less than 10 K and large gaseous clusters are bonded with weaker van der Waals forces [17]. Then these clusters which pass through a metal skimmer are ionized by speeding electrons generated from a heated tungsten filament. When clusters are charged, they are mass selected and accelerated into a target chamber. A detailed description of the instrumentation of this cluster ion source will be discussed in section 3.2.

(b) *Source of Negative Ion Cesium Sputtering (SNICS)*

A negatively biased target material is sputtered by positive cesium ion and negative target ions are extracted and focused onto the sample chamber [46]. During the target

sputtering process polyatomic clusters are also formed due to the high reactivity of cesium ions, with an adjustable extraction voltage these clusters can be acquired and accelerated.

(c) *Laser Ablation*

A metal is vaporized by a laser beam and the vapor is carried out by high density helium gas through a nozzle where the gas undergoes supersonic expansion, and cools and condenses to form metal clusters [47]. All metal clusters produced are accelerated to the same speed by the helium carrier gas when exiting the nozzle. Early experiments done by Dietz et al. show that for a Al vaporization clustering process, the production of Al_2 dimer and Al_3 trimer signals possess 10% and 5% of the monomer signal.

(d) *Discharge Source*

A pulsed high current arc is placed between two electrodes in a pulse of carrier gas, which output the budding plasma through a channel and a conical nozzle into the high vacuum [48]. Ionized particles act as condensation sites for metal cluster ion growth.

(e) *Gas Aggregation*

Clusters are formed by nucleation from a metal vapor in a helium gas atmosphere covered by liquid nitrogen cooling chamber [49]. The neutral cluster beam is extracted through a small orifice. Cluster size ranges from 2 to 500 atoms per cluster depending on the metallic element.

(f) *Liquid Clusters*

A liquid is vaporized by resistive heating of the source. For ethanol room temperature

pressure is about 5.9 N/m^2, but pressure increases with source temperature [50]. Similar to the process described in 3.1 (a), vaporized liquid expands when passed through a nozzle whereby an adiabatic process vapor condenses and produces neutral clusters; helium gas is used as the cooling agent of the vapor during the clustering process. These clusters are ionized by electron bombardment.

3.2 Cluster Ion Formation in GCIB System

3.2.1 Supersonic Jet Nozzle

Figure 3.1 is a Gas Cluster Ion Beam (GCIB) system schematic diagram. In the nozzle chamber stagnated high pressure (P_o) gas at T_o temperature expands through a small hole of diameter D. Due to adiabatic expansion, highly randomized gas passes into the vacuum with similar speeds and at very low temperatures. The nozzle is a vital part of the GCIB since its structure controls the gas flow, cluster size, beam divergence and temperature. For the expansion, the energy conservation law can be applied by considering the enthalpy in the stagnation region (H_o) and in the vacuum region energy transfers into rest enthalpy and kinetic energy of the flow of gas which gives [51]

$$H_o = H + \frac{1}{2}mv^2 = c_pT + \frac{1}{2}mv^2 = c_pT_o \tag{3.1}$$

here c_p is the specific heat at constant pressure with a value of $\frac{5}{2}k$ for a monoatomic beam, and the flow region temperature is T. Also the Boltzmann constant is given by equation,

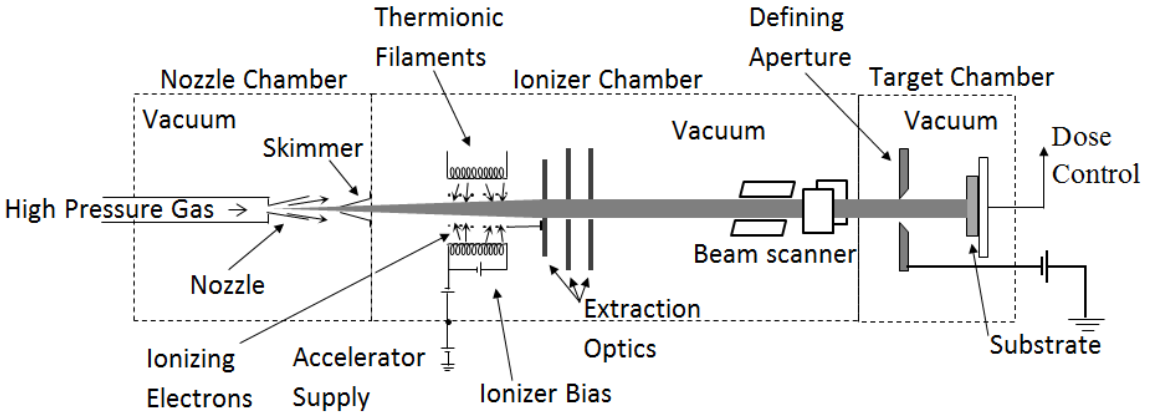

Figure 3.1: The schematic diagram of the Gas Cluster Ion Beam (GCIB) system in Texas Center for Superconductivity at University of Houston. The system is divided into three main chambers: Nozzle, Ionizer, and Target chamber. Inside the nozzle chamber, the stagnated high pressure gas expand adiabatically to form clusters which are then ionized and accelerated in the ionizer chamber and the cluster ion beam is focused and scanned onto the sample which is located inside the target chamber.

$$k = c_p - c_v \tag{3.2}$$

the equation (3.1) can be re-written as,

$$T = T_o\left[1 + \frac{1}{2}(\gamma - 1)M^2\right]^{-1} \tag{3.3}$$

where the ratio of the specific heats $\left(\gamma = {}^{c_p}/_{c_v}\right)$ at constant pressure and volume is assumed to be independent of temperature for a monoatomic gas and the Mach number (M) is the ratio of the stream velocity (v) to the local speed of sound $\left(c = \sqrt{{}^{\gamma kT}/_{m}}\right)$.

The M increases dramatically in the zone of silence (the region that is confined by the shock boundary as shown in Figure 3.2) and is given by

$$M = Q\left(\frac{d}{D}\right)^{\gamma-1} \tag{3.4}$$

where Q is a constant that for an atomic beam is 3.26 and d is a length from the nozzle throat. The behavior of M can be determined for different $^{d}/_{D}$ values for monoatomic (with three degrees of freedom, $\gamma = {}^{5}/_{3}$) and diatomic gases (with five degrees of freedom, $\gamma = {}^{7}/_{5}$), and the variations are shown in Figure 3.3. The curves indicate that for monoatomic gas the M increases in a short distance from the nozzle throat compared to diatomic gas. Thus the distance between the nozzle throat and skimmer orifice and the high pressure and low temperature in the stagnation region is important in extracting the required intense cluster ion beam current. Also the distance must be set such that the skimmer orifice is located in the molecular flow region of the supersonic expansion. The distance (d) is usually set to 3 cm. For this study a conical nozzle with 0.075 mm diameter was used and the gas flow rate was 330 sccm.

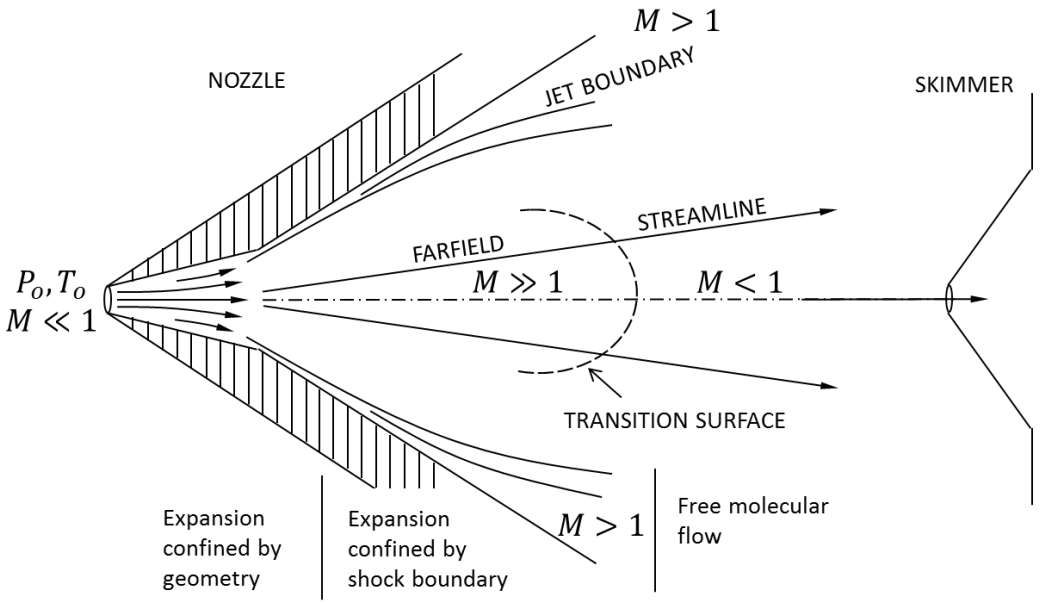

Figure 3.2: The cross section of a nozzle and a skimmer, and apparent expansion of an inert gas transitioning from monoatomic state to a molecular flow (The dash line indicates the transition boundary). Mach number (M) is very high just after expanding through the nozzle [52]

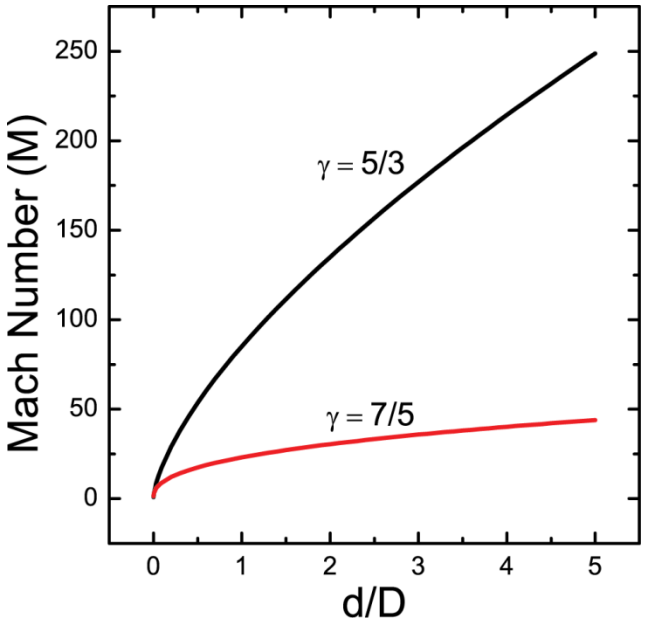

Figure 3.3: Mach number variation with distance between nozzle throat and skimmer orifice divided by nozzle throat diameter (0.075 mm) for monoatomic gas with three degree of freedom and for diatomic gas with 5 degree of freedom [53].

3.2.2 Cluster Formation

Supersonic expansion prompted cluster formation is a complicated process and there are limited theoretical explanations. Nevertheless if the local temperature is less than that of the binding energy of a dimer of gas atoms, clusters form, in the transition region from the zone of silence to molecular flow as shown in Figure 3.2, according to the following equation [54],

$$Ar + Ar + Ar \quad \rightarrow \quad Ar + Ar_2 \tag{3.5}$$

Formed dimers act as the condensation nuclei for cluster growth by inclusion of monomer atoms. Cluster growth is fueled by increased kinetic energy of monomer ions during dimer formation, since the energy in the process given by equation (3.5) is conserved. In addition, cluster – cluster aggregation becomes more prominent if there are a large number of clusters.

The formation of clusters can also be explained by considering condensation theory. Figure 3.4 shows the supersonic expansion of a condensing gas phase diagram. Point *A* represents high pressure stagnated condition, and during adiabatic expansion the gas at point *B* crosses $P_v(T)$ vapor pressure curve and gas expands further leading to an unstable state or super-saturation causing the gas to divert from the adiabatic process at point *C* and form clusters by homogeneous nucleation, and move back to the vapor pressure curve. The divergence at point *C* depends on the thermodynamics and on the kinetics and the time scale of the expansion, which are determined by the geometry of the nozzle and high pressure stagnation [55].

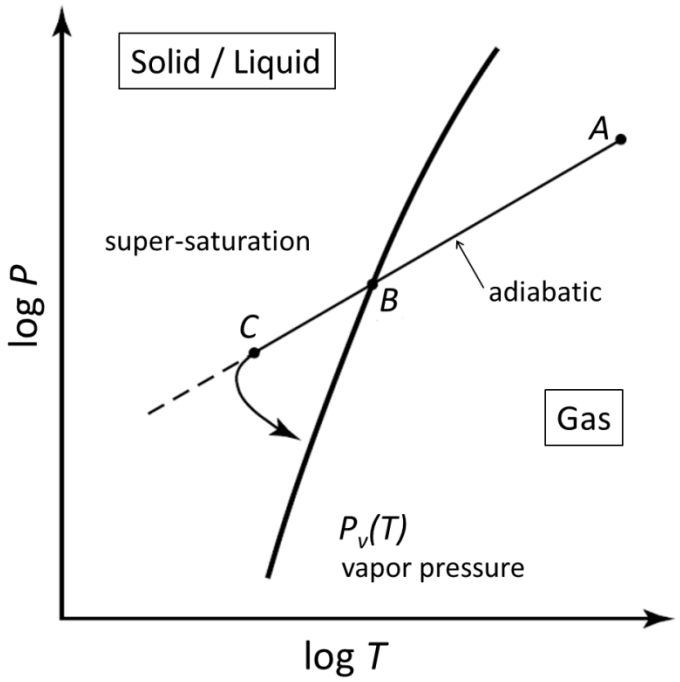

Figure 3.4: Phase diagram of the gas flow in supersonic expansion. Point ***A*** represents high pressure stagnated condition, and during adiabatic expansion, the gas at point ***B*** crosses $P_v(T)$ vapor pressure curve, and gas expands further leading to an unstable state or super-saturation causing the gas to divert from the adiabatic process at point ***C*** and re-attain the vapor pressure curve. The curve is in a double-log coordinate system [55]

The relationship between the vapor pressure $P_v(T)$ and the radius (r) of a cluster is given by

$$\ln \frac{P_r(T)}{P_0(T)} = \frac{2\sigma m}{kT\rho} \cdot \frac{1}{r} \tag{3.6}$$

where ρ, σ, and m are the density, the surface tension, and atomic weight of the cluster, respectively and k is the Boltzmann constant. For larger clusters the vapor pressure is low. Cluster ion growth depends on a critical value of the radius of the cluster and if the radius is below the critical clusters evaporate into the vacuum.

3.2.3 Metal Skimmer

The cores of the neutral clusters pass through a small orifice of the skimmer and the intensity of the cluster beam depends on the distance (*d*) between the nozzle and the skimmer orifice. The skimmer that is used is made out of nickel (Ni) and has a shape of a cone and also the diameter of the orifice used in this study was 0.075 mm. If d is larger than an optimal value a shock wave called Mach disk is formed in front of the skimmer which causes a decrease in the beam intensity [56]. Another issue that arises is that cluster beam interference due to evaporating gas collisions with clusters. Thus, including a high pumping rate turbo pump reduces the distortion by evaporating gas.

3.2.4 Cluster Ionization and Acceleration

Neutral clusters entering the ionizer chamber through the skimmer are ionized by electrons, which is convenient in extracting an intense current cluster ion beam. Photons are also a possible candidate for ionization and they produce a clear energy balance, but the beam current is lower than that of electron ionized cluster ion beam current [17]. The initial acceleration of cluster ions is provided by two-stage extraction voltages. The ionization beam includes clusters as well as monomer ions, and to suppress monomer ions via the space charge effect, a low extraction voltage is applied initially, and only large cluster ions with higher initial kinetic energies are extracted. Extracted cluster ions are focused by three electrostatic lenses. The cluster ion size distribution can be selected through applying a voltage across a retarding electrode located beam downstream from

the lenses. Also the cluster size distribution and beam intensity changes with the stagnation pressure (P_o). Figure 3.5 shows a time of fight mass spectrum of large cluster sizes at different P_o values [57]. The GCIB system that was used in this study can be used to produce maximum of 30 keV energy cluster ions with a biasing acceleration voltage of 30 kV. To achieve uniformity in the cluster ion beam, x-y scanners (deflectors) are activated. Experimental manipulation of the cluster ion beam for different target materials will be described in Chapters 5, 6 and 7.

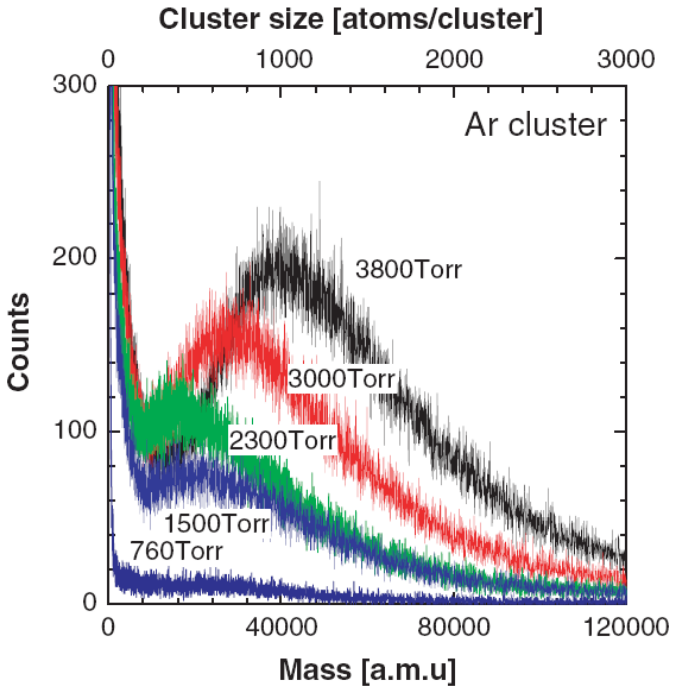

Figure 3.5: Ar cluster ion beam distribution at different stagnation pressures. When the pressure increases cluster size distribution peak shifts toward higher cluster masses. 3000 atoms per cluster ion beam can be realized with a pressure range of 10000 – 10500 Torr [1 Torr = 133.3 N/m^2].

Chapter 4

Material and Surface Characterization Techniques

Investigation of the cluster ion-induced modifications of surface, and crystal structure, as well as chemical composition of materials, requires various techniques that provide detail characterization on materials. This chapter will cover the techniques that were used in the research, and results will be given in following chapters.

4.1 Rutherford Backscattering Spectrometry

Ion beam analysis techniques introduce a non-destructive method for understanding properties of materials. Since the discovery of backscattering of alpha particles from a gold thin film target in 1909 by Sir Ernest Rutherford and colleagues From the results

obtained from Geiger-Marsden experiment Rutherford Model of the atom was formulated in 1911. Rutherford Backscattering (RBS) has been employed to extract information about target material composition and if the material is a thin film, details regarding film thickness and layered compositional variations can be determined. Furthermore, if the ion beam is aligned with sample crystal axes, RBS ion channeling can verify the crystallinity of the sample.

4.1.1 Thin Film Analysis

If a multilayered elemental thin film sample is exposed to alpha particles, the backscattering particle energy varies depending on the number of films, the elements present and the thickness of films. The spectrum that is generated provides information on the sample in terms of backscattering energies, which can be converted into film thickness. Au coated Si substrates that were used in this research study were subjected to Ar cluster ion beam sputtering, and samples had thickness greater than 10 nm. The energy of the beam that was used for the RBS analysis was 2.0 MeV ^{4}He ions. Figure (4.1) shows the energy converted RBS spectrum for a non-bombarded Au thin film coated on Si substrate; a layer of Ti was used to improve adhesion of Au onto Si substrate. The energy difference created by the surface and the interface between film and the substrate ΔE is related to the film thickness by

$$\Delta E = [\varepsilon]_f N \Delta t_f \tag{4.1}$$

where $[\varepsilon]_f$ is the stopping cross section factor and N, Δt_f are the atomic density and the

thickness of the film per channel respectively. $[\varepsilon]_f$ is calculated according to the following equation,

$$[\varepsilon]_f = K_f \frac{\varepsilon_{in}}{\cos(\theta_1)} + \frac{\varepsilon_{out}}{\cos(\theta_2)} \tag{4.2}$$

where K_f is the kinematic factor of elemental thin film, ε_{in} and ε_{out} are inward and outward stopping cross section factors respectively [58]. The scattering angle for the RBS experiment used with respect to the laboratory frame was 165^o and also the incident beam was normal to the target surface, thus the incident angle of the alpha beam was $\theta_1 = 0^o$ and the direction of the scattered particle was at $\theta_2 = 15^o$. According to the mean energy approximation, ε_{in} is evaluated with respect to the incident beam energy (E_o) and ε_{out} with respect to $K_f E_o$. These values were calculated using SRIM 2012 software [59]. From equations (4.1) and (4.2), Δt_f was evaluated for Au thin film. Also the total amount of target atoms sputtered from the surface due to cluster ion beam was estimated with comparison to a non-bombarded Au thin film. Calculated values of amount of Au atoms sputtered are discussed in Chapter 6.

4.1.2 Ion Beam Channeling

Ion channeling describes an energetic ion beam incident onto a crystalline material, and the ion beam is aligned with the crystal orientation. Energetic ions travel further into the material than at a random crystal orientation. Thus, backscattering yield decreases dramatically compared to a random RBS spectra. A particle channels through a crystal

structure if (1) there are openings between atomic rows, (2) there is a force acting on the particle to steer in the ion channel, and (3) the trajectory of the particle is stable by avoiding collisions with atomic rows [60]. The near-surface damage and recovery of a crystalline material due to cluster ion beam can be evaluated using ion channeling technique. In Chapter 5 I will discuss off-normal cluster ion-induced damage and recovery of the crystal structure by thermal annealing using RBS ion channeling for Si (111).

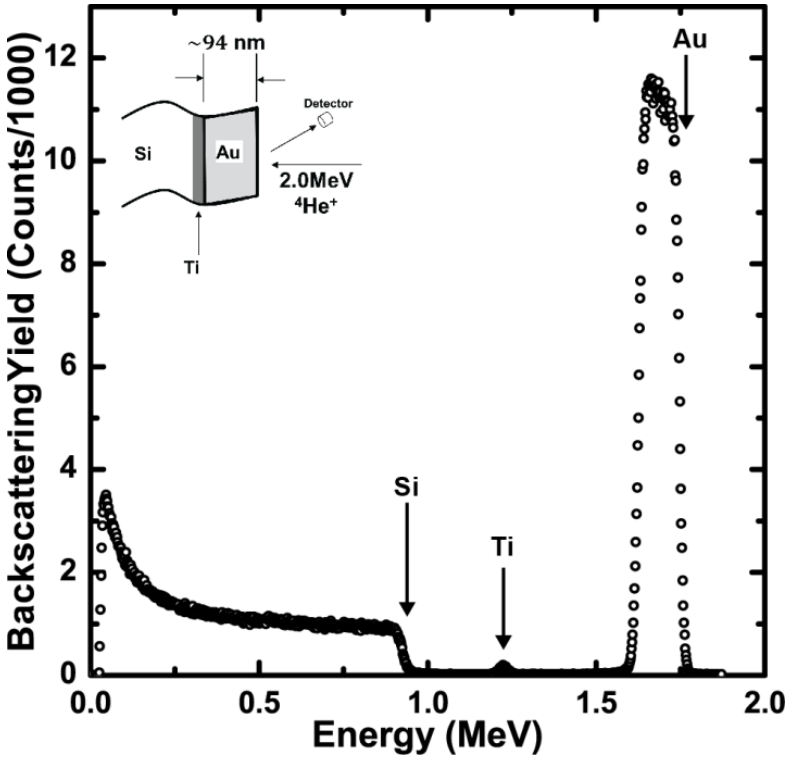

Figure 4.1: Energy converted RBS spectrum for Au thin film coated on Si substrate, Au adhesion on Si is improved by a layer of Ti. The calculated thickness of the non-bombarded Au film was 94 nm; the bulk atomic density of Au 5.9050×10^{22} atoms/cm^3 was considered.

4.2 Atomic Force Microscopy (AFM)

The surface topographies of non-bombarded and bombarded samples were investigated using Park Scientific Auto Probe CP AFM. This provides a 3D profile of the surface on a nanoscale by measuring forces between a sharp probe and the surface at a very short distance. For a contact mode AFM, if the spring constant of the cantilever is less than the surface the cantilever bends. The tip carries a repulsive force and by maintaining a constant cantilever deflection, the force between the probe and the sample can be held constant, and a surface image can be obtained. The AFM images were analyzed by Gwyddion 2.24 AFM imaging software [61]. Surfaces of different bombardment conditions were evaluated by root mean square roughness (r),

$$r = \left\{ \frac{1}{N} \sum_{i=1}^{N} [h_i - \langle h \rangle]^2 \right\}^{1/2} \tag{4.3}$$

The wavelength of surface ripple patterns in x-direction was calculated as the maximum value of the power spectrum of the image. Fast Fourier Transform (FFT) decomposes AFM data signal into harmonic components and thus useful for studying spectral frequencies present in AFM data. Fourier transform of the AFM images was performed using Hann's function as the discrete window function,

$$w(x) = 0.5\,[1 - cos(2\pi x)] \tag{4.4}$$

The 2D FFT image of the AFM scanned image shows the dominating spatial frequencies present on the surface. RMS roughness provides surface behavior at an individual point,

height correlation of two arbitrary points is quantified by the autocorrelation function $A(d)$ or the height-height correlation function $G(d)$ of the surface.

$$A(m,n) = \frac{1}{(N-n)(M-m)} \sum_{l=1}^{N-n} \sum_{k=1}^{M-m} [h_{k+m,l+n}\, h_{k,l}] \tag{4.5}$$

where $m = x_1 - x_2/\Delta x$ and $n = y_1 - y_2/\Delta y$, with $(x_1, y_1), (x_2, y_2)$ coordinates for h_1 and h_2 arbitrary height values, and Δx and Δy are measurement intervals. For AFM measurements, evaluation of surfaces is done only along the fast scanning axis. Therefore, equation (4.5) can be rewritten as,

$$A_x(m) = \frac{1}{N(M-m)} \sum_{l=1}^{N} \sum_{k=1}^{M-m} \left[h_{k+m,l}\, h_{k,l}\right] \tag{4.6}$$

The one-dimensional autocorrelation function in Gaussian form is given by,

$$A_x(x_1 - x_2) = \sigma^2 \exp\left[\frac{-(x_1 - x_2)^2}{T^2}\right] \tag{4.7}$$

here σ and T are the root mean square deviation of the heights and the autocorrelation length, respectively. The difference between the autocorrelation function and height-height correlation function is negligible. For the latter function the power of difference between arbitrary points are considered. One-dimensional height-height correlation function can be written as,

$$G_x(x_1 - x_2) = \frac{1}{N(M-m)} \sum_{l=1}^{N} \sum_{k=1}^{M-m} [h_{k+m,l} - h_{k,l}]^2 \tag{4.8}$$

The Gaussian form of the height-height correlation function is given by,

$$G_x(x_1 - x_2) = 2\sigma^2 \left[1 - \exp\left\{-\frac{(x_1 - x_2)^2}{T^2}\right\}\right] \quad (4.9)$$

AFM evaluations of surfaces are presented in Chapters 5 and 6.

4.3 Profilometer Analysis (PA)

The Tencor Alpha step 200 profilometer was used to determine the amount of material removed from the surface of bulk and polymeric materials. Half of each sample was covered before bombardment of cluster ions to create a step on the surface. The height difference that occurs on the surface due to bombardment is called an alpha-step. Then samples were mounted on a manually operated x-y stage of the profiler, and they were scanned across in one direction to measure the difference in step height. The step height represents the amount of material sputtered from the surface for a given dosage. Alpha steps were created for Si samples, which is discussed in detail in Chapter 5.

4.4 Scanning Electron Spectroscopy (SEM)

FEI XL-30FEG SEM provides the flexibility of scanning through a sample surface. It uses a focused electron beam with 15 keV energy to excite electrons in the material, which generate an image depending on the amount of these secondary electrons

collected. Intensity of each pixel is determined by collected electrons. SEM was used because of its flexibility of scanning through a sample surface to identify cluster ion beam shadowed regions, which assist in determining the formation of ripple patterns. Analysis of SEM images will be described in Chapter 5 and Chapter 6.

4.5 X-ray Photoelectron Spectroscopy (XPS)

Cluster ion beam bombardment induced surface chemical modification was studied using XPS. XPS spectra are acquired by bombarding the material surface with a beam of x-rays and simultaneously measuring the kinetic energy and the number of electrons escaping from the surface. The instrument that was used in this experiment was a Physical Electronics PHI S-700 ESCA system with Al filament x-ray source. The energy of the incident photon and kinetic energy of electrons is related by,

$$hv = E_{elec} + E_{bind} + \emptyset_{wf} \tag{4.5}$$

where hv is the x-ray photon energy, $\emptyset_{wf}$ is the work function induced by the analyzer, which is about 4-5 eV, and E_{bind} is the binding energy. The work function is artificially given by the instrument. Therefore, the binding energy can be estimated by the energy difference between the incident x-ray photon energy and the kinetic energy of escaping electrons from the surface. XPS spectra are plots of measured numbers of electron versus binding energy. Each element on the surface represents a characteristic binding energy. An XPS spectrum produces binding energy signals for almost all elements in the periodic

table except hydrogen. Au thin film substrates were analyzed and discussed in Chapter 6.

4.6 Static Contact Angle Goniometer Measurements

Interaction between liquid molecules and solid molecules is conveniently described by contact angle measurement. Contact angle is the angle between the solid-liquid interface and the liquid-vapor interface of a liquid droplet on a surface. The shape of the liquid droplet is explained by the Young-Laplace equation. The thermodynamic equilibrium between solid, liquid and vapor phase is important in understanding liquid-solid interactions. At equilibrium, chemical potentials in each of the three phases are equal. Also at equilibrium the interfacial energy between solid-vapor is equal to the interfacial energies between solid-liquid and liquid-vapor along the solid surface. This is known as the Young Equation [62] and describes equilibrium the contact angle of liquid on a flat surface.

Figure 4.2 shows the static sessile drop method used to determine the contact angle of a water droplet (volume 1 μL). A water droplet is brought close [Figure 4.2 (a)] to the surface until it touches the solid surface, then the droplet transfers onto the surface. A high intensity lamp is illuminated on one side and the profile of the water droplet is recorded from other side. The image recorded corresponds to the static contact angle taken when the droplet settled immediately after the transfer. Figure 4.2 (b) shows a water droplet on a surface bombarded with large gas clusters at an off-normal angle. $\theta_A > 90^o$, indicating that the surface had become hydrophobic and liquid-solid interactions are

limited due to low surface energy. Figure 4.2 (c) shows a surface bombarded with gas cluster ions at surface normal direction and $\theta_B < 90^o$ indicates that the surface is hydrophilic.

For a rough surface the contact angle is different compared to flat surface as described by Young equation. This contact angle hysteresis was first demonstrated by the Wenzel model [63] for a completely wetting homogeneous surface. The Wenzel model is valid when the liquid droplet is comparably larger than the surface rough features. However, when the size of the liquid droplet is comparable with the surface structures (heterogeneous surfaces), vapor trapped between structures must be considered. Thus Cassie-Baxter equation introduces a factor that compensates for vapor trapped between surface structures [64].

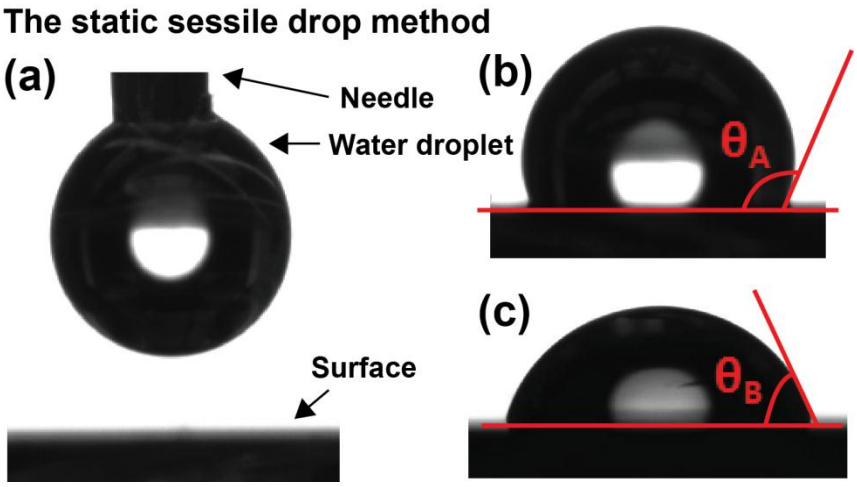

Figure 4.2: The contact angle between a solid-liquid interface and a liquid-vapor interface is determined by using the static sessile drop method. (a) The water droplet with 1μL volume just before the transfer onto the surface. (b) A water droplet on a surface bombarded with large gas cluster ions at an off-normal angle. $\theta_A > 90^o$ means that the surface had become hydrophobic and liquid-solid interactions are limited due to low surface energy. (c) A surface bombarded with gas cluster ion beam at surface normal direction and $\theta_B < 90^o$ indicates that surface is hydrophilic and the surface energy is higher.

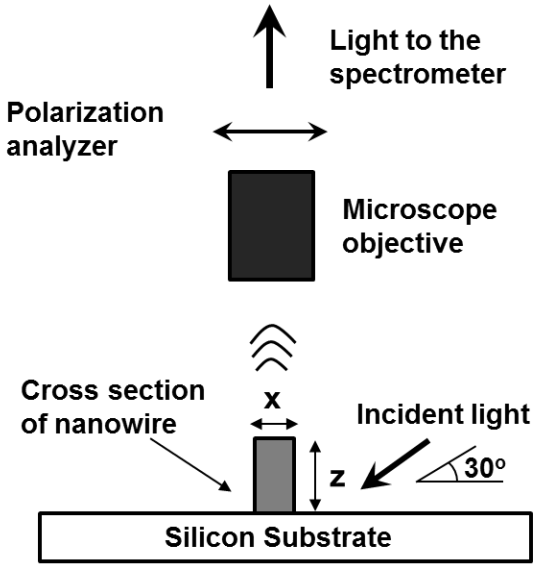

Figure 4.3: Experimental setup used for optical scattering measurements of gold nano-ripples.

4.7 Surface Plasmon Resonance Measurements

Rippled Au and Ag surfaces were studied for surface plasmon effects. Metallic nano structures interact strongly with visible light due to conduction electron oscillations [65, 66]. This creates strong localized electromagnetic fields that produce intense incident light scattering around a resonance wavelength. The plasmon resonance wavelength depends on the size, shape and material. The variation of resonance wavelength with metallic ripple structures is discussed in Chapter 7. The investigation of the surface was carried out by using a standard light microscope fitted with dark-field illumination [67].

The scattering spectrum of rippled surface was obtained by illuminating unpolarized focused white light perpendicular to the ripples with 60^{o} incident angle from the surface normal as shown in Figure 4.3. The raw spectrum of the rippled surface is compared with a reference white light spectrum to produce a normalized surface plasmon resonance spectrum. The dark-field illumination maximizes scattering from ripple structures and reduces the substrate effect. A spectrum was obtained when light illuminated parallel to the ripple structures. Figure 4.4 shows the process of extracting the surface plasmon spectrum.

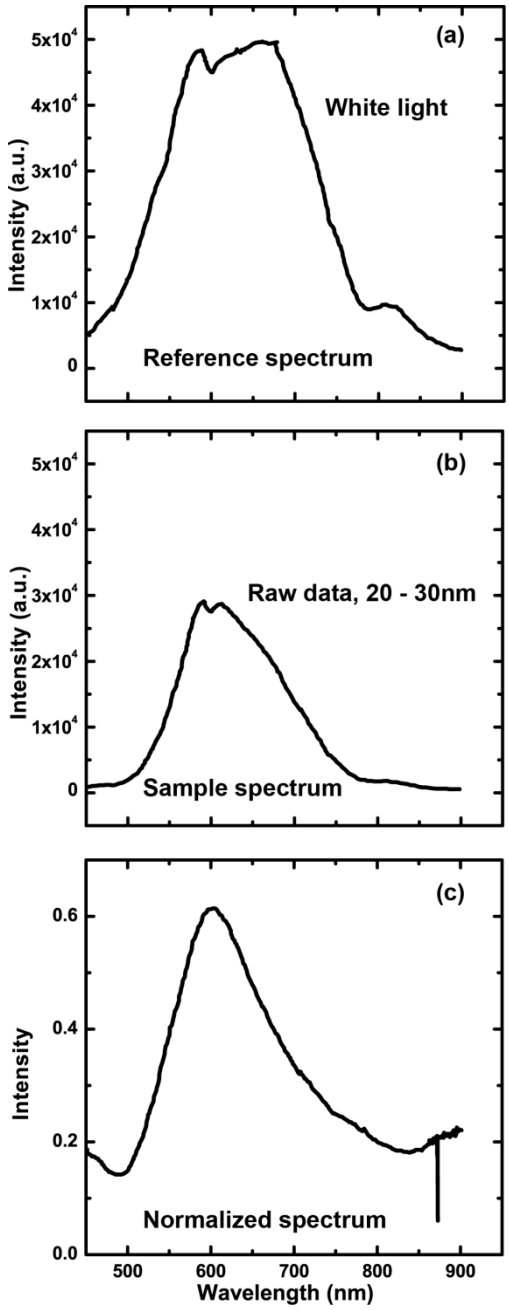

Figure 4.4: (a) Scattering spectrum from white source, (b) Raw data obtained from a nano structure, (c) The raw spectrum of surface nano structure is compared with the reference white light spectrum to produce a normalized surface plasmon resonance spectrum.

Chapter 5

Self-assembled Nano-patterns on Si Surfaces by Ar Cluster Ion Beam Bombardment

Nano-pattern formation on Si surfaces by Ar_{3000} cluster ion bombardment is investigated as a function of cluster ion angle of incidence and applied dosage. This chapter covers a comparison of cluster ion beam and monomer ion-induced nano-patterns on Si substrates.

5.1 Introduction

Self-assembled pattern formation due to ion beam bombardment has created significant interest in recent years owing to their ease in processing with known conditions, and

fewer processing stages compared to a template based or lithography techniques. Si substrates are the most extensively researched material in nano-pattern formation because of their notable monatomic crystallography [68-75]. Although the process is well known, the ripple formation phenomenon to date is investigated to establish a universal theory in micro-nano scale surface evolution models [30,31,36,76-79]. So far nano-pattern formation models and experiments based on monomer ion bombardment have suggested ion beam dependence on the angle of incidence, dose, energy, type of ion, and current density.

However, cluster ion-induced nano-pattern formation follows a different mechanism. The synergistic interactions between an off-normal cluster ion and a surface generate forward moving atoms due to momentum transfer [17]. These mobile atoms re-deposit close to the collision site. One interpretation of nano structure formation is the shock wave formation due to cluster ion collision [14]. Nevertheless, shock wave formation is a single collision event process and does not explain the spatio-temporal growth of nano structures. Inelastic collisions within the cluster ion [42] when colliding with a surface provide additional energy due to van der Waal bond separations and lead to generation of large amounts of surface mobile atoms. Because of these cascading events within the cluster ion, surface penetration minimizes [17]. Surface curvature is not required for a cluster ion beam to initiate a surface morphological variation [80], although the cluster ion-induced surface roughness dependence increases on existing surface structures with the applied dose. The Bradley and Harper model suggests the curvature and isotropic thermal diffusion dependence for the formation of surface ripple structures on amorphous

materials [28] and these structures vary in orientation from perpendicular to parallel depending on the incident angle of the monomer ion beam. Nonetheless, cluster ion-induced surface ripples are always perpendicular to the incident beam, and ripples disappear at a grazing incident angle for silicon amorphous surfaces.

5.2 Experimental Details

Silicon substrates with orientations of (111), (110), and (100) were cleaned before loading in the main chamber of the Gas Cluster Ion Beam (GCIB) system. A detailed schematic diagram of the GCIB system is given and described in Chapter 3. A high pressure Ar gas undergoes supersonic expansion to produce neutral clusters, which are ionized and accelerated to produce a beam of cluster ions with each cluster ion consisting of about 3000 Ar atoms. Samples were bombarded with 30 keV Ar cluster ion beam at different incident angles from 0^o to 80^o in steps of 10^o and at a dose of 1×10^{16} cluster/cm^2; the incident angle was measured from the target surface normal. Also, the bombardment dose was selected up to 1×10^{18} clusters/cm^2 for the incident angle 60^o and the cluster ion beam current density was set to 1 $\mu A/cm^2$ with homogeneous beam scanning. The low beam current avoids target sample heating, and the target chamber was maintained at 24.5 ^oC with chamber pressure lower than 3×10^{-4} N/m^2. Each sample was characterized by Atomic Force Microscopy (AFM). The AFM image area was 5×5 μm^2, which included in all cases sufficient ripples to make substantial measurements. A clear statistical understanding can be achieved by determining the surface root mean square

roughness, dominant wavelength, and correlation length, and by calculating the roughness and the growth exponent.

The surface sputtered depth was estimated by producing an alpha step during cluster ion beam bombardment and step height was measured by profilometer. Nano-ripple Si sample bombarded at 60^{o} at a dose of 1×10^{16} clusters/cm^{2} was annealed at 550 ^{o}C for 1 hour to determine the surface roughness and the degree of crystal structure recovery. Rutherford Backscattering Spectroscopy (RBS) ion channeling measurements were conducted on a non-bombarded sample, on Ar cluster ion beam bombarded sample and on the annealed rippled sample.

5.3 Experimental Results and Discussion

5.3.1 Si Surface Roughening and Linear Regime

In the course of the Ar cluster ion beam bombardment study, we found that Si surface roughness has a maximum transition incident angle as shown in Figure 5.1. We measured surface root mean square roughness as a function of Ar cluster ion beam incident angle measured from the surface normal, for each sample the dose was kept at 1×10^{16} clusters/cm^{2}. Surface instability increases significantly up to 70^{o} incident angle and then drastically decreases to a smooth surface at a grazing incidence angle of 80^{o}. Ripple patterns are formed in the range of 50^{o} to 70^{o}, and below 50^{o} angle surface features are random; these results are in agreement with previous work [17, 81, 57]. Monomer ion

experiments conducted by Ziberi et al. indicate ripple formation on Si surfaces at as low as 5^o incident angle from the surface normal for Ar^+ (1500 eV), Kr^+ (2000 eV) and Xe^+ (2000 eV) with 6.7×10^{18} ions/cm^2 with the beam current density at 300 μA/cm^2 [71]. According to their results, from 35^o to 60^o the surface became smooth and beyond 60^o ion bombardment generated saw tooth-like structures. Nonetheless, these experimental results are argued considerably, other research groups' observations show ripple formation on Si surfaces in the region of 55^o to 70^o from the surface normal with a dose of 1×10^{18} ions/cm^2 at ion beam density of 18 μA/cm^2 [82]. The maximum surface instability for Si occurs at 70^o for a dose of 1×10^{16} clusters/cm^2.

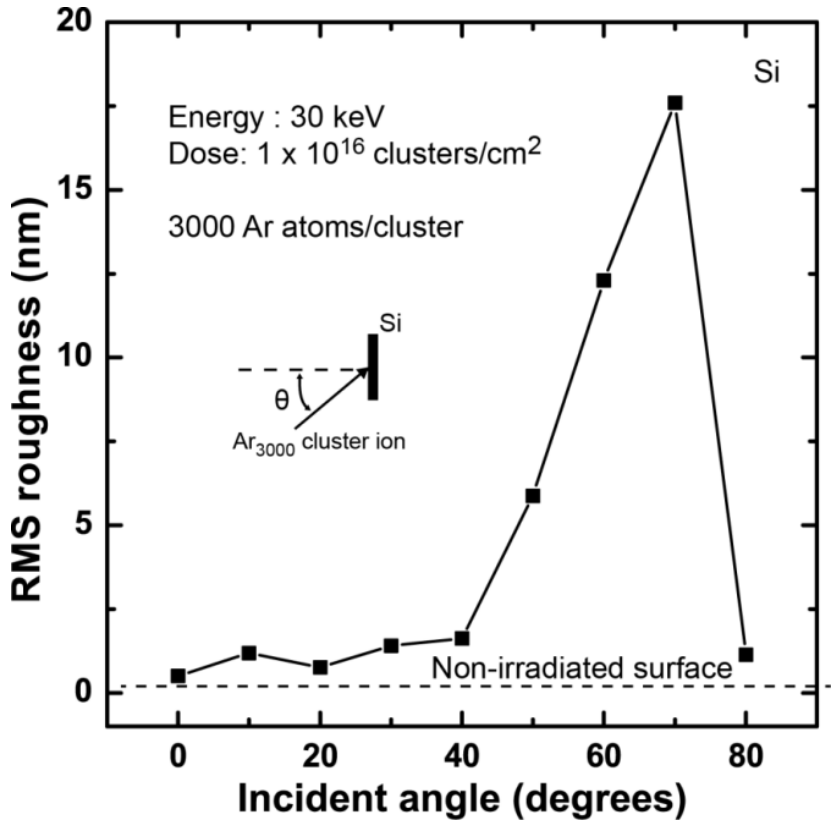

Figure 5.1: RMS roughness of the Si (111) surface with the cluster ion incident angle. After 70^o the surface roughness reduces considerably and at grazing incident angles the surface is smooth.

Surface self-assembly and modes of nano-ripples depend on the cluster ion beam incident angle and dosage. Figures 5.2 (b) – (d) shows the atomic force microscope scans for cluster ion bombarded at 50^o, 60^o and 70^o angles from the surface normal. Island-like structures formed at 70^o is due to the existence of random ripple modes. Evolution of ripples leads to domain walls and domain boundaries (or ripple dislocations) and understanding of these features is important. Figure 5.2 (a) illustrates a smooth surface due to the normal incident Ar cluster ion beam. Normal incident cluster ions sputter surface atoms laterally (parallel to the surface) [18]. These sputtering atoms fill up trenches and smooth the surface. If cluster ions are bombarded continuously the surface begins to sputter exponentially [19].

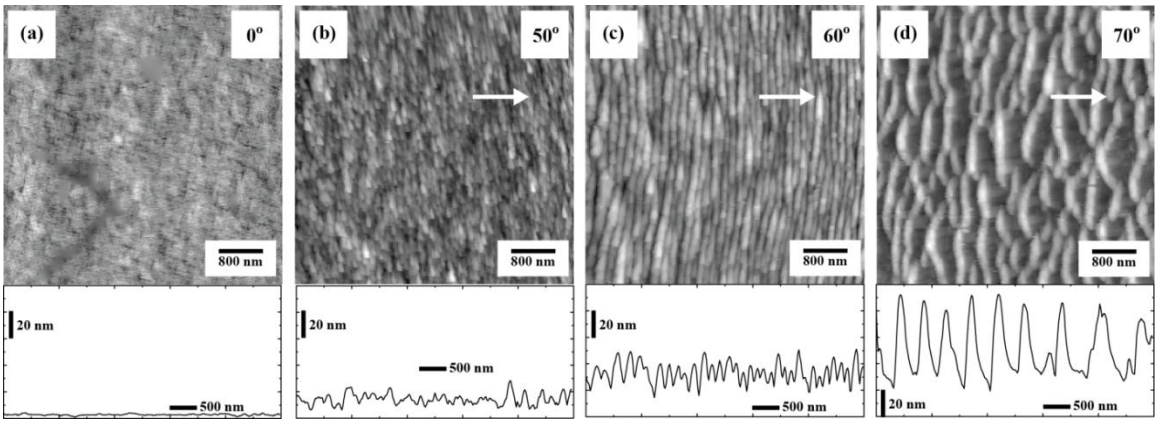

Figure 5.2: Atomic force microscope scans of Si (111) bombarded with 1×10^{16} clusters/cm^2 dose Ar cluster ions at (a) 0^o, (b) 50^o, (c) 60^o and (d) 70^o. The scan area for all images is $5 \times 5\mu m^2$. White arrows indicate the direction of the cluster ion incidence, and for image (a) the cluster ion direction points inward.

During our experiment, we found that nano-ripple formation did not depend on the Si crystal orientation. This is caused by amorphization of the surface layer due to high energy transfer between cluster ions and the surface. As an example, Figures 5.3 (a) and (b) show both RBS channeling spectra for a non-bombarded Si (111) substrate and for a cluster ion beam bombarded Si (111) substrate, respectively. For the bombarded sample, an amorphous surface layer of 58 nm is formed. Therefore, in the following sections we will discuss only cluster ion-induced ripple formation on Si (111) substrates. When the bombarded sample was annealed at 550 ^{o}C for an hour, the substrate crystallinity recovered about 15% as demonstrated in Figure 5.4. During this re-crystallization process the surface root mean square roughness increased from 12.3 nm to 15.4 nm, and also the average wavelength increased from 200 nm to 230 nm. However, ripple dislocations increased with thermal annealing as shown in Figure 5.5.

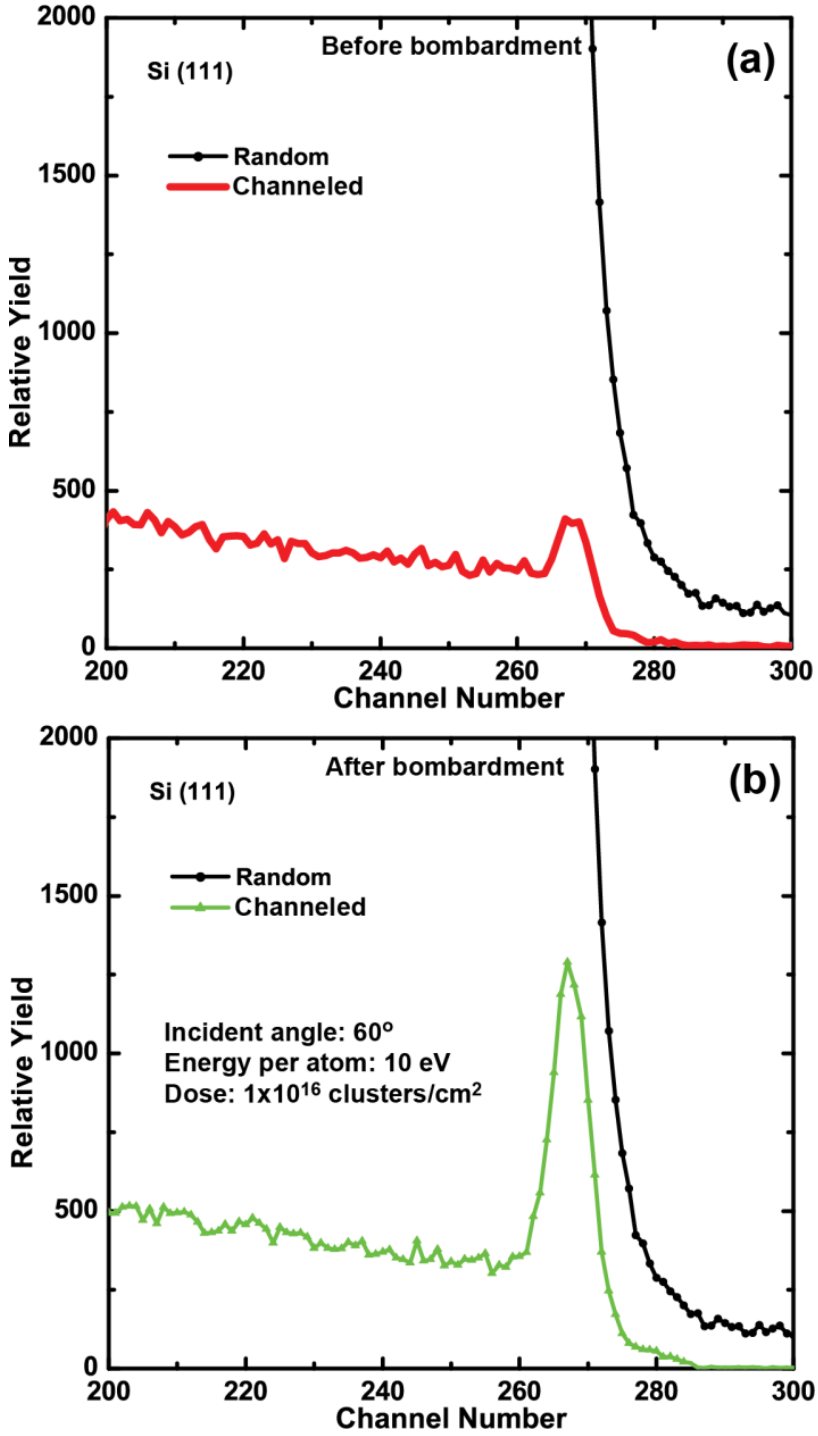

Figure 5.3: RBS random and channeling analysis of the surface damage in Si (111) substrates induced by Ar cluster ion beam bombardment, (a) before and (b) after bombardment (1×10^{16} clusters/cm^2, 60^o). After bombardment an amorphous layer of 58 nm is formed on the substrate.

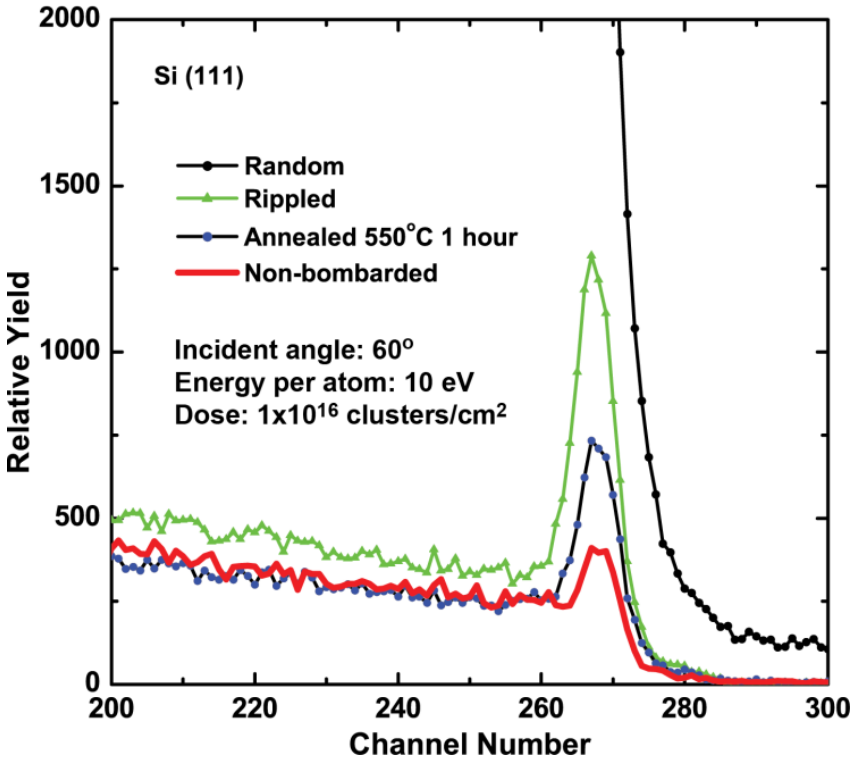

Figure 5.4: RBS channeling analysis of the surface damage recovery (15% recovered from the original substrate) due to thermal annealing at 550 ^{o}C for an hour.

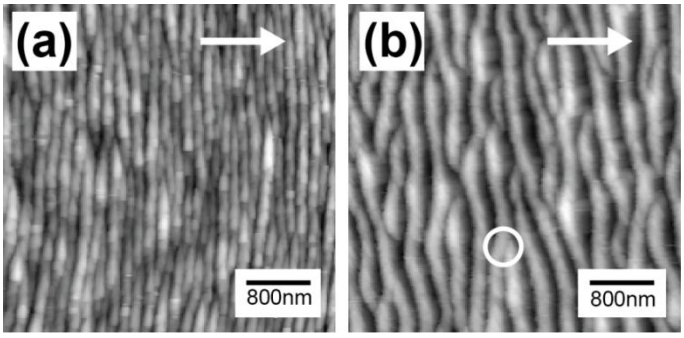

Figure 5.5: Atomic force microscope scans of Si (111) substrates (a) Ar cluster ion beam bombarded at a dose of 1×10^{16} clusters/cm^2 and at an angle of incidence of 60^{o}, (b) Thermal annealed Si substrate. The scan area for all images was $5 \times 5\mu m^2$. White arrows indicate the direction of the cluster ion incidence and the white circle shows ripple dislocations.

In our experiments, the target temperature did not deviate from the room temperature. However, experiments have shown that the temperature of the target can rise up to about 150 ^{o}C during monomer ion beam bombardment [83]. Significance between our Ar cluster ion experiments and monomer ion beam experiments are the energy per atom, the beam current density, and the target temperature due to beam heating. Beam heating activates isotropic thermal diffusion of surface atoms for monomer ion processing [28]. Since cluster ion beam processing of surfaces is at room temperature, main diffusion activation is effective ion surface diffusion.

The randomness of initial impact of cluster ions creates surface defects that produce arbitrary ripple modes at the surface, which depends on the basic parameters of a cluster ion (angle of incidence, energy and dose). Continuous bombardment of clusters, coalesce into ripples and this process is a time dependent. Figure 5.6 (a) – (c) shows atomic force microscope scans for off-normal incident angles 50^{o}, 60^{o}, and 70^{o} at 2.5×10^{15} clusters/cm^{2}, 7.5×10^{15} clusters/cm^{2} and 1×10^{16} clusters/cm^{2} dosages. However, according to figures, angle of incidence also plays an important role in the self-assembly of nano-ripples. For example, at 70^{o} surface nano-ripples have a large amount of dislocations, even though the roughness is higher as shown in Figure 5.7.

Qualitatively, our results point out that both amplitude and wavelength of surface nano-structures at all incident angles show initial linear growth in their physical parameters, which eventually saturates at higher dosages. Figure 5.7 shows the root mean square roughness variation of ripples formed on Si (111) for cluster ion beam incident angles 50^{o}, 60^{o}, and 70^{o} as a function of dose. Immediate saturation of surface roughness and

wavelength (as shown in Figure 5.8) is observed for 50^{o} cluster ion incidence caused by high surface sputtering. Furthermore, cluster ion-induced nano-ripple linearity resembles monomer ion beam ripple formation where growth parameters increase linearly and eventually begin to saturate at a critical angle [83].

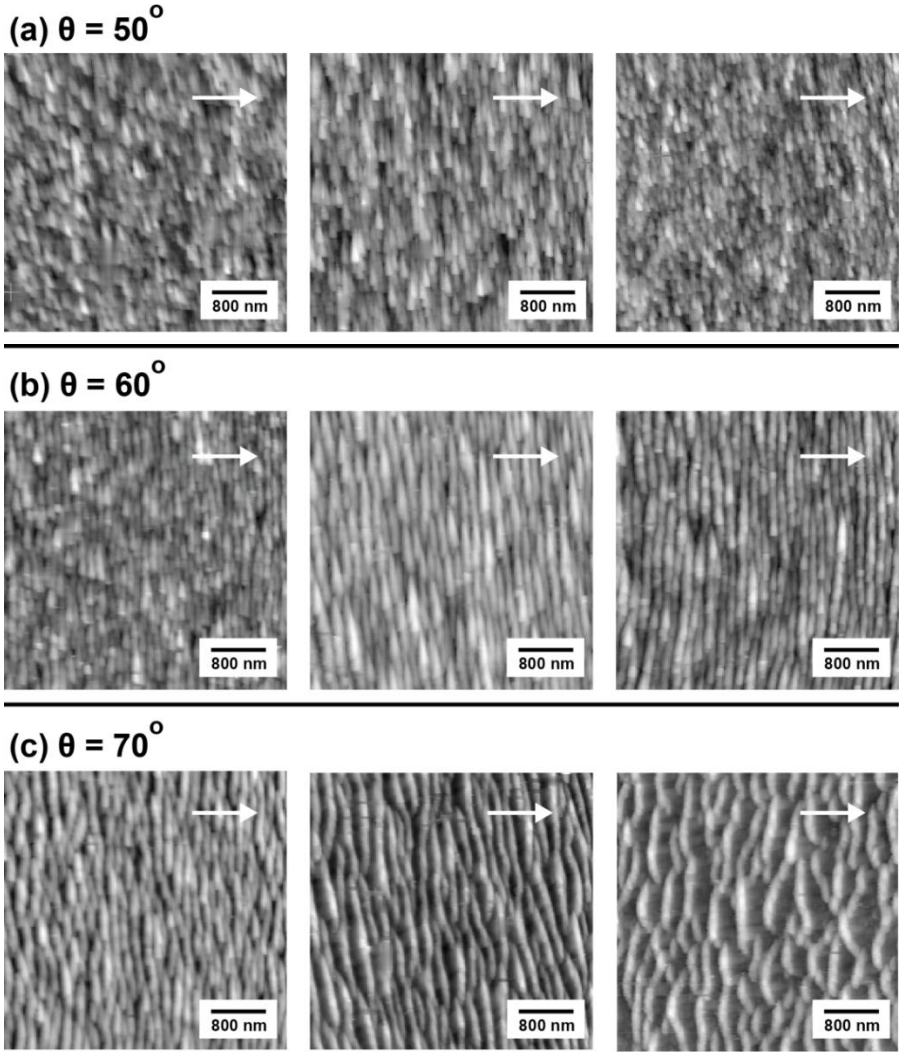

Figure 5.6: Atomic force microscope scans of nano-ripple structures on Si (111) for angles of incidence of 50°, 60°, and 70°. The dose evolution is shown for each angle are from 2.5×10^{15} clusters/cm^2, 7.5×10^{15} clusters/cm^2 and 1×10^{16} clusters/cm^2. The scan area for all images is $5 \times 5\mu m^2$. The arrow indicates the direction of the cluster ion incidence.

The Bradley and Harper model [28] predicts the linear growth of ripples, but does not to predict ripple saturation (Appendix A). The Makeev, Cuerno and Barabási (MCB) model modified the Bradley and Harper model by including non-linear terms that depend on the slope of the surface and the random ion flux (Appendix A). Moreover, this model considers effective ion-induced diffusion rather than isotropic thermal diffusion. Most theoretical calculations show coupling of monomer ions and mobile surface atoms.

The root mean square surface roughness and wavelength can be written as a function of time (or dose) showing a power law behavior, $r \propto t^{\beta}$ and $\lambda \propto t^{\gamma}$, respectively. These conditions arise when the ripple growth is independent of the size of the target sample. According to the scaling theory [84], β is called the growth exponent and the reciprocal of γ is the dynamic exponent. This linear scaling is observed in monomer ion as well as in cluster ion bombarded surfaces. Theoretical and experimental results obtained by the Kardar-Parisi-Zhang non-linear stochastic partial differential equation for monomer ion bombarded Si (111) has found a value for β as 0.25 [30]. For example β is 0.38 for O_2^+ bombarded Si (100) surface at an incident angle of 60^o [85] and β is 0.33 for Ne^+ bombarded onto Ag (100) at 70^o [86].

Our results on β and γ for Ar cluster ion beam bombarded Si (111) surface are given in Table 5.1. Thus results show for cluster ion beam incident angle 70^o the surface has higher instability compared to 50^o and 60^o. This may be due to the surface sputtering at 70^o is lower than 50^o as shown in Figure 5.9. Linear curve fitting shows that for 50^o angle of incidence amount of Si atoms sputtered from the surface as 116 ± 14 atoms per cluster

ion. This amount of Si atoms sputtered drops to 55 ± 4 and 46 ± 3 atoms per cluster ion for 60^{o} and 70^{o} angles, respectively.

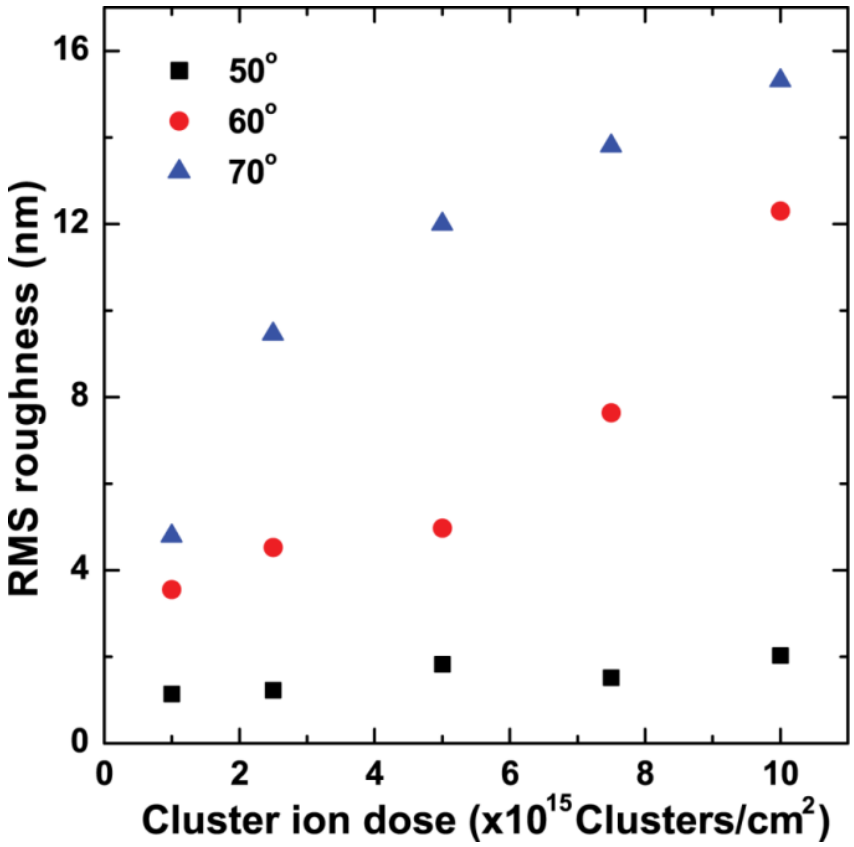

Figure 5.7: Root mean square roughness as a function of the dose for Si (111) substrates when the cluster ion bombarded at incident angles 50°, 60°, and 70°.

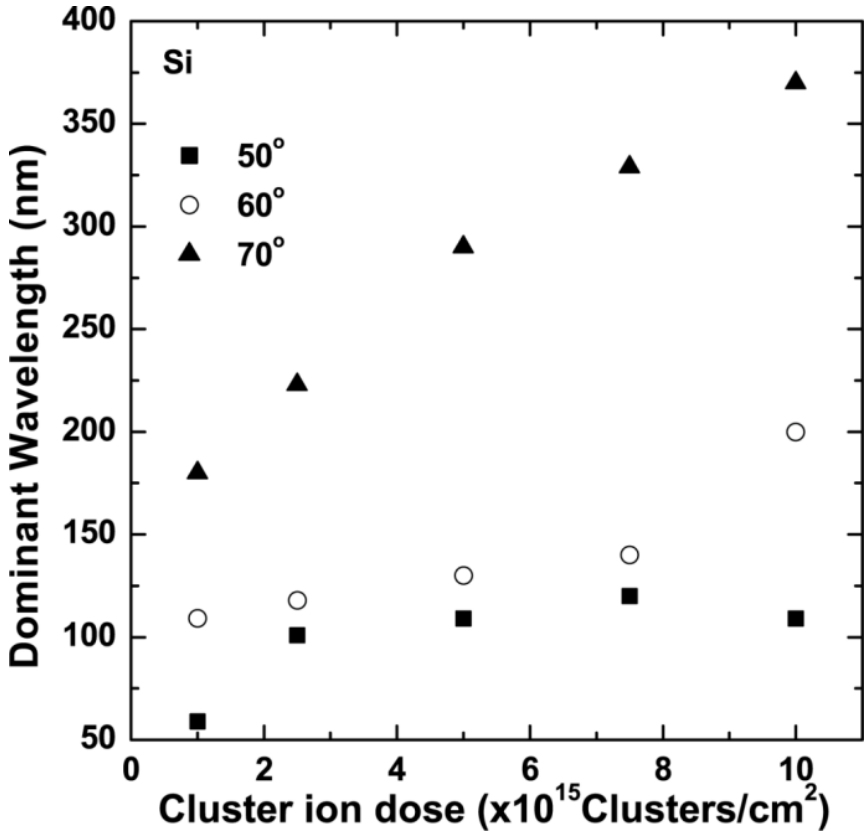

Figure 5.8: Characteristic ripple wavelength as a function of dose for Si (111) substrates when the cluster bombarded at incident angles 50°, 60°, and 70°.

Table 5.1: The growth exponent (β) and the reciprocal of dynamic exponent (γ) for Si (111).

Incident angle [°]	β	γ
50	0.19 ± 0.12	0.22 ± 0.08
60	0.41 ± 0.09	0.25 ± 0.10
70	0.50 ± 0.06	0.33 ± 0.02

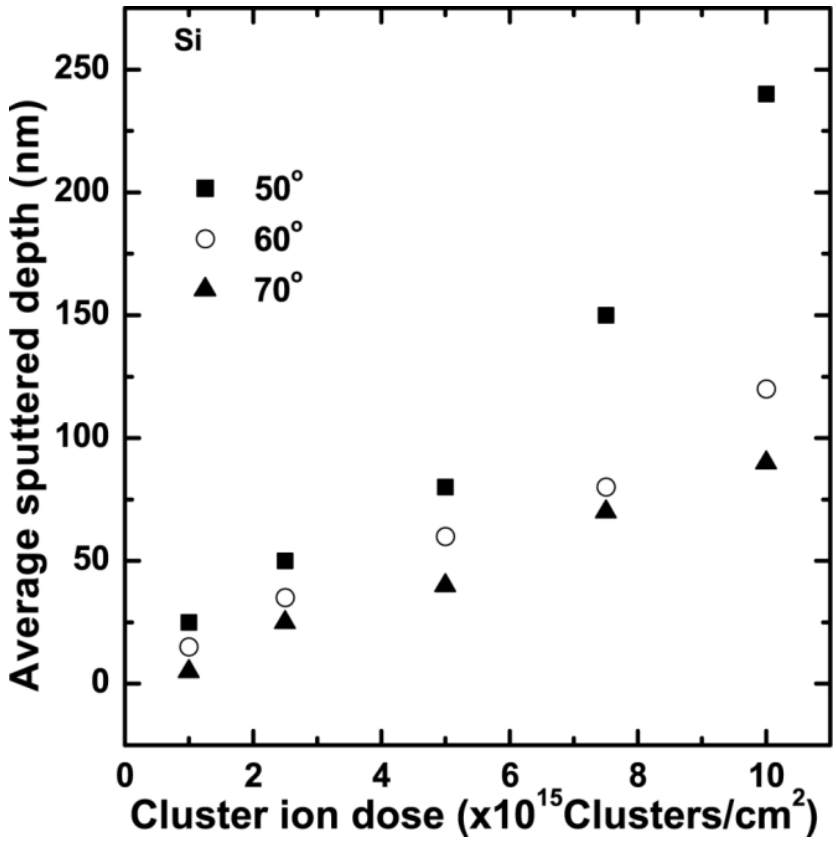

Figure 5.9: Average sputtering depth of Si (111) as a function of dose for 50°, 60°, and 70° incident angles.

The spatial behavior of a surface can be characterized by autocorrelation length in addition to amplitude parameters, such as root mean square roughness or average roughness. Autocorrelation length can describe random surface decays as well as how two points in space can be treated in a random process. Figure 5.10 shows the autocorrelation length as a function of the applied dose for a Si surface. The autocorrelation length depends on the roughness exponent (α), the system correlation length (τ) and the wavelength of the substrate. The system correlation length (τ) is extracted from the autocorrelation function in the direction of ripple wavelength. It is

defined as $A\ (\tau) = \ 1/e$, this represent the characteristic length between fluctuations or how much two scans are similar to each other. In a sense a larger wavelength and $\alpha \ \rightarrow 0$ will result in a longer autocorrelation length and for smooth surface ($\alpha \ \rightarrow 1$) will result in shorter correlation. In regard to 50^{o} results, autocorrelation length decreases with applied dose due to restriction of self-assembly. In contrast for both 60^{o} and 70^{o} angle autocorrelation length increases with applied dose.

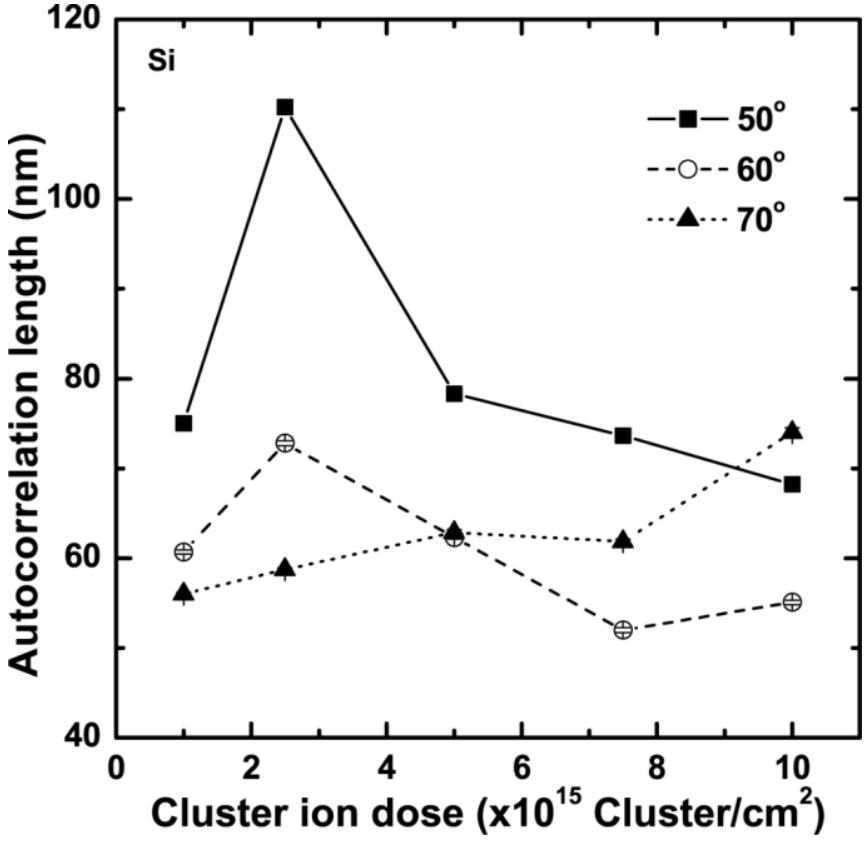

Figure 5.10: Correlation length as a function of the dose for Si (111) substrates, when the cluster bombarded at 50°, 60°, and 70° incident angles.

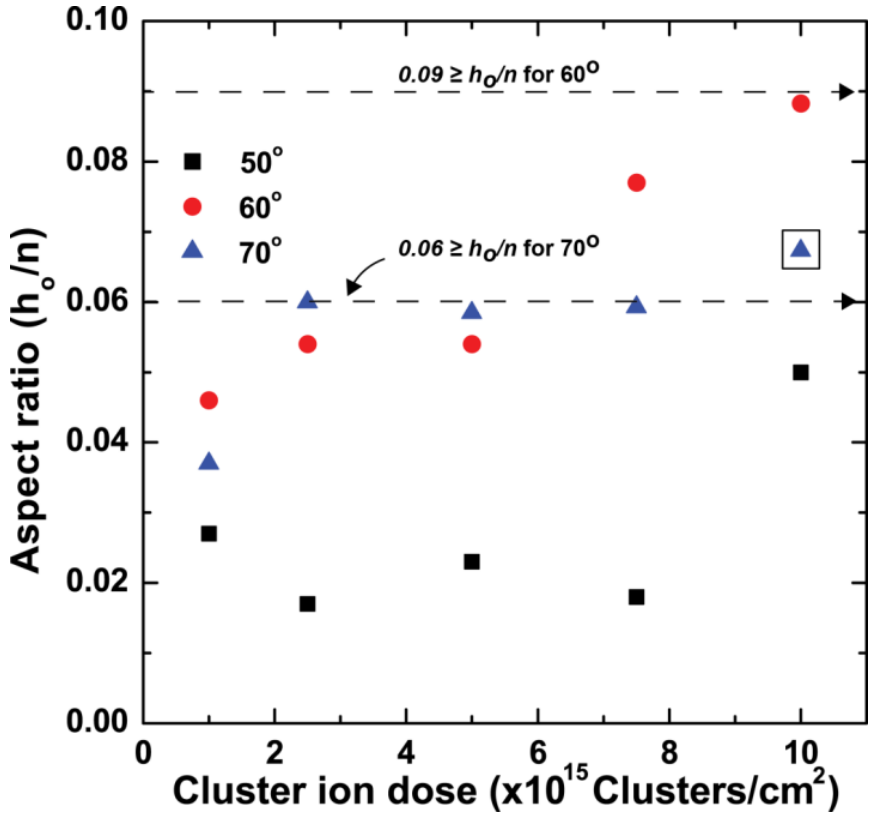

Figure 5.11: Aspect ratio of surface structures on Si (111) as a function of dose for 50°, 60°, and 70° incident angles. Assuming a sinusoidal surface [36], Table 5.2 lists the limiting conditions to avoid saturation. The squared data point indicates aspect ratio increase due to atomic accumulation.

5.3.2 Saturation of Ripples and Sand Dune-like Structures on Si Surfaces

The ripple growth on a surface saturates with time because of limiting ion beam conditions and geometrical surface features. This has been observed for monomer and as well as for cluster ion beams. Carter [36] (Appendix A) has shown that saturation is caused by geometrical shadowing of surface structures; his explanation considers a sinusoidal ripple pattern. When the amplitude to the wavelength aspect ratio increase with time, the slope of the sinusoidal ripple becomes outsized, triggering the ion beam to be shadowed upstream of the ripple and slowing down the following ripple growth. As an example for a sinusoidal ripple pattern with amplitude of $h = h_o \sin(2\pi x/n)$, where h_o is the amplitude of ripples and n is the wavelength, Carter [36] proposed a limiting condition of h_o/n to avoid shadowing. Thus, for an incident angle of θ, ion beam parameters should satisfy $\tan(\pi/2 - \theta) \geq 2\pi h_o/n$.

Figure 5.11 shows the aspect ratio of surface structures as a function of dose for Ar cluster ion beam bombarded Si (111) substrates. It clearly shows that for 70^o, the shadowing process starts at 2.5×10^{15} clusters/cm^2, and for 60^o cluster ion beam shadowing begins after 1×10^{16} clusters/cm^2 (also listed in Table 5.2). The shadowing effect causes cluster ions to interact with upstream of an existing ripple rather than the low surface curvature (trenches). Beyond this critical dose (or time) ripples follow a non-linear dynamic process. For 50^o, clear variation on the surface is not observed due to high sputtering, which lead to kinetic roughening growth.

Table 5.2: The aspect ratio limiting condition and the dose at which ripple saturation begins for Ar cluster ion-induced nano-ripples on Si (111) substrates.

Incident angle [°]	h_o/n (limiting condition)	Dose ($\times 10^{15}$ clusters/cm^2)
50	0.13	-
60	0.09	10.0
70	0.06	2.5

In the non-linear regime, ripples growth is influenced by the existing surface structures. Figure 5.12 (a) and (b) show atomic force microscope scans for Si (111) bombarded at 60^o and 70^o incident angles with 1×10^{17} clusters/cm^2 dose, respectively. To characterize these ripples we assess the height-height correlation function (Chapter 4) of the atomic force microscope data [83]. The dynamic scaling hypothesis [84], indicates that for d smaller than the length scale of average separation of periodic pattern $G(d) \propto d^{2\alpha}$, d is the length scale perpendicular to the ripple pattern. Figure 5.13 shows the $G^{1/2}(d)$ variation as a function of d. The first minimum of curves as shown in figure gives a rough measurement of wavelength (λ) of the ripple patterns and the first maximum is a measurement of surface average roughness $r = G^{1/2}(\lambda/2)$. The ripple wavelength increases from 200 nm, 459 nm to 2412 nm for applied doses of 1×10^{16} clusters/cm^2, 1×10^{17} clusters/cm^2 and 1×10^{18} clusters/cm^2, respectively.

Furthermore, continuous cluster ion bombardment produces ripples comparable to the image length scale and coalescence of ripples disrupts to create isolated large scale sand dune like structures as shown in Figure 5.12 (c). Within these structures secondary patterns develop on the upstream due to local surface gradient and sputtering. Larger

cluster ion incident angles from the surface normal produces longer ripple wavelengths; 459 nm for 60^o and 1065 nm for 70^o at 1×10^{17} cluster/cm^2 dosage. This variation is similar to low dose observations. However, the surface roughness for 70^o (23.22 nm) is lower than 60^o (25.85 nm) as shown in Figure 5.14. This is due to surface roughness at 70^o decreases forming faceted saw tooth, which is prominently observed at grazing incident angles. Whereas for 60^o angle of incidence, ripples grow over time to form nano-dune structures.

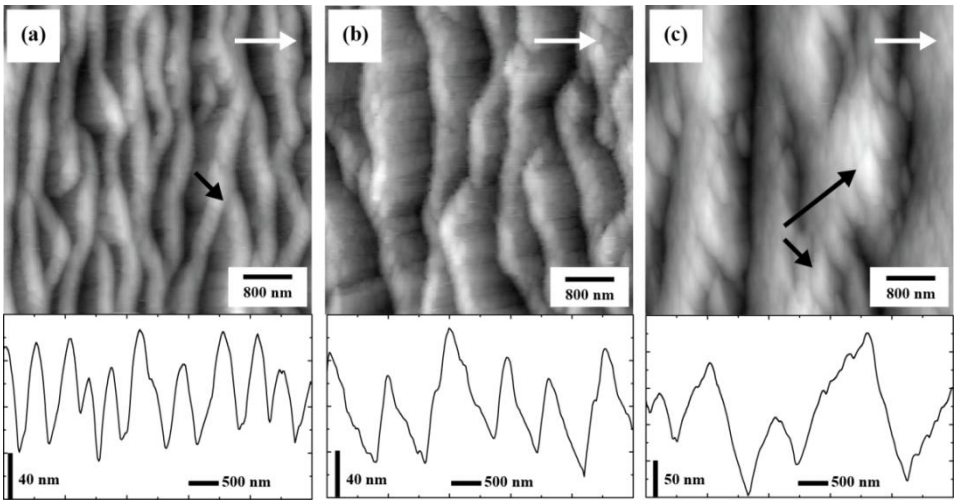

Figure 5.12: Atomic force microscope scans of nano-ripple structures on Si (111) for angles of incidence of (a) 60° and (b) 70° cluster ion bombarded at 1×10^{17} clusters/cm^2 dose. In (a) the black arrow indicates wall boundaries (or ripple dislocations). (c) The sand dune like structures formed on Si (111) after cluster ion bombardment at 1×10^{18} clusters/cm^2 dose and at an incident angle of 60^o, the black arrows show secondary structure formations on primary surface pattern. The scan area for all images is 5×5 μm^2. The arrow indicates the direction of the cluster ion incidence.

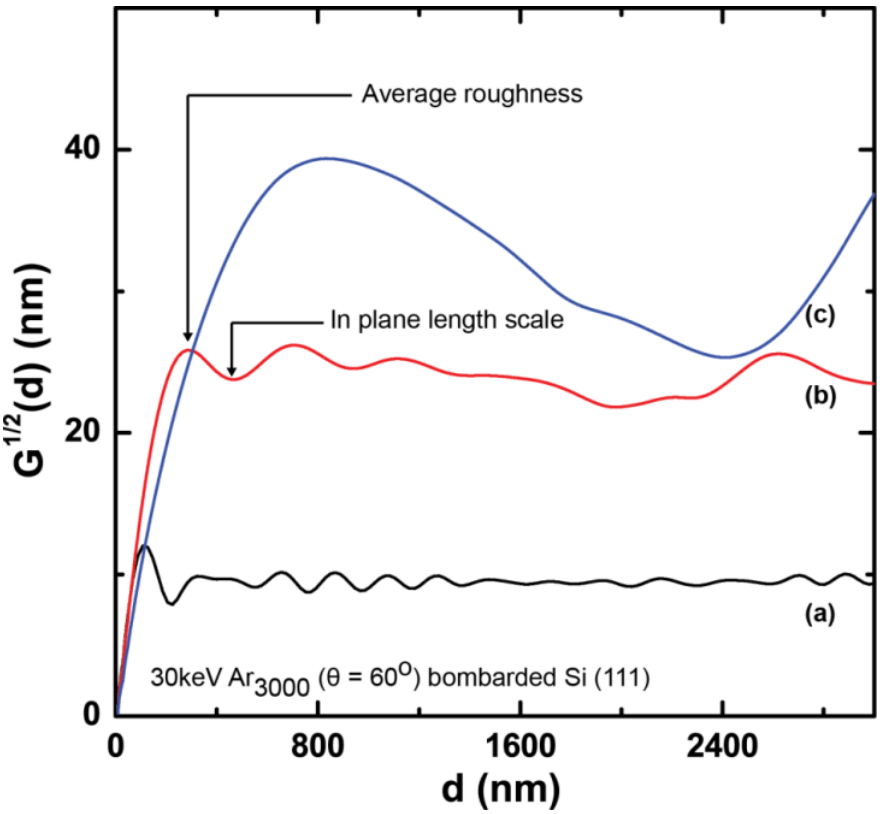

Figure 5.13: Square root of the height-height correlation function of the cluster ion beam bombarded Si (111) at doses (a) 1×10^{16} clusters/cm^2, (b) 1×10^{17} clusters/cm^2 and (c) 1 x 10^{18} clusters/cm^2 for cluster ion incident angle of 60^o. (i) The first local minimum of $G^{1/2}(d)$ gives a rough measurement of the surface wavelength $d = \lambda$ and (ii) The first maximum is the characteristic surface average roughness $r = G^{1/2}(\lambda/2)$ for a given ripple pattern [83].

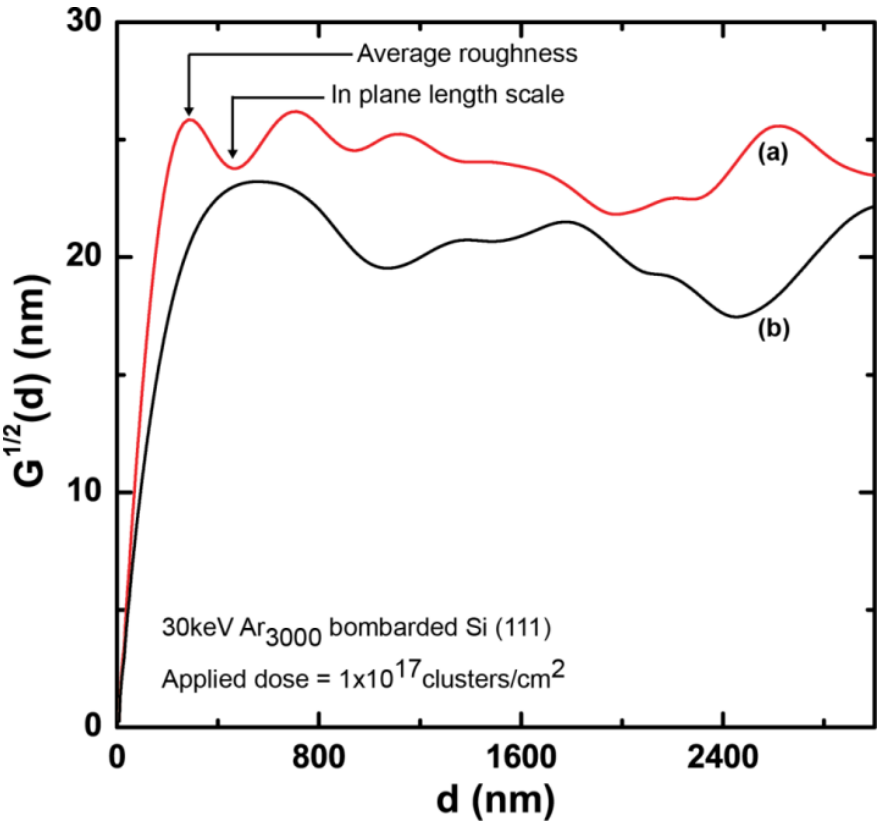

Figure 5.14: Square root of the height-height correlation function of the cluster ion beam bombarded Si (111) at dose 1×10^{17} clusters/cm^2 for cluster ion incident angles (a) 60^o and (b) 70^o.

Chapter 6

Morphological Evolution of Au Surfaces during Ar Cluster Ion Beam Bombardment

Evolution of Au surfaces during off-normal Ar_{3000} cluster ion beam bombardment is investigated. Nano-pattern formation depends on cluster ion angle of incidence, energy, and applied dosage. Cluster ion bombardment generates three surface processes: (1) Continuous sputtering of atoms, (2) Re-deposition of sputtered atoms, and (3) Surface diffusion. These processes provide a comprehensive explanation of cluster ion-induced nano-ripples on Au surfaces. In this chapter, we will present our experimental results on nano-ripple formation on Au surfaces and discuss a theoretical model on ripple formation.

6.1 Experimental Details

Au thin films deposited on Si (100) substrates (purchased from Sigma-Aldrich) were used in this experiment. Au orientation is technically polycrystalline with a preference to (111) orientation. Au thin film is bonded onto the Si substrate by an interfacial Ti adhesive layer. 0.5 × 0.5 cm^2 samples were cleaned and mounted in to the Gas Cluster Ion Beam (GCIB) system target chamber. Formation of Ar cluster ions by supersonic expansion is described in Chapter 3. Samples were bombarded with Ar cluster ions, each cluster ion carries about 3000 Ar atoms and the energy per atom was set to 10eV. Before the experiment the GCIB target chamber, nozzle chamber, and ionization chamber were vacuumed to 1×10^{-6} Torr, 4×10^{-8} Torr, and 1×10^{-8} Torr, respectively [1 Torr = 133.3 N/m^2]. Usually, the required target chamber pressure can be achieved in about 16 hours with the current experimental configuration.

Samples were mounted at tilt angles of 0^o to 80^o in steps of 10^o; here the tilt angle is the measured angle between the cluster ion beam direction and the sample holder. This angle corresponds to the cluster ion beam incident angle measured from the target surface normal. Each tilt sample was bombarded with 1×10^{16} clusters/cm^2 cluster ion dose to determine the maximum instability angle (θ_{max}). For Au we found that $\theta_{max} = 60^o$. During the experiment the beam current density was kept at 1 μA/cm^2 to prevent beam heating. The applied dose was varied from 1×10^{15} to 3×10^{16} clusters/cm^2 for incident angles 50^o, 60^o, and 70^o to determine the temporal evolution of nano-ripples on Au surfaces. The cluster ion energy dependence of nano-ripple structures was determined by comparing a 20 keV and 30 keV energy cluster ion beam at 50^o incident angle for

variable cluster ion beam dose.

The thermal effect on nano-ripples formed on Au surface was investigated by a modified sample stage and a target chamber, where temperature was varied from 220.3 K to 473.2 K for a constant angle (60^{o}) and dose (3×10^{16} clusters/cm^2).

Each sample was characterized by Atomic Force Microscopy (AFM) and Rutherford Backscattering Spectroscopy (RBS) to determine the root mean square roughness, wavelength, and Au thin film thicknesses after cluster ion bombardment. The Scanning Electron Microscope (SEM) was used to scan large surface areas to observe defects generated by contaminate particles.

6.2 Experimental Results and Discussion

6.2.1 Lateral Sputtering and Surface Smoothing Phenomena

Figure 6.1 (a) shows the AFM scan of the Au surface before Ar cluster ion beam bombardment; this non-bombarded polycrystalline Au surface has a Root Mean Square (RMS) roughness of 1.28 nm. Figure 6.1 (b) shows the AFM scan for the Au surface bombarded with Ar cluster ion beam normal to the surface. The applied dose was 2×10^{16} clusters/cm^2 dose and the energy of the beam was 30 keV. When cluster ions deposit normal to the surface, metallic, and semiconductor surfaces undergo smoothing processes [17], i.e. cluster ions interact with mounds on the surface and sputtering atoms fills up trenches [5]. The bombarded surface RMS roughness drops to 0.7 nm. Figure 5.1 (b) also

shows hillocks formed due to random accumulations and generation of spikes. Normal incident cluster ion collisions generate spike regions [87] that experience high pressure and high temperature transitions. In these regions the pressure can be in the order of 100 N/m^2 and temperature can rise up to 10^4 or 10^5 K [14] and produce large amounts of mobile target atoms. Figure 6.2 shows a schematic diagram of cluster ion beam bombardment at normal incidence. Mobile atoms sputter parallel to the surface "Lateral Sputtering" due to Ar atoms gaining lateral velocity components created by internal cascade collisions within a cluster [41]. To produce significant surface damage, the energy per atom should be greater than 2 eV [88]. These energies shock waves form and surface atoms sputter outward from a collision site.

Figure 6.3 shows random composite RBS spectra for random composite RBS spectra for the non-bombarded and Ar cluster ion beam bombarded at normal incidence for Au surfaces. The primary estimation of the Au film thickness for the non-bombarded sample is 93.8 ± 1.4 nm. Surface thickness reduces to 26.6 ± 1.4 nm when bombarded with 2×10^{16} clusters/cm^2 dose cluster ions normal to the surface. This large difference is attributed to lateral sputtering of the surface. Figure 6.4 illustrates amounts of layers removed due to sputtering, which is calculated by the difference between non-bombarded and bombarded surfaces. The sputtering is linear with applied dose and the amount of Au atoms sputtered per cluster ion is 21 atoms per cluster. The calculation was done assuming bulk density of Au as 5.9040×10^{22} atoms/cm^3. In comparison, a monomer ion beam of Ar^+ at 30 keV energy sputters 11 Au atoms per ion (calculated by SRIM 2012 software [89]).

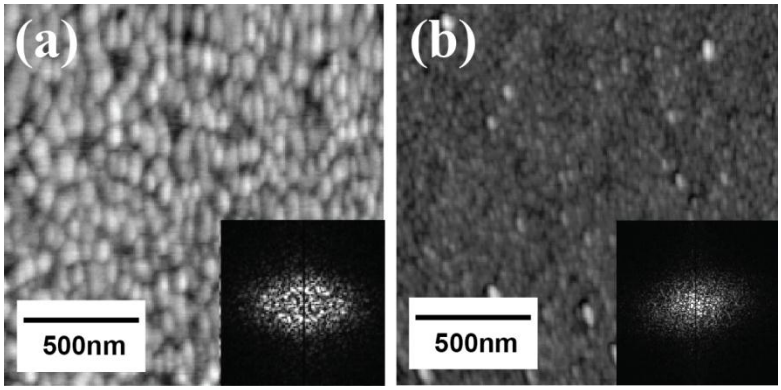

Figure 6.1: AFM scans of (a) non-bombarded polycrystalline Au surface and (b) Ar cluster ion beam smooth Au surface. The non-bombarded Au surface rms roughness is around 1.28 nm and when the surface is smooth with a normal incidence cluster ion with 30 keV energy for 2×10^{16} clusters/cm^2 dosage, the surface rms roughness reduces to 0.7nm. The hillock structures that exist in the smooth surface [as shown in (b)] are due to isolated accumulation of surface atoms. The scan area for all images is 1.6×1.6 μm^2

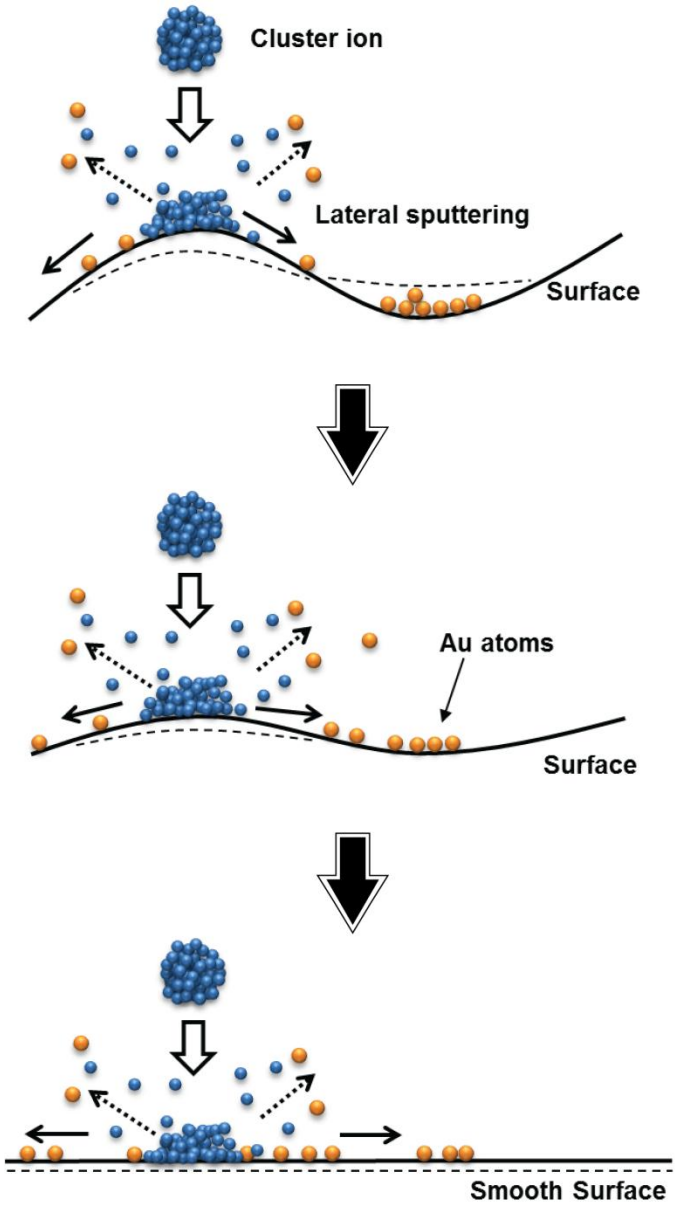

Figure 6.2: Schematic diagram of cluster ion surface interaction at normal incidence.

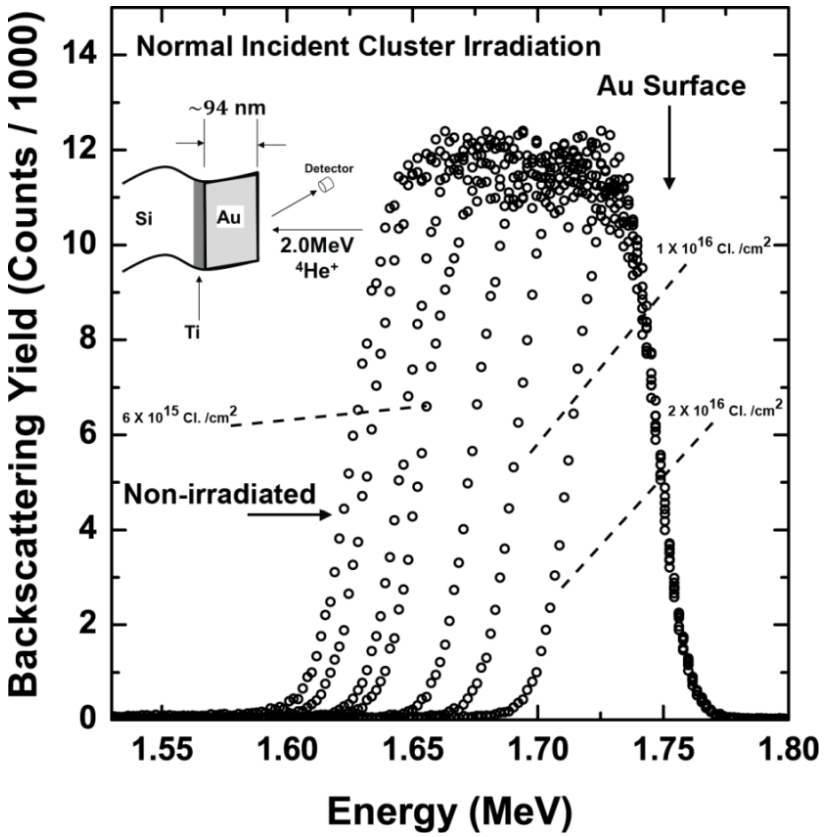

Figure 6.3: Random RBS spectra for 2.0 MeV ^{4}He ions incident on non-bombarded and six Ar cluster ion beam bombarded, at surface normal, Au thin film deposited on Si substrate. The Si signal and the signal for the Ti adhesion layer are not shown in the composite figure. The thickness of the non-bombarded sample is 93.8 ± 1.4 nm and after sputtering with 2×10^{16} clusters/cm^2 dosage the thickness of the film is 26.6 ± 1.4 nm. The atomic density of the Au thin film is considered as the bulk density of Au 5.9050×10^{22} atoms/cm^3.

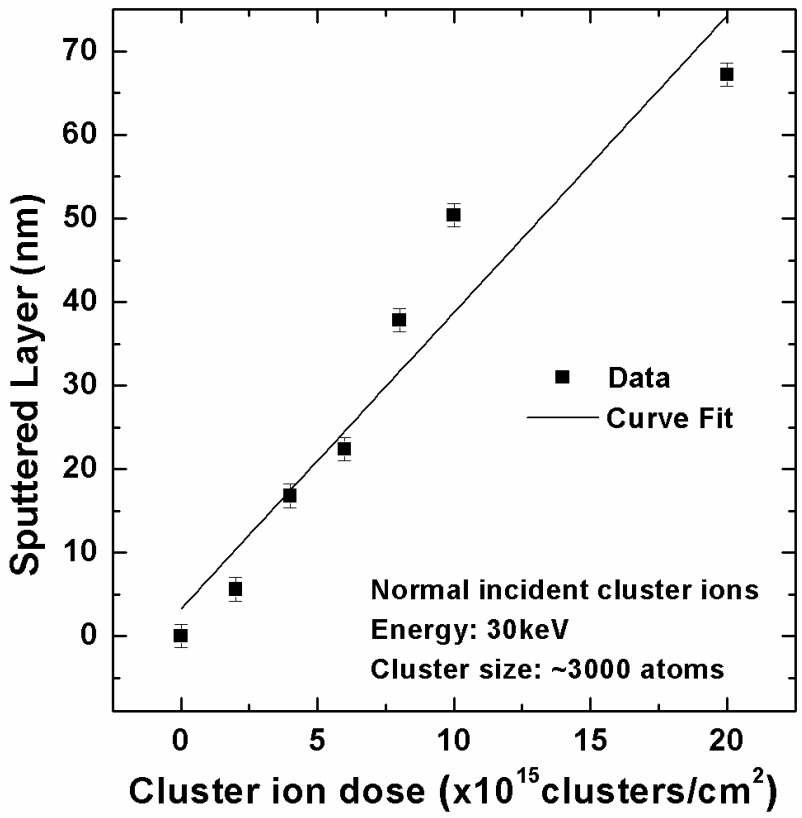

Figure 6.4: Amount of layers sputtered with applied dosage for normal incidence Ar cluster ion beam bombardment. The sputtered layer is calculated from the RBS spectra shown in Figure 5.3 by deducting thicknesses of bombarded Au thin films from non-bombarded thin film at each dosage. The linear curve fit calculation gives the average amount of target atoms removed from the surface during cluster ion bombardment, which are 21 atoms per cluster.

6.2.2 Ar Cluster Ion Beam Incident Angle Dependence

In general, off-normal cluster ion bombardment results in different processes on the surface due to the horizontal and vertical velocity components of colliding clusters that transfer momentum to the surface atoms such that atoms sputter at an angle. Figure 6.5 shows AFM scans of Ar cluster ion beam bombarded at different incident angles. AFM scans show significant cluster ion beam incident angle dependence. The maximum surface instability occurs at 60^{o} for Au surfaces.

Yamada et al. [17] showed that ripples begin to develop at a critical cluster ion incident angle of 10^{o}, but clear surface patterns are only observed beyond an angle of incidence of 40^{o} and patterns weaken after 60^{o} [Figures 6.5 (d) – (f)]. The ripple formation with incident angle can be understood by Fast Fourier Transform (FFT) images [Figure 6.5]. When a centered first peak appears in a Fourier image, the image shows an ordered pattern. The transition from non-ordered state to ordered state and then to non-ordered state as shown in Figure 6.5 (a) – (i) illustrates that the surface is ordered at a maximum instability angle of 60^{o}. Partially grown ripples as shown in Figure 6.5 (g) indicate weakening of cluster ion surface interactions. At grazing incident angles cluster ions interact with surface mounds and modifications occur without removing significant target atoms [90]. Figure 6.6 shows square root of height-height correlation function, $G^{1/2}(d)$, as a function of the length scale perpendicular to the ripple pattern, which show the ordering of surface patterns up to the maximum instability state at 60^{o}.

Figure 6.7 shows root mean square roughness dependence on the cluster ion beam incident angles from 0^o to 80^o measured from surface normal for a dose of 1×10^{16} clusters/cm^2. The surface roughness increases exponentially from 20^o to 60^o and decreases for angles larger than 60^o. The roughness at this critical angle (θ_{max}) is 9.12 nm for 1×10^{16} clusters/cm^2 dosage and this value increases to 17.03 nm for 3×10^{16} clusters/cm^2 dosage, for Au surface. This critical angle depends on the target material – e.g. for Si $\theta_{max} = 70^o$, and for Ag $\theta_{max} = 50^o$ [experimental details are not shown in this thesis]. Nano-ripples are formed due to low energy sputtering and surface diffusion of atoms. The surface diffusion of atoms is significant for the growth of cluster ion-induced ripples.

Furthermore, the initial surface roughness is irrelevant for nano-ripple development. A preliminary study conducted on $Si_{0.7}Ge_{0.3}$ by Chen in 2006 experimentally demonstrated nano-ripple formation on an initially flat surface [80]. The Bradley and Harper model [28] considers the initial surface curvature as well as isotropic thermal diffusion for pattern formation. However, the growth of ripples created by cluster ions does not depend on the initial surface curvature. The damage created on the surface mostly depends on the outermost atomic layer of cluster ions [91]. Thus, at an off-normal angle forward momentum transfer is driven by these outermost atomic layers of the cluster. Therefore, the wavelength of nano-ripples formed on Au surfaces exponentially increases with the cluster ion incident angle as shown in Figure 6.8. Wavelength for incident angles from 10^o to 80^o at 1×10^{16} clusters/cm^2 dosage varies between 54 nm and 242 nm.

Figure 6.9 shows composite RBS spectra for off-normal Ar cluster ion beam bombarded Au surfaces for incident angles 0^o to 80^o. The difference in the thickness between non-bombarded surfaces and bombarded surface provides the amount of Au atoms sputtered from a surface compared to incident angles for 1×10^{16} clusters/cm^2 dosage [Figure 6.10]. According to Toyoda et al. [17, 57] cluster ion sputtering behaves as a $\cos\theta$ function, whereas monomer ion sputtering follows a $1/\cos\theta$ function, which is described by the linear cascade theory [92, 93]. Figure 6.10 shows two break points at 20^o and 60^o, which indicate sputtering, may be slowed due to ripple formation between break points. Sputtering varies as a function of $\cos\theta$. In region III, cluster ions colliding at grazing incident angles only interact with surface mounds or near surface atoms and sputtering decreases to zero when the angle increase; this could be an effect due to partial transfer of energy or cluster ion reflection from the surface.

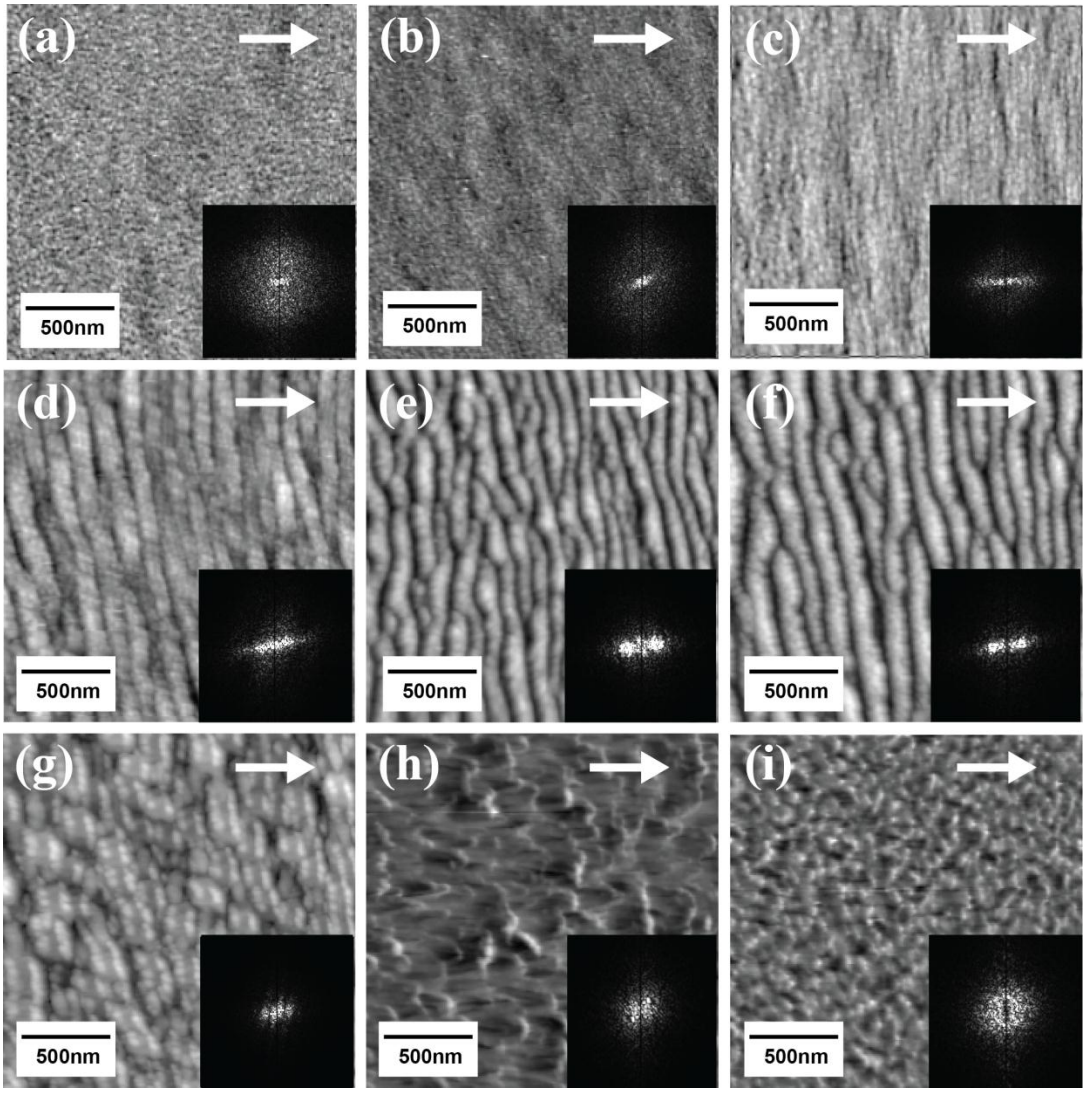

Figure 6.5: Atomic force microscope images of Ar cluster ion beam modified Au surfaces at different cluster ion incident angles (θ) with 1×10^{16} clusters/cm^2 dosage and energy of 30keV per cluster ion: (a) 10^o, (b) 20^o, (c) 30^o, (d) 40^o, (e) 50^o, (f) 60^o, (g) 65^o, (h) 70^o and (i) 80^o from surface normal. Beyond 60^o surface structures are disoriented. Inserted FFT images show the ordering and disordering of surface structures with the cluster ion incident angle. The arrow denotes the direction of incident cluster ions. The scan area for all images is 1.6×1.6 μm^2.

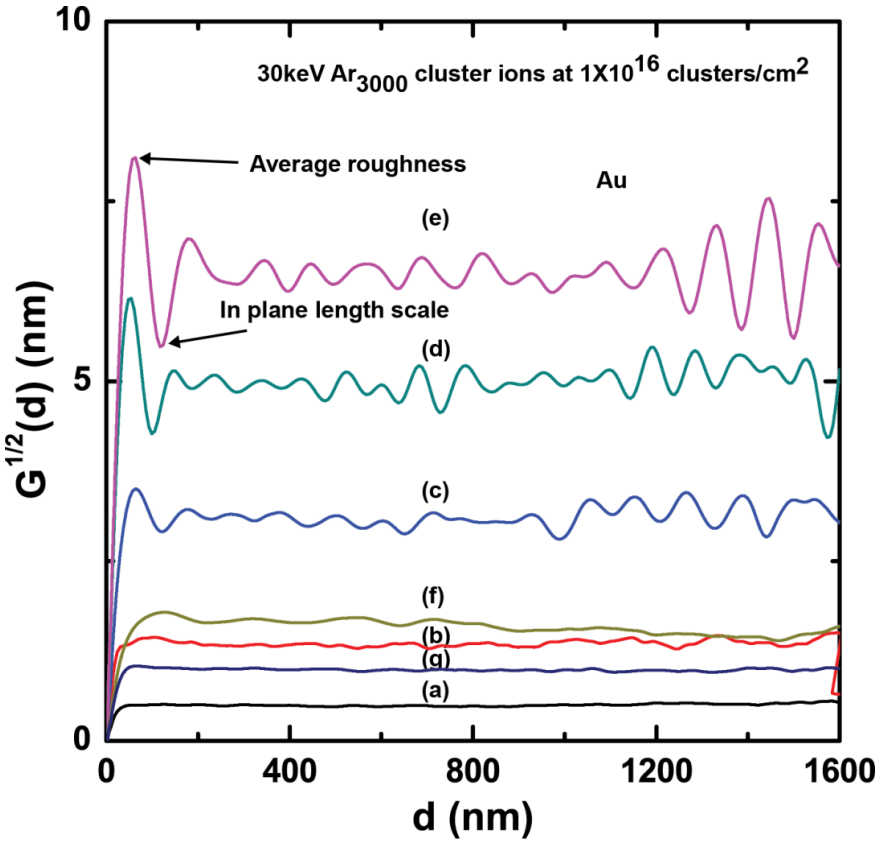

Figure 6.6: Square root of the height-height correlation function of the cluster ion beam bombarded Au surfaces at doses 1×10^{16} clusters/cm^2 for cluster ion incident angles of (a) 0^o, (b) 30^o, (c) 40^o, (d) 50^o, (e) 60^o, (f) 70^o, and (g) 80^o. (1) The first local minimum of $G^{1/2}(d)$ gives a rough measurement of the surface pattern wavelength $d = \lambda$. (2) The first maximum is the characteristic surface average roughness $r = G^{1/2}(\lambda/2)$ for a given ripple pattern.

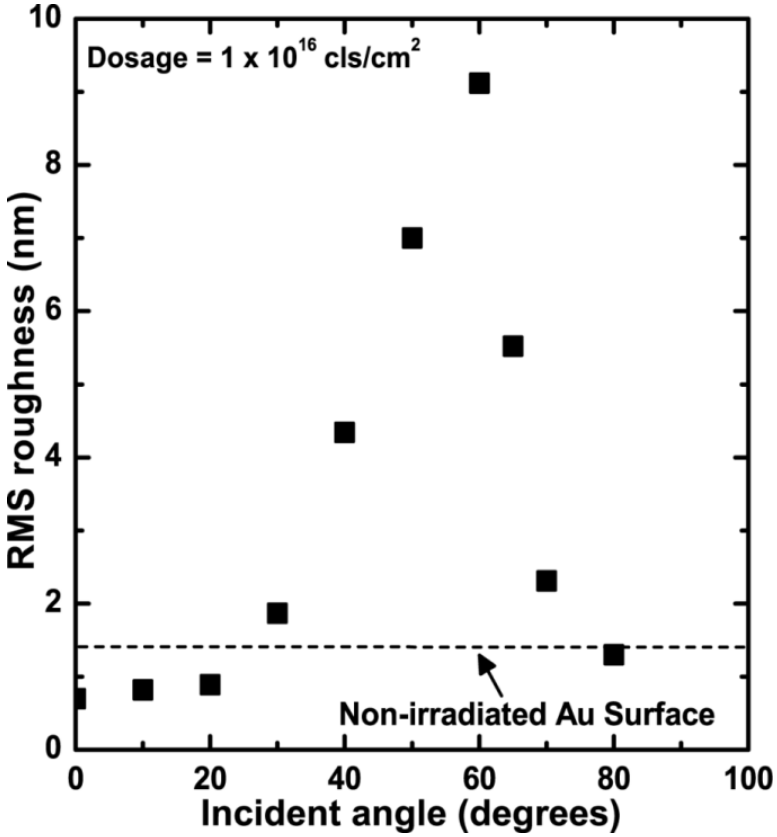

Figure 6.7: RMS roughness of the Au surface with the cluster ion incident angle. After 60^{o} the surface roughness reduces considerably and this threshold angle depends on the target material.

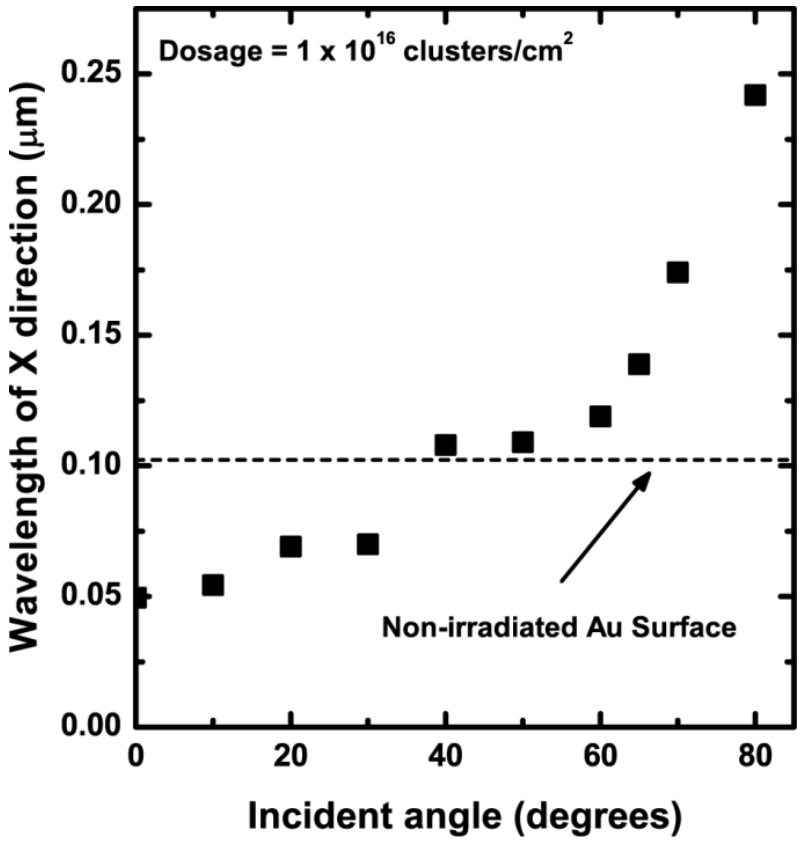

Figure 6.8: Surface wavelength in the x-direction, which is perpendicular to the ripple structures. The wavelength exponentially increases with incident cluster ion beam angle.

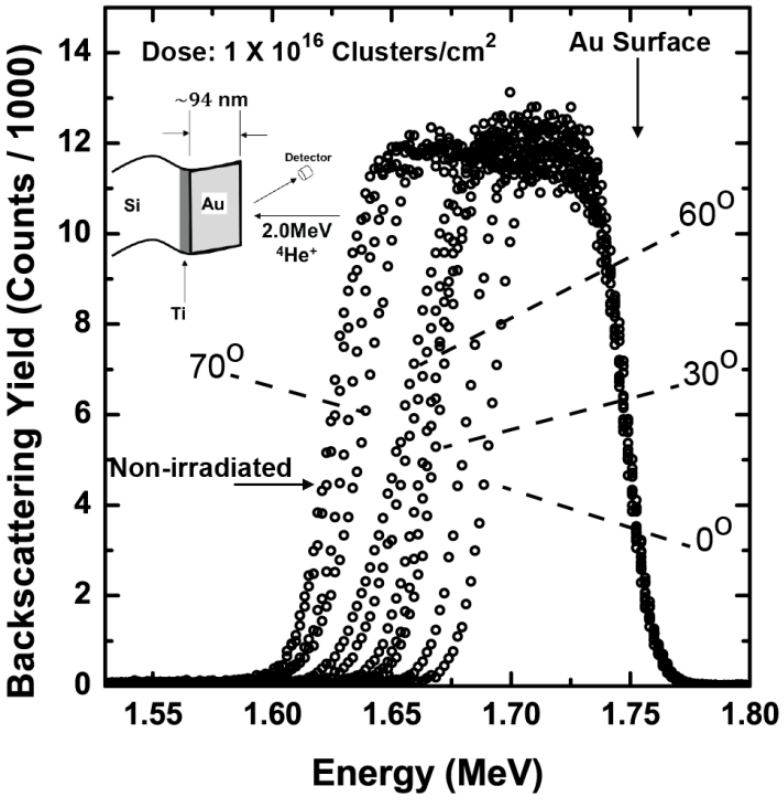

Figure 6.9: Random RBS spectra for 2.0 MeV ^{4}He ions incident on non-bombarded and 10 Ar cluster ion beam bombarded at different incident angles 0^o to 80^o. The Si signal and the signal for the Ti adhesion layer are not shown in the composite figure.

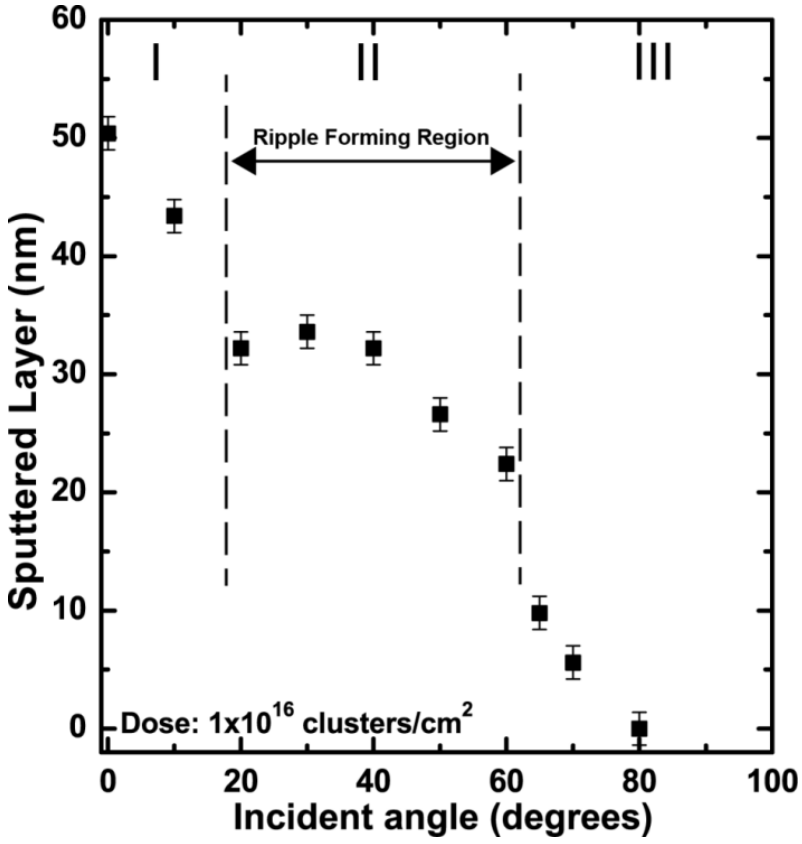

Figure 6.10: Angular dependence of sputtering of Au thin film by Ar cluster ion beam at 1×10^{16} clusters/cm^2 dosage. Amount of Au atoms removed is calculated with comparison to a non-bombarded Au thin film by RBS analysis. The sputtering variation with the cluster ion angle is classified into three regions. Region II (20^o – 60^o) is the ripple formation region.

6.2.3 Evolution of Nano-ripples with Applied Ar Cluster Ion Dose

The evolution of nano-ripples with applied dosage is shown in Figures 6.11 (b) – (i). Ripple structures initially as shown in Figure 6.11 (b) are highly dislocated due to random cluster ion collisions – i.e. each collision sputters atoms at an angle and creates a ripple with certain amplitude due to initial randomness structures that carry different amplitude modes (domains). The boundary between these amplitudes is known as a domain wall.

An important question that arises is how these ripples coalesce to form long ordered structures with continuous bombardment. A possible solution for ordering draws on the superposition of amplitude mode dislocations due to surface instability and growth of ripples with the expense of neighboring domains [94]. Figure 6.11 (i) shows a significant improvement in ripple ordering at 3×10^{16} clusters/cm^2 dosage bombarded at 60^o Ar cluster ion beam incident angle. Corresponding Fourier transform images [Figure 6.11] show the ordering of ripples with bombardment dose. For sharper and uniform ripple patterns, the radial width of the Fourier peak becomes smaller [39]. Figure 6.12 shows the square root of height-height correlation function, $G^{1/2}(d)$ that indicates with dosage ripples become more ordered. Figure 6.13 shows the RMS roughness of ripple patterns as a function of applied Ar cluster ion beam dosage for incident angles of 50^o, 60^o, and 70^o. For a sinusoidal surface pattern according to Carter's shadowing effect model [36], to satisfy the $\tan(\pi/2 - \theta) \geq 2\pi h_o/n$ term aspect ratio of ripples should be 0.13, 0.09, and 0.06 for 50^o, 60^o, and 70^o, respectively. However, cluster ion-induced nano-ripples on Au surfaces saturate at very low dosages as shown in Figure 6.15. For example, for

cluster ions incident at 60^{o}, the limiting condition to avoid saturation occurs at 2×10^{14} clusters/cm^2. Therefore, the experimental parameters were varied in the saturated or non-linear regime. Figure 6.14 shows the wavelengths in the x-direction (the direction of cluster ion incidence) of surface ripple patterns. During the ripening process ripples merge by superposition of neighboring ripple domains, which create more domain boundaries before the production of coalescence ripples. This transition is shown in Figures 6.11 (d) – (f). Figure 6.16 illustrates a schematic diagram of ripple formation during cluster ion beam off-normal bombardment.

Preliminarily target Au surface atoms undergo three sputtering processes and the formation of ripples are due to atoms that sputter with low energies and ripples grow due to surface diffusion of target atoms. Beyond the limiting condition, cluster ion bombardment and surface atom sputtering depends on the local surface slope. Cluster ions colliding with surface mounds or in this case ripple structure peaks, sputter atoms and the ripple growth slows down. However, cluster ions colliding the upstream of ripples (upstream is defined as the ripple slope facing the cluster ions beam) produce mobile atoms that accumulate upstream. This ripening process depends upon the cluster ion applied dosage (Figure 6.17) and incident angle (Figure 6.18). The ripple maximum height to width ratio (H/W) increases from 0.27 to 0.41 when the applied dose changes from 1×10^{16} clusters/cm^2 to 3×10^{16} clusters/cm^2. Nevertheless, H/W ratio decreases to 0.19 for cluster ion incident angles of 50^{o}. This is caused by the high sputtering rate at 50^{o} (12 atoms/cluster) compared to 60^{o} (7 atoms/cluster), calculated from the slopes of Figure 6.19. For 70^{o} grazing incident angle, cluster ion beam sputtering rate decreases to

2 atoms/cluster, and the upstream accumulation reduces as a result of geometrical shadowing.

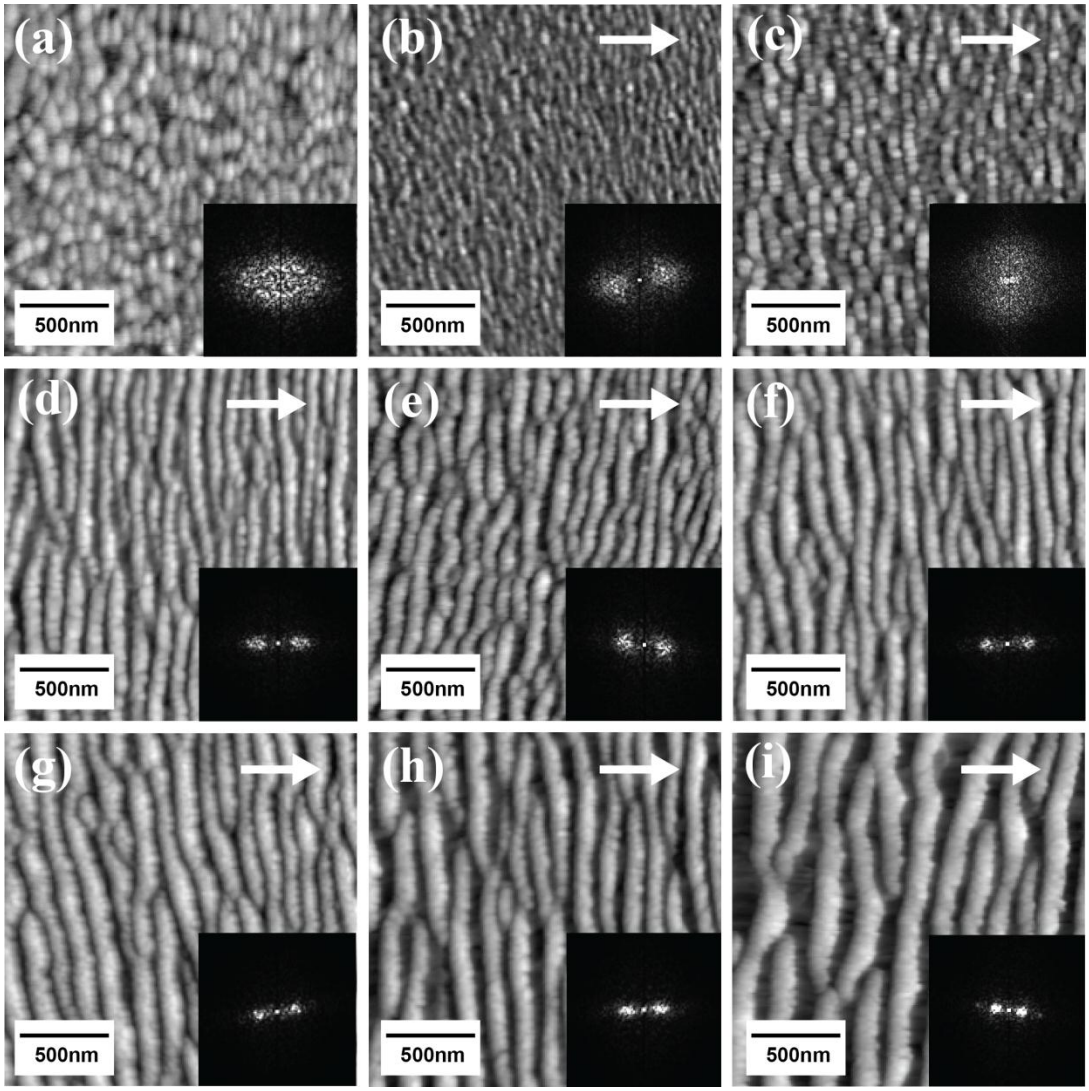

Figure 6.11: Atomic force microscope images of Au surfaces (a) non-bombarded polycrystalline surface, and Ar cluster ion beam modified Au surfaces at different dosages with 60^{o} incident angle and energy of 30keV per cluster ion (b) 0.1, (c) 0.2, (d) 0.4, (e) 0.6, (f) 0.8, (g) 1, (h) 2, and (i) 3, $\times 10^{16}$ clusters/cm^2. The inserted FFT images show thinning of radial width of the Fourier peak, which indicate the ordering of ripples structures with applied cluster ion dose. The arrows denote the direction of cluster ions. The scan area for all images is $1.6 \times 1.6\mu m^2$.

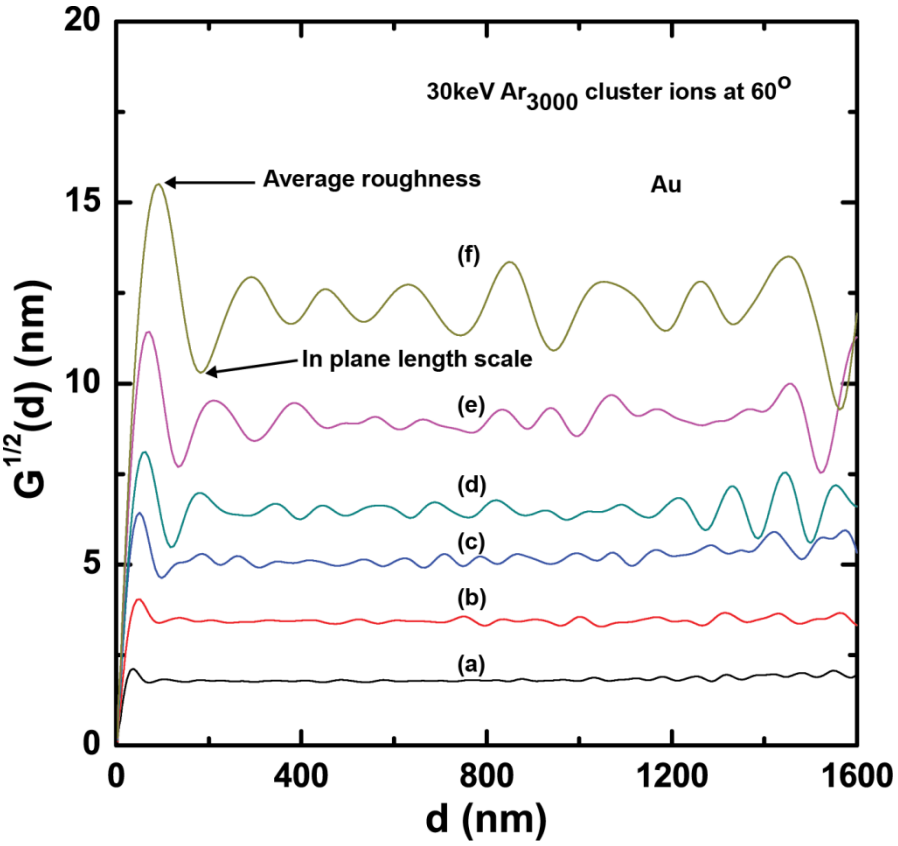

Figure 6.12: Square root of the height-height correlation function of the cluster ion beam bombarded Au surfaces at doses (a) 1×10^{15} clusters/cm^2, (b) 2×10^{15} clusters/cm^2, (c) 4×10^{15} clusters/cm^2, (d) 1×10^{16} clusters/cm^2, (e) 2×10^{16} clusters/cm^2, and (f) 3×10^{16} clusters/cm^2 for cluster ion incident angles of 60^o. (i) The first local minimum of $G^{1/2}(d)$ gives a rough measurement of the surface pattern wavelength $d = \lambda$, and (ii) The first maximum is the characteristic surface average roughness $r = G^{1/2}(\lambda/2)$ for a given ripple pattern.

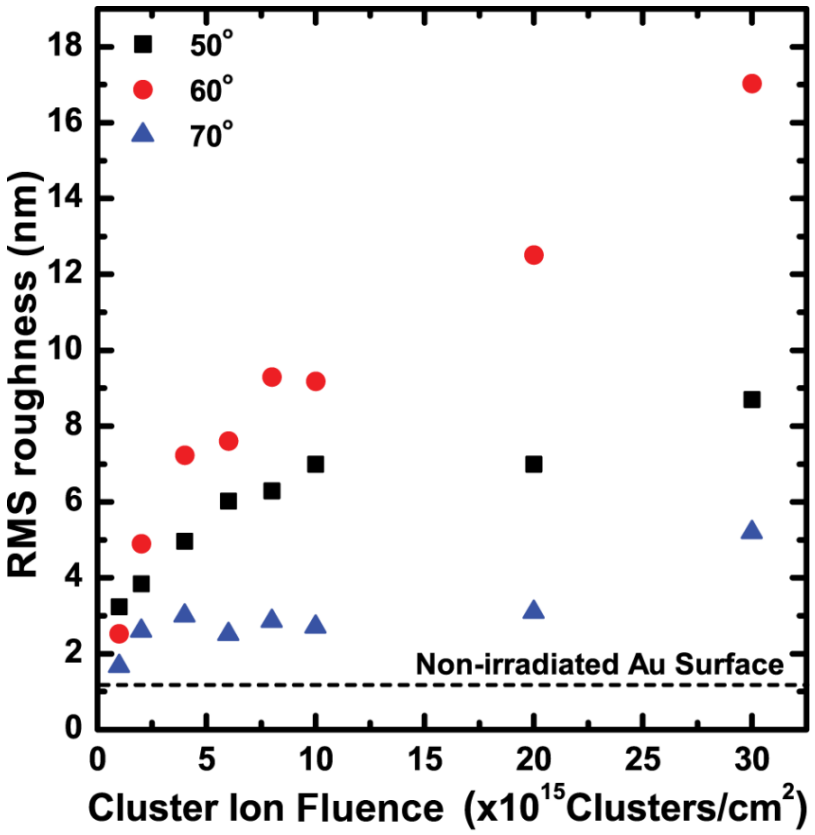

Figure 6.13: RMS roughness at the threshold angle of 60^{o} remains higher than 50^{o} and 70^{o} with dose. Compared to 60^{o}, surface roughness saturates prematurely for 50^{o} and 70^{o}.

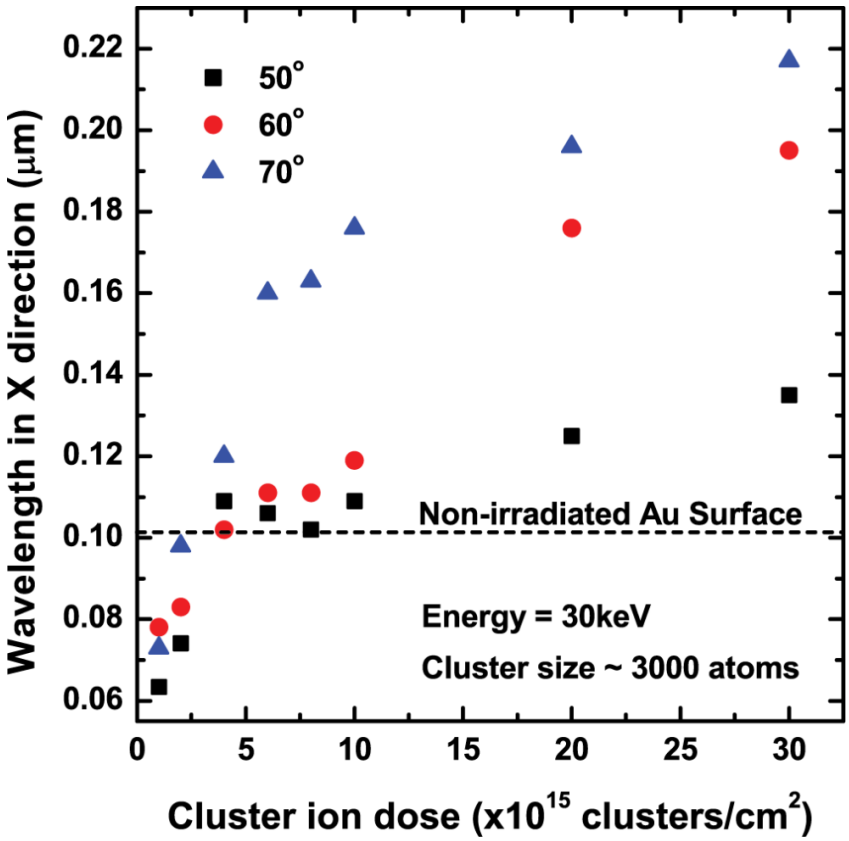

Figure 6.14: Surface wavelength in the x-direction, which is perpendicular to the ripple structures. Initially the wavelength exponentially increases with applied dosage and saturates at higher dosages. According to the curves wavelengths increases with the Arcluster ion beam incident angle.

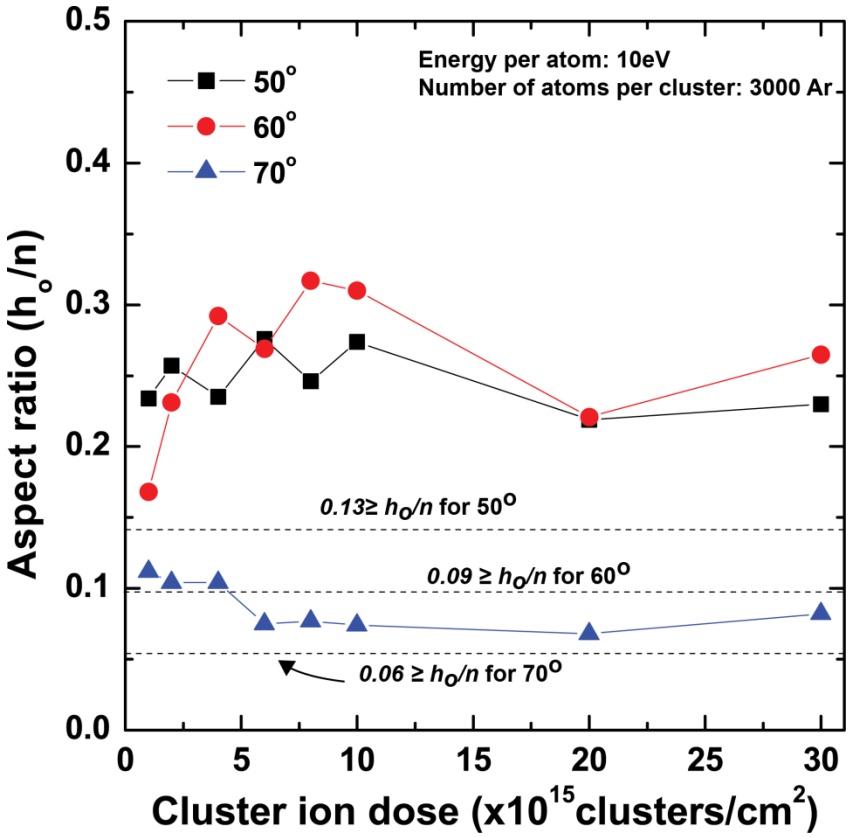

Figure 6.15: Aspect ratio of surface structures on Au thin film as a function of dose for 50°, 60°, and 70° incident angles. Here the aspect ratio is defined as the ratio between roughness amplitude and wavelength, assuming a sinusoidal surface pattern.

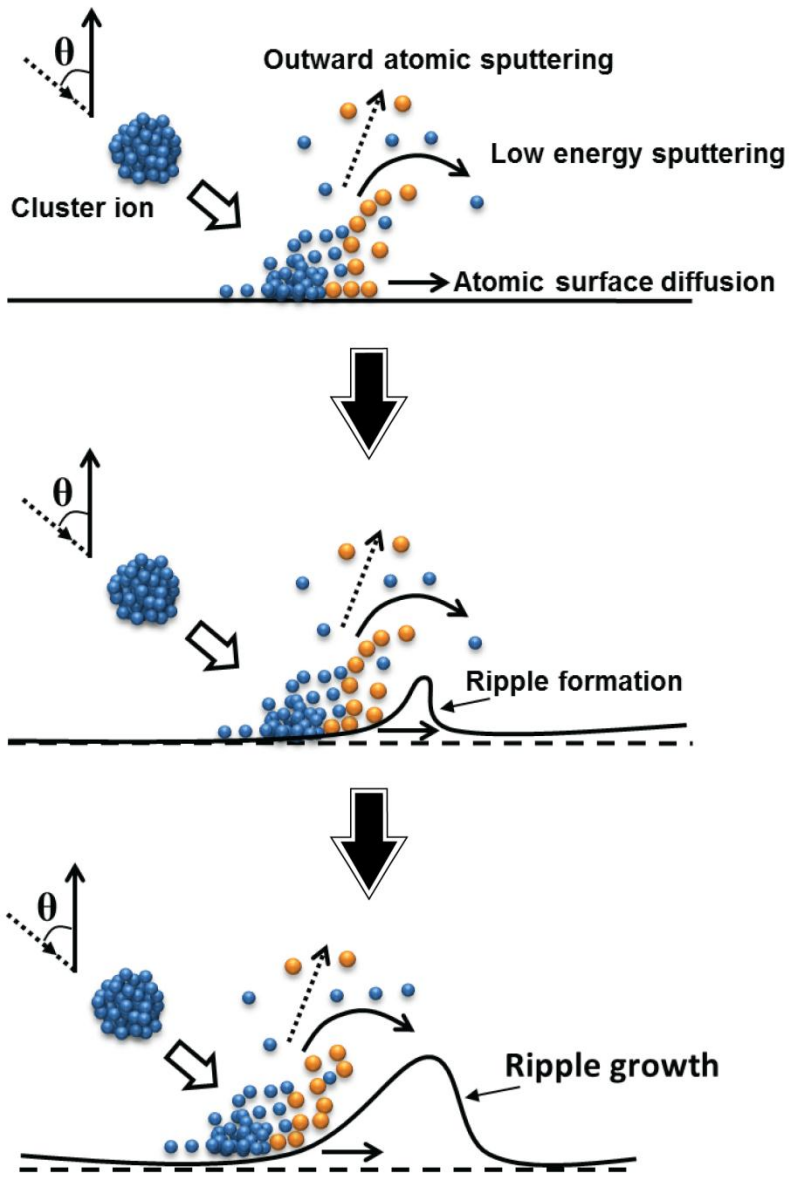

Figure 6.16: Schematic diagram of cluster ion surface interaction at off-normal incidence.

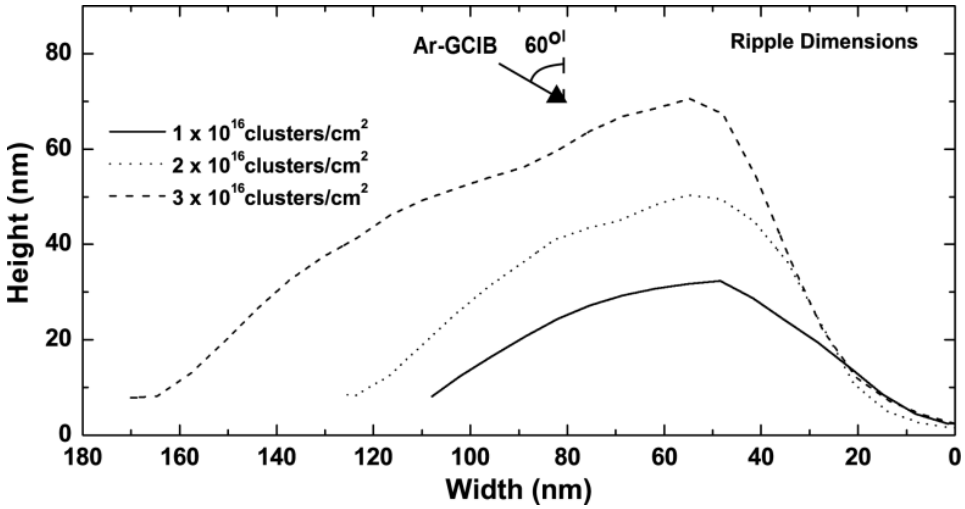

Figure 6.17: Composite AFM image cross section of a ripple on Au surfaces formed due to Ar cluster ion beam bombardment at 1, 2, and 3 × 10^{16} clusters/cm^2 dosages for 60^o incident angle.

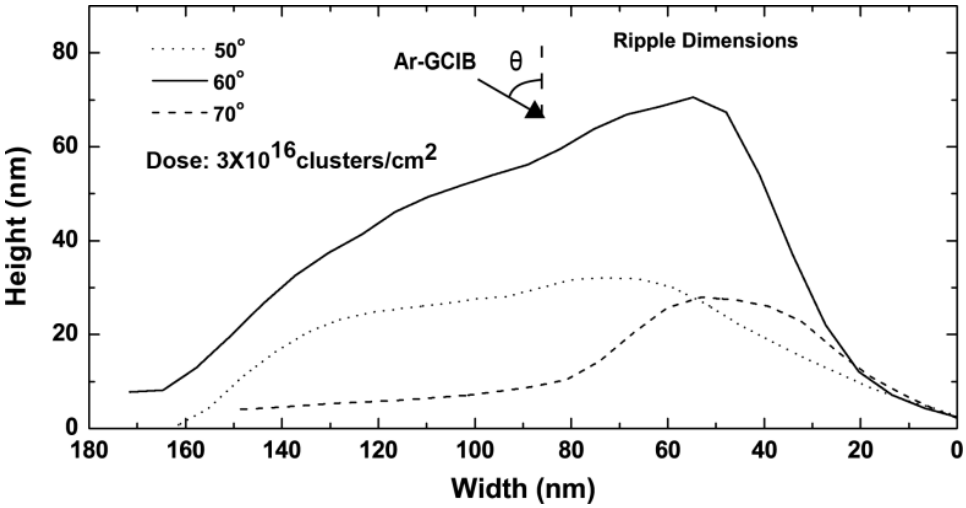

Figure 6.18: Composite AFM image cross section of a ripple on Au surfaces formed due to Ar cluster ion beam bombardment at 3 × 10^{16} clusters/cm^2 dosage for 50^o, 60^o, and 70^o incident angles.

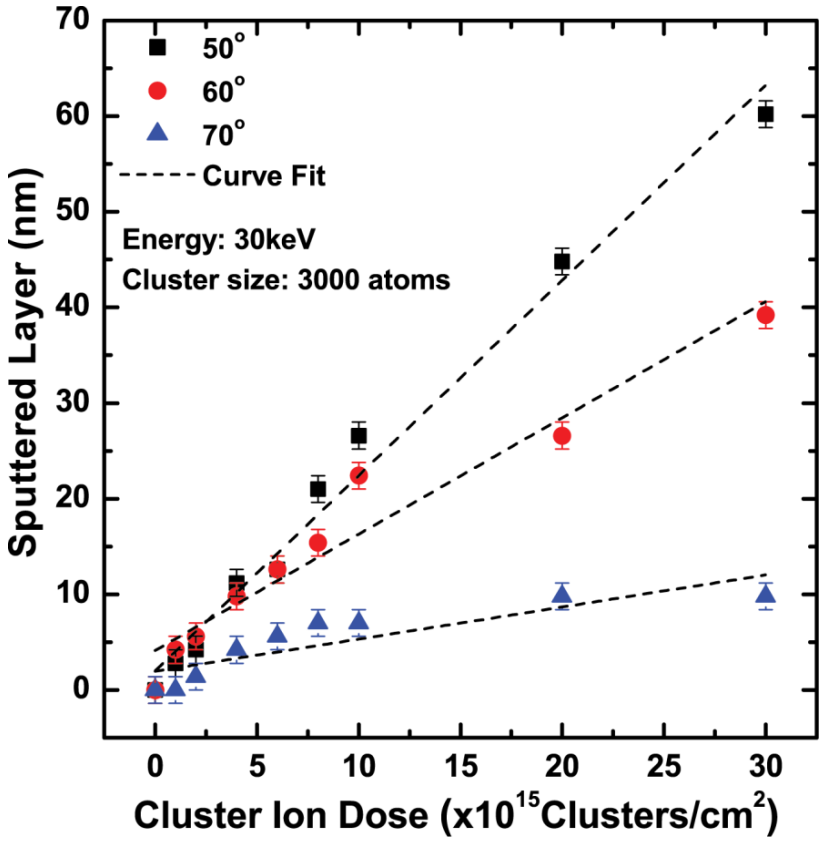

Figure 6.19: Dose dependence of sputtering Ar cluster ion beam incident angles $\theta = 50^{o}$, 60^{o} and 70^{o}.

6.2.4 Ar Cluster Ion Beam Energy Dependence

Figure 6.20 shows the acceleration energy dependence of surface sputtering of Au for energies of 20 keV and 30 keV at 50^{o} incident angle. The dose was varied from 1×10^{15} clusters/cm^2 to 3×10^{16} clusters/cm^2 and the size of the Ar cluster was 3000 atoms/cluster. Then the energy per atom varies from 6.67 eV to 10 eV. For both energies, the sputtering rate fluctuated linearly with the applied dose. The sputtering rate for 20 keV energy is 11 atoms/cluster and for 30 keV it is 12 atoms/cluster. Also the roughness variation is similar between for the energies up to 1×10^{16} clusters/cm^2 as shown in Figure 6.21. This is in good agreement with previous results by Toyoda et al. [90]. Monomer ion sputtering creates knock-on cascades, which form inside the material. This produces large amounts of defects within the material. On the other hand cluster ions interact with surface atoms and all of the energy is deposited. The complete energy deposition leads to reduction in the roughness for doses higher than 1×10^{16} clusters/cm^2

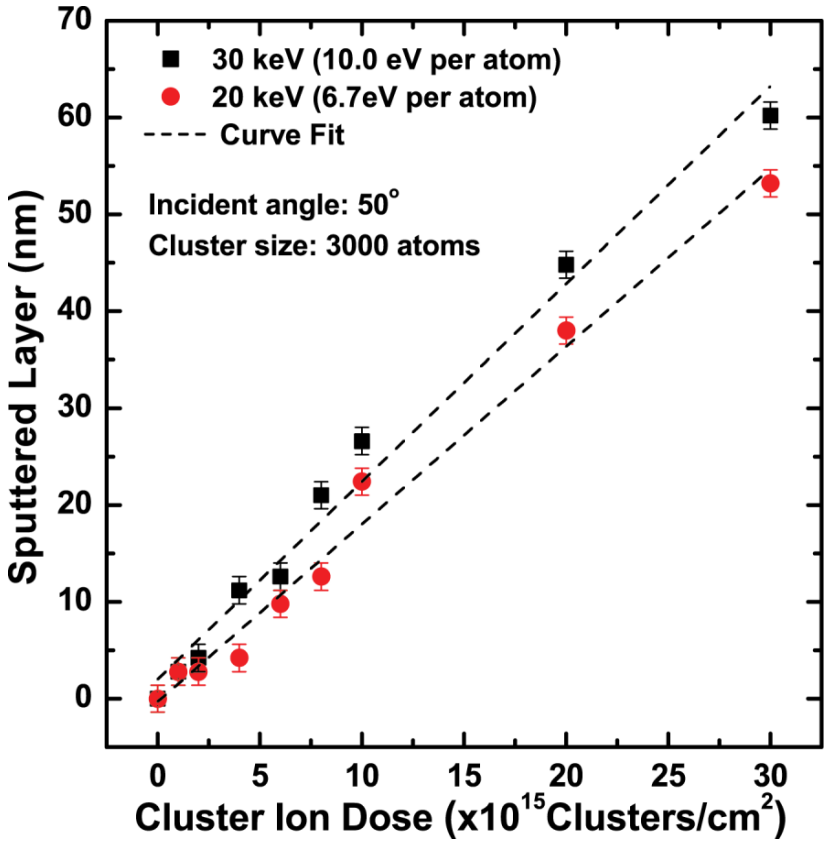

Figure 6.20: Sputtering of the surface Au atoms with the applied dosage at 20 keV and 30 keV cluster ion energies at 50^{o} cluster ion angle of incidence, here energy per atom in a cluster ion is 6.7 eV and 10.0 eV respectively.

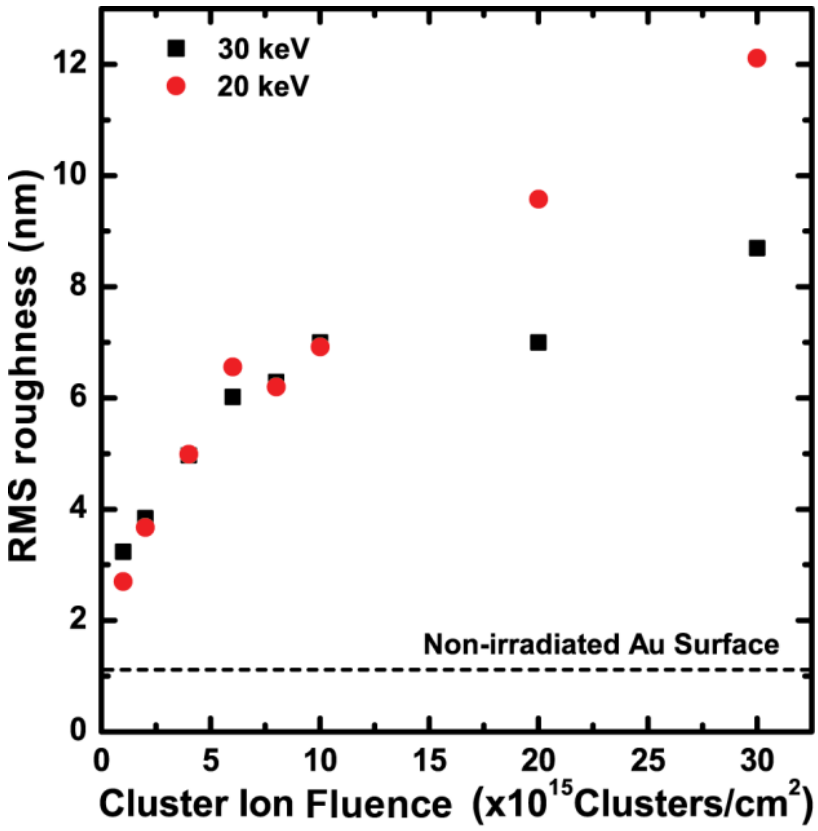

Figure 6.21: RMS roughness as a function of cluster ion dose at 20 keV and 30 keV energy.

6.2.5 Cluster Ion-induced Effective Surface Diffusion

Figure 6.22 shows a SEM image of a cluster ion beam bombarded surface with 2×10^{16} clusters/cm^2 at 60^o incident angle. The hair line features in the front end of the ripples indicate that surface atoms diffuse in the direction of cluster ion beam deposition. When cluster ions collide with the surface at an off-normal incidence large amounts of mobile atoms are generated and these atoms are responsible for ripple formation and surface diffusion. Since the total Au sample is exposed to the cluster ion beam, the entire surface can be considered as an amorphous and viscous layer of mobile atoms. For amorphous surfaces the Ehrlich-Schwoebel barrier [95, 96] is inactive [82]. However, for cluster ions the initial crater boundaries acts as step edges [35] for triggering ripple formation. To understand the ripple formation a solid micro particle was placed on Au surface as shown in Figure 6.23 (a). The micro particle shadowed the incident cluster ion beam. SEM analysis of this surface shows a region of ripple structures and a non-bombarded polycrystalline region on the downstream of the particle [Figure 6.23 (b)]. Figure 6.23 (c) shows a partially formed ripple pattern caused by backscattering Ar cluster ions and Ar atoms from the particle upstream side.

The Rutherford Backscattering Spectroscopy (RBS) analysis revealed that the off-normal cluster ion beam bombarded Au thin films has a surface gradient as shown in Figure 6.24. The bombarded surface was scanned across the sample in the direction of cluster ion incidence (1→4) and the thin film surface thicknesses were measured at four locations 2 mm apart. Figure 6.25 illustrates the dose dependence of the surface gradient which is only distinctive at higher cluster ion beam dosages. Figure 6.24 spectrum-1 show the Au

peak intensities reduced compared to the non-bombarded surface. Hence, it appears likely that the cluster ion beam sputtering of the Au thin film has exposed the interfacial Ti layer and Si substrate. Figure 6.26 (b) shows the x-ray photoelectron spectroscopy survey spectrum of Au surface bombarded with 3×10^{16} cluster/cm^2 at 50^o incident angle, which corresponds to spectrum 1 in Figure 6.24. Ti and Si intensity lines appear due to the exposure of secondary layers. These intensity lines were not observable for the location 4 (spectrum 4 Figure 6.24) [Figure 6.26 (a)]. O 1s and C 1s intensity lines appear as a result of exposure of bombarded Au surface to the ambient environment. Even though the surface forms a gradient over the length scale of the sample, the root mean square roughness measurements at locations 1 to 4 of the surface shows comparable values.

Surface gradients were also observed for 60^o and 70^o cluster ion beam incident angles [Figure 6.27]. Viscous flow of surface mobile atoms has been modeled for monomer ion beam surface interactions and ripple formation [97] but existence of these active layers has not been demonstrated experimentally. The surface gradient of the cluster ion bombarded surface is generated due to mobile surface atoms and creation and flow of these atoms are due to impacting cluster ions. The surface gradient is noticeable for applied dosages greater than 1×10^{16} clusters/cm^2. Calculated values of the surface gradients as a function of dose and incident angles are given in Table 6.1 and Table 6.2.

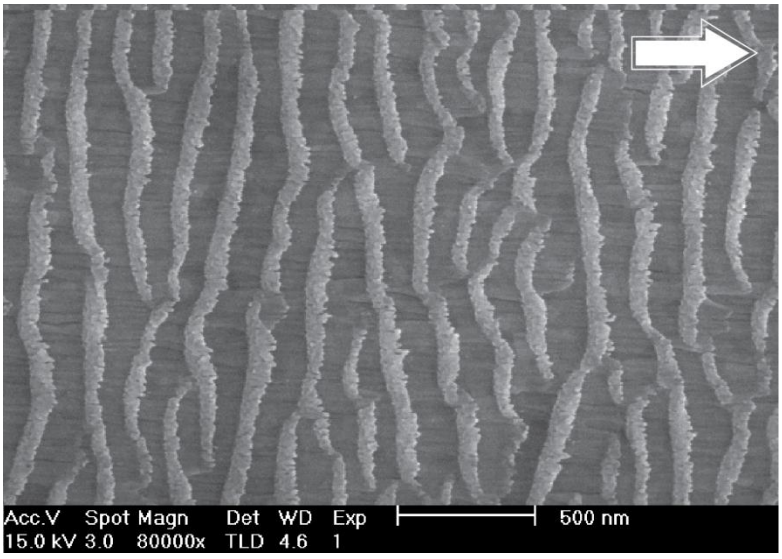

Figure 6.22: SEM image of nano-ripple formation on Au surface with Ar cluster ion beam bombarded at 60^{o} incident angle and 2×10^{16} clusters/cm^2 dosage.

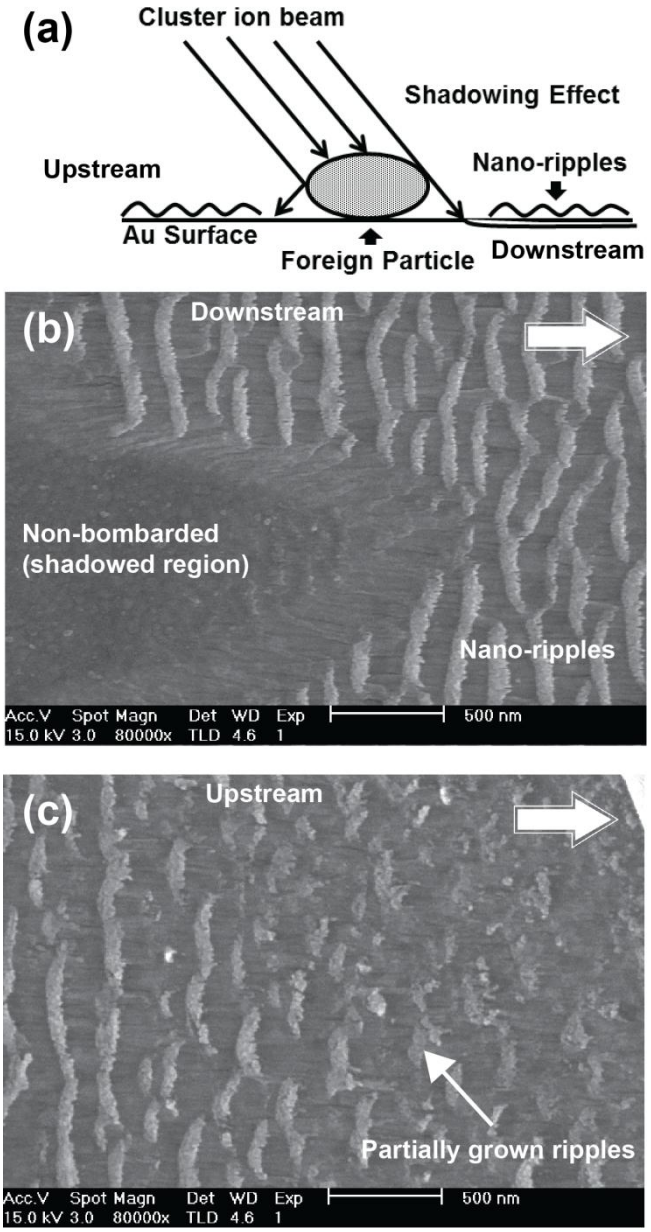

Figure 6.23: (a) a micro-size particle is placed to generate a shadowing effect on the surface, (b) the front end or downstream of the micro-size particle show an undamaged polycrystalline region and rippled region on Au surface. (c) The back end or upstream of the micro particle show damaged ripple structures due to backscattering of cluster ions.

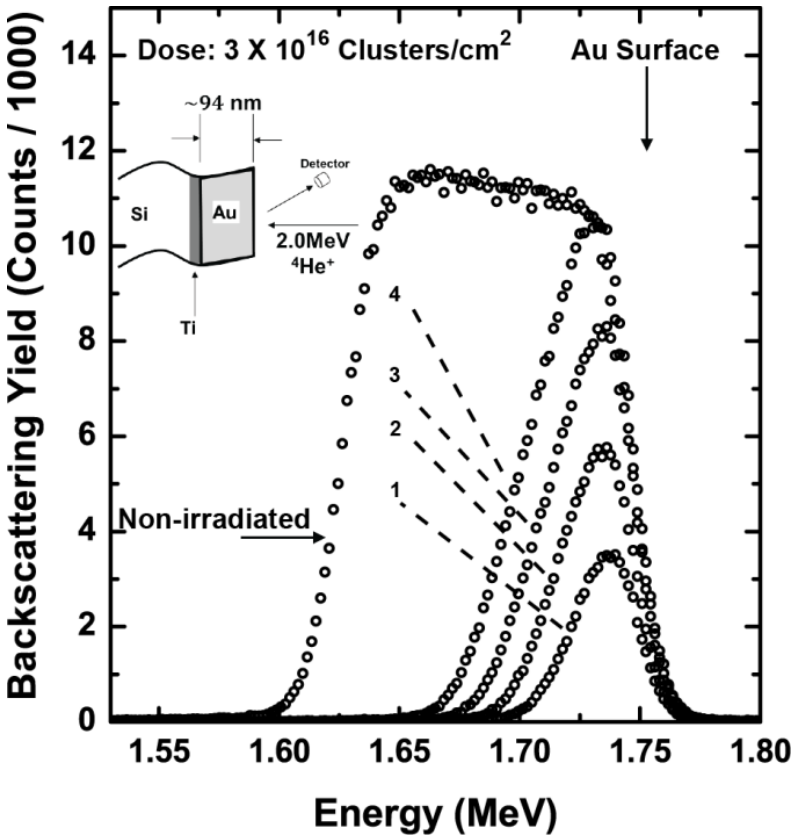

Figure 6.24: Random RBS spectra for 2.0MeV 4He ions incident on non-bombarded and Ar cluster ion beam bombarded at 50^{o} incident angle from the surface normal with 3×10^{16} clusters/cm^2 dosage. Bombarded surface was scanned across the sample in the direction of cluster ion incidence (1→4) and the thin film surface thicknesses were measured at four locations. The Si signal and the signal for the Ti adhesion layer are not shown in the composite figure.

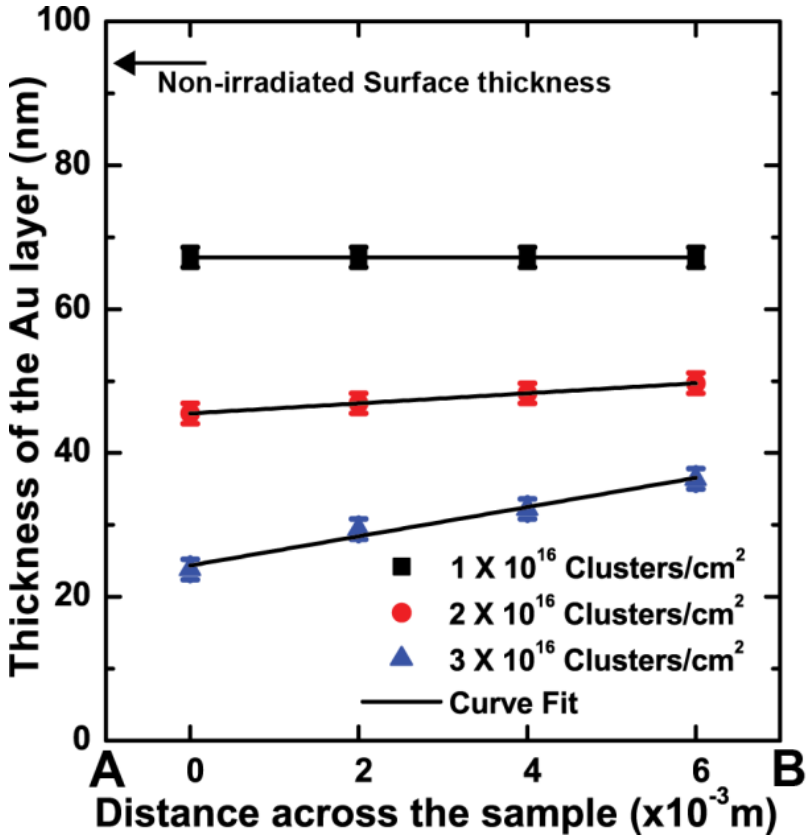

Figure 6.27: Thickness of Au thin film after bombarded with (a) 1, (b) 2, and (c) 3×10^{16} clusters/cm^2 at 50^o cluster ion angle of incidence. Thickness was measured 2mm apart in the direction A to B (cluster ions arrive onto the surface in this direction).

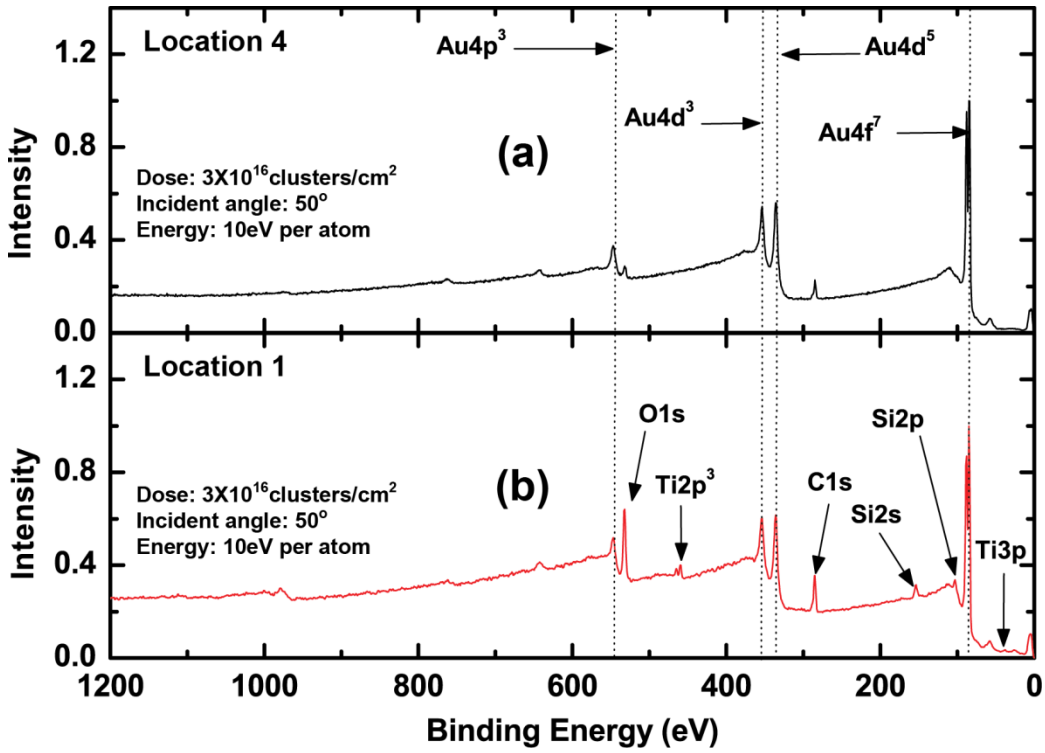

Figure 6.26: A survey x-ray photoelectron spectra for Cluster ion beam bombarded at 50^{o} from the surface normal with 3×10^{16} clusters/cm^2. Au binding energy signals are Au $4p^3$, $4d^3$, $4d^5$, and $4f^7$ (a) Location 4 and (b) Location 1 corresponds to the RBS spectrum 4 and spectrum 1 in Figure 6.24. At Location 1 surface was discolored due to exposure of interface Ti layer and Si substrate. O 1s and C 1s signal are due to contaminates when Au surface exposed to the ambient environment.

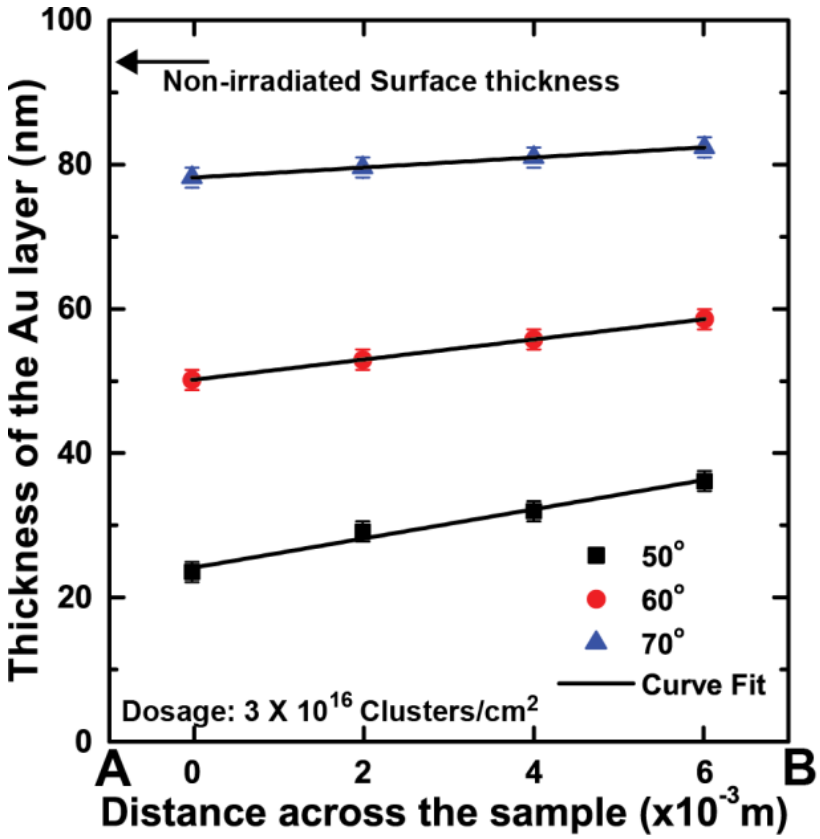

Figure 6.27: Thickness of Au thin film after bombarded with 3 × 10^{16} clusters/cm^2 dosage at 50^o, 60^o and 70^o cluster ion beam incident angles. Thickness was measured 2mm apart in the direction A to B (cluster ions arrive onto the surface in this direction).

Table 6.1: The gradient of the Au surface as a function of dose at 50^o cluster ion beam incident angle.

Dose [× 10^{15} clusters/cm^2]	Surface gradient (nm/mm)
10	-
20	0.70
30	2.03

Table 6.2: The gradient of the Au surface as a function of incident angle of the cluster ion beam with a dosage of 3×10^{16} clusters/cm^2.

Incident angle [degrees]	Surface gradient (nm/mm)
50	2.03
60	1.40
70	0.70

6.2.6 Temperature Effect on Nano-ripple Formation on Au Surfaces

During the process of Ar cluster ion-induced nano-ripple formation overall Au surface temperature remains at about room temperature (24.5^{o}C), despite the fact that a single cluster ion impact creates instantaneous temperatures rise to 10^5 K [14]. Here we investigated Au nano-ripples and the surface gradient as functions of the surface temperature. To estimate the temperature dependence of Au samples, we modified the cluster ion beam system target chamber to hold a controllable temperature target stage and cooling shields. The outer shield was cooled using liquid nitrogen and the inner shield and the target stage was cooled using a helium compressor (APD Cryogenics, Inc.; Model HC-4 MK2). The liquid nitrogen cooled outer shield ensures that the stage can reach a minimum temperature.

This dissertation includes results obtained for a temperature range from 220.3 K to 473.2 K. The cluster ion beam incident angle and the applied dose were kept constant at 60^o and 3×10^{16} clusters/cm^2, respectively, and the temperature was varied. Figure 6.28 shows atomic force microscope images of nano-ripples formed on Au surfaces as a function of

temperature. Cluster ion-induced nano-ripples disrupts as the surface temperature increases. However, the root mean square surface roughness is highest at room temperature (RT) [Figure 6.29]. Hence the surface instability effects are mainly confined to a temperature range close to RT. Figure 6.30 shows the square root of the height-height correlation function as a variable of the surface temperature. The in-plane length scale corresponds to a first local minimum of $G^{1/2}(d)$. The $G_{min}^{1/2}(d)$ value increase relates to the disruption of ripples. At 473.2 K surface patterning is triggered by thermal diffusion and the main surface features are holes.

The surface gradient decreases with the applied dose. Therefore, ripple formation and mobile atom migration are mainly due to the effective cluster ion-induced diffusion. The surface gradient at RT and 373.2 K are 1.40 nm/mm and 0.70 nm/mm, respectively.

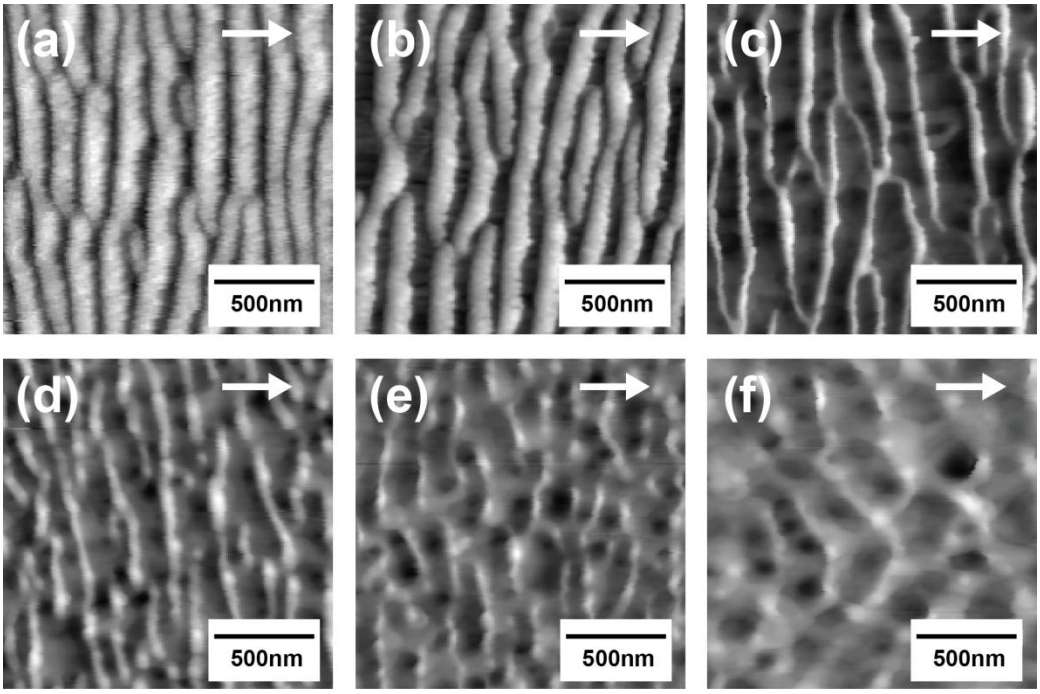

Figure 6.28: Atomic force microscope images of Ar cluster ion beam modified Au surfaces as a function of surface temperature with 60^{o} incident angle, energy of 30 keV per cluster ion and applied dosage of 3×10^{16} cluster/cm^2. The surface temperature: (a) 220.3 K, (b) 297.3 K (room temperature), (c) 373.2 K, (d) 398.2 K, (e) 423.2 K, and (f) 473.2 K. The arrows denote the direction of cluster ions. The scan area for all images is 1.6×1.6 μm^2.

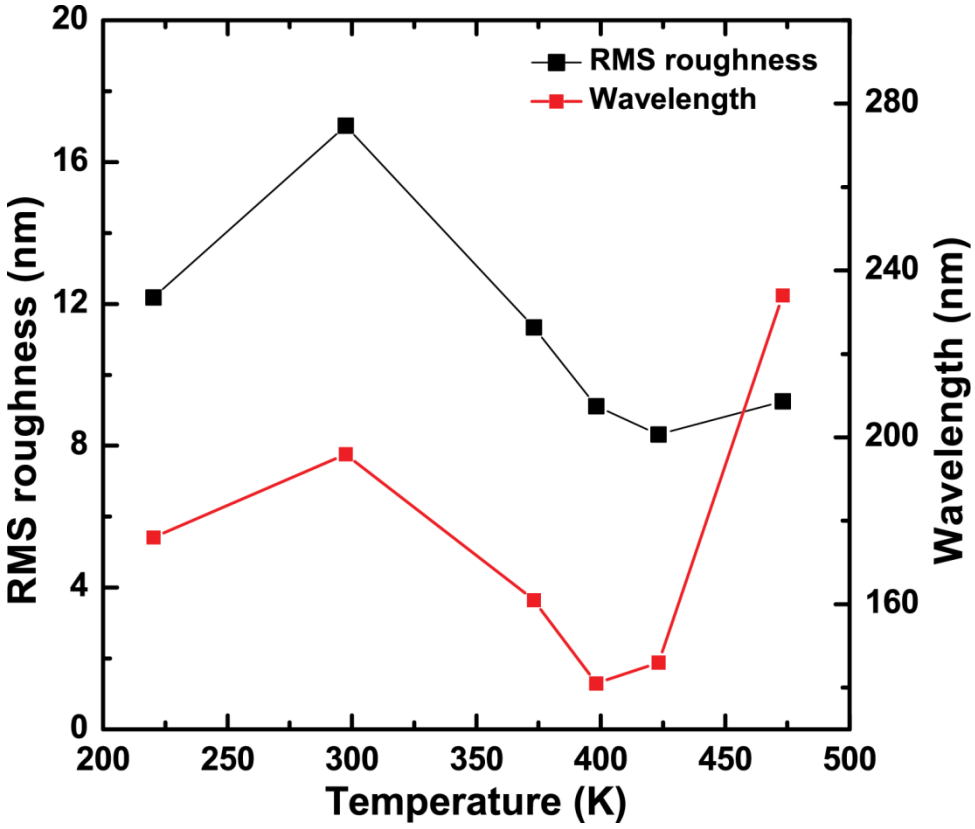

Figure 6.29: RMS roughness and average wavelength as a function of surface temperature at 60^{o} cluster ion incident angle and 3×10^{16} clusters/cm^2 dosage.

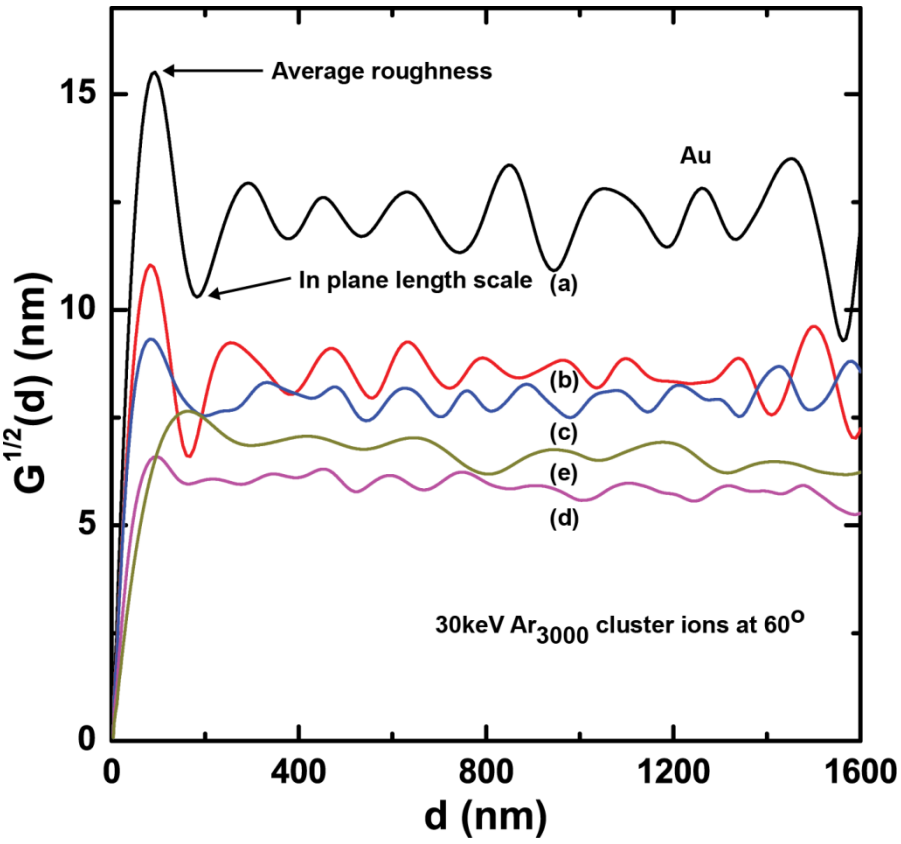

Figure 6.30: Square root of the height-height correlation function of surface temperature at 3×10^{16} clusters/cm^2 dosage with incident angle of 60^o. (i) The first local minimum of $G^{1/2}(d)$ gives a rough measurement of the surface wavelength $d = \lambda$ and (ii) The first maximum is the characteristic surface average roughness $r = G^{1/2}(\lambda/2)$ for a given ripple pattern.

Chapter 7

Applications of Au Nano-ripple Surfaces

Gas cluster ion beam fabricated self-assembled nano-patterns have introduced promising applications in the fields of surface, optical, and bio-medical engineering. A Cluster ion consists about thousands of atoms, which provides more than thousand fold throughput advantage over monomer ions. In this Chapter we discuss two applications of Au nano-ripple surfaces.

7.1 Anisotropic Surface Wetting of Au Nano-ripple Surfaces

Wettability of a solid surface describes the interaction between a water droplet and the surface [98]. It is commonly expressed as the Contact Angle (CA) of the water droplet. CA is defined as the angle between solid-liquid and liquid-vapor interfaces. Depending

on the value of CA, wettability can be categorized as hydrophobic (CA > 90^o) or hydrophilic (CA < 90^o). Surfaces with CA > 150^o are known as superhydrophobic. Applications of such surfaces include self-cleaning [99], anti-sticking, and anti-contamination [100, 101]. Lotus leaves, bamboo tree leaves, rice leaves, and wings of cicada are some examples of naturally existing superhydrophobic surfaces. If CA < 40^o surfaces are superhydrophilic. Possible applications of these surfaces include biological cell adhesion and nerve cell regeneration [102, 103]. CA (θ) is given by Young's equation [104], $\cos\theta = (\gamma_{SV} - \gamma_{SL})/\gamma_{LV}$, where γ_{SV}, $\gamma_{SL}$and γ_{LV} represent surface tensions at solid-vapor, solid-liquid and liquid-vapor interfaces. Young's equation interprets a vapor-liquid-solid phase equilibrium system resides in a flat surface. However, actual surfaces include nano-micro structures that influence CA measurements. This CA is known as the apparent CA, which is always larger than θ for hydrophobic surfaces.

CA dependence of surface roughness can be described qualitatively by the Wenzel [105] and Cassie-Baxter [106] models. The Wenzel state assumes that the water droplet homogeneously covers the rough surface underneath the droplet [Figure 7.1 (a)]. In that case the apparent CA (θ_W) is given by, $\cos\theta_W = r\cos\theta$, here r denotes the surface roughness factor. For a rough surface r is always greater than 1. When r increases CA and CA hysteresis increase up to a value (r = 1.7 [98]) where the water droplet suspends on the pattern due to vapor trapped between surface features – Cassie-Baxter state [Figure 7.1 (b)] and CA hysteresis decreases with increasing roughness. The apparent CA (θ_c) at this state is only a dependent of the solid fraction, f, which is defined as the

fraction of solid surface area wet by the water droplet. According to Cassie-Baxter model apparent CA is given by, $\cos\theta_c = f\left(1 + r_f \cos\theta\right) - 1$. When solid fraction is 1, $r_f = r$ and $\theta_c = \theta_w$.

Wettability studies of nano-rippled Au surfaces shows that with slight changes in cluster ion beam bombardment parameters are efficiently modifying water – surface interactions. Figure 7.2 (a) shows surface area variation as a function of cluster ion beam incident angle for a nano-rippled Au surface bombarded with 1×10^{16} cluster/cm^2 dosage. The surface area percentage and hysteresis were highest at 60^o. Accordingly apparent contact angle was highest at 60^o as shown in Figure 7.2 (b). Au surfaces were tested for CA immediately after cluster ion beam bombardment and without further chemical modifications. CA increases with cluster ion beam applied dosage due to increase in surface roughness factor [Figures 7.2 (c) and (d)]. Surface contaminates (carbon and oxygen – Chapter 6) may influence the CA measurements, if samples are left exposed to ambient environments.

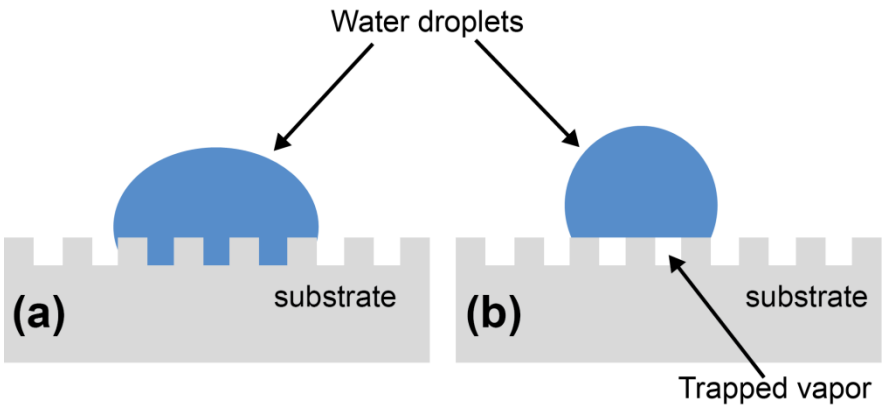

Figure 7.1: Water droplet behavior on a rough surface. (a) Wenzel state: water droplet penetrates completely into the pattern, (b) Cassie-Baxter state: water droplet suspends on the pattern.

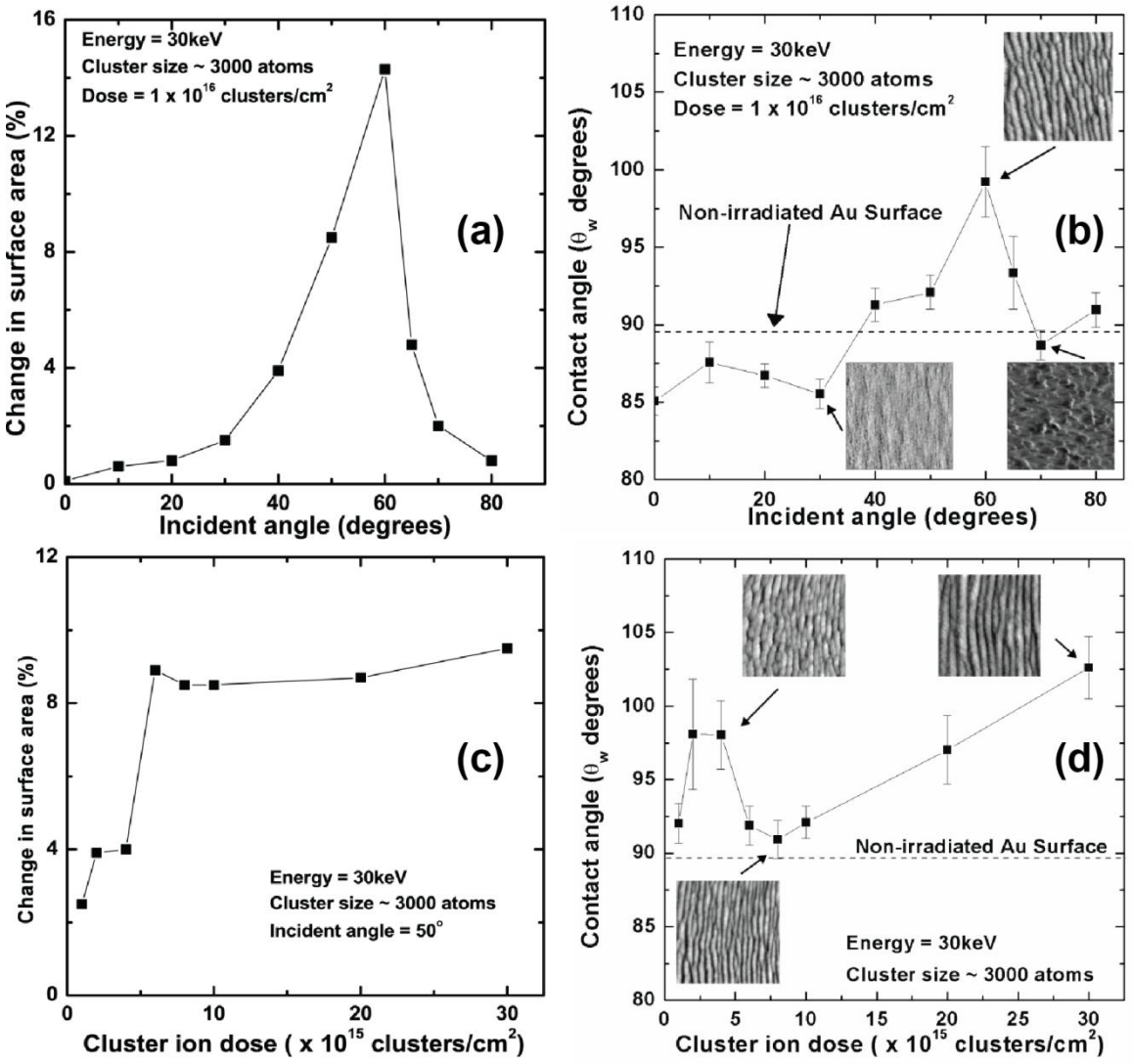

Figure 7.2: (a) The percentage of surface area increase compared to a flat surface measured as a function of Ar cluster ion beam incident angles for 1×10^{16} clusters/cm^2 dosage, (b) Contact angle of a water droplet on Au surface as a function of the cluster ion incident angle measured from the surface normal. The size of the water droplet was 1 μL, (c) The percentage of surface area increase compared to a flat surface measured as a function of Ar cluster ion beam dosage at 50^o incident angle, and (d) corresponding contact angle measurement of a water droplet.

Surface nano-ripple patterns become highly oriented with applied cluster ion beam dosages (as discussed in Chapter 6). When a water droplet is placed on these one-dimensional (1D) nano-ripple structures, it involves in an inhomogeneous wetting [107, 108]. This inhomogeneity is entirely due to liquid – solid surface contact line facing physical discontinuities on the surface. Figure 7.3 (a) and (b) shows water droplets placed on a rippled surface and contact angles were measured in x and y directions respectively. x corresponds to the direction perpendicular to the ripples and y-direction is parallel to ripples. Figure 7.3 (c) shows the surface tested for CA measurements, which was prepared by bombarding with Ar cluster ion dose of 3×10^{16} clusters/cm^2 and the incident angle of the beam was 60^o from the surface normal. The apparent CA in the x-direction showed θ_x=101^o and in the y-direction it was only θ_y= 92^o. Then the angle difference $\theta_x - \theta_y$= 9^o, is called the angle of wetting. Figure 7.3 (d) shows the water droplet formed on the 1D ripple pattern. When the liquid spreading was measured for the 1 μL droplet, top view showed an elliptical shape of the drop. In x direction contact line was measured 2.7 mm and in y-direction line it was 3.3 mm. The physical anisotropy phenomenon introduces a unique directional flow of water on surface, which can be applied as directional self-cleaning surfaces.

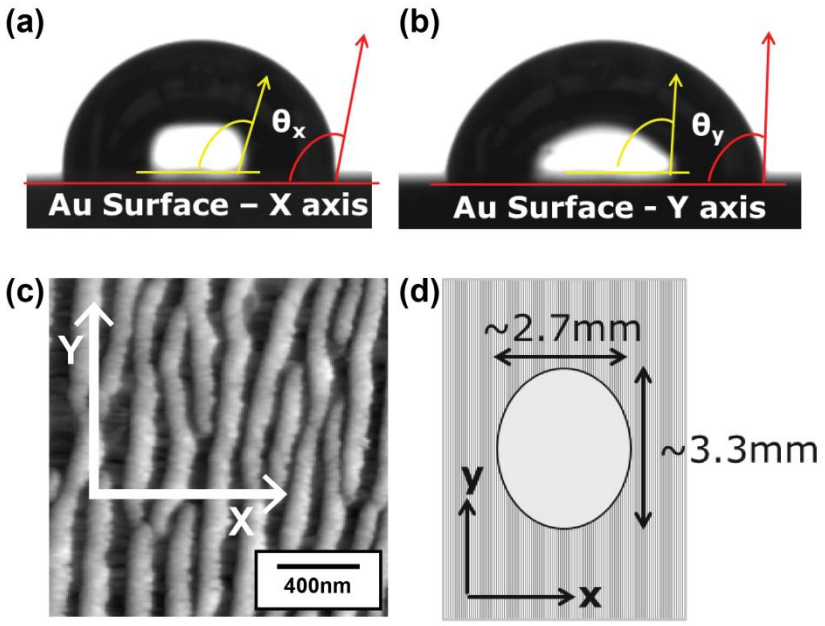

Figure 7.3: (a) and (b) are water droplets placed on a ripple surface and contact angles are measured in x and y directions respectively using static sessile water droplet method. x-direction corresponds to the direction perpendicular to ripples and y-direction is considered parallel to ripples. (c) Contact angle measurements were carried out on a surface bombarded with Ar cluster ion beam 3×10^{16} clusters/cm^2 and the incident angle of the beam was 60^o. The contact angle measured in x-direction was 101^o and in y-direction it was 92^o. (d) A schematic diagram of anisotropic water droplet formed on a one dimensional ripple pattern. The 1 μL water droplet spread 2.7 mm in the x-direction and spread 3.3 mm parallel to ripples.

7.2 Surface Plasmon Resonance of Metallic Nano-ripples

A plasmon is a quantized bulk plasma oscillation of electron in a metallic solid [109]. Plasmons that are confined to a surface of a metal are called surface plasmons [110]. If the surface consists metal nano-particles [typically Au or Ag], these particles interact strongly with white light and creates localized electromagnetic fields that produce intense incident light scattering around a resonance wavelength. This is called localized surface plasmon resonance. These enhancements have useful applications such as surface-enhanced Raman scattering [111], optical waveguides [112], bio-labels [113], and biosensors [114].

Scattering of incident light to produce resonance wavelengths from a rippled surface can be understood by assuming that the ripple wave vector supplies the required momentum to incident photon such that both energy and momentum is conserved when exciting a surface plasmon [Figure 7.4]. However, the main issue arising here is that how to compare energy, momentum and wave vector of the incident photon to that of surface plasmon [115]. The nano-ripple surface can be considered as a diffraction grating and following a derivation similar to Wood's anomaly [116], we can estimate effects of ripple features and azimuthal angle dependence of light incident on the surface. Consider the case where a planar wave is incident onto the rippled surface at a polar angle (α) and an azimuthal angle (β) with respect to the coordinate system [Figure 7.5], here x-direction is perpendicular to the nano-ripples. The ripple wave vector is given by $\boldsymbol{K_r} = (2\pi/l)\hat{\boldsymbol{x}}$,

where l is the period of the nano-ripples and $\hat{x}$ is the unit vector perpendicular to the nano-ripples and lying on the surface.

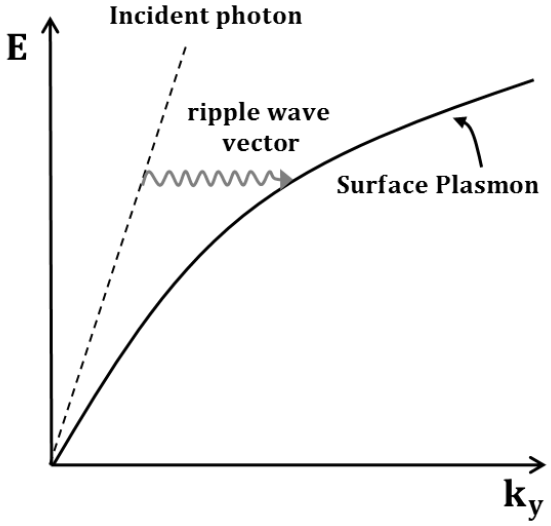

Figure 7.4: The dispersion curve diagram. k_y the component of the wave vector in the plane of the ripples

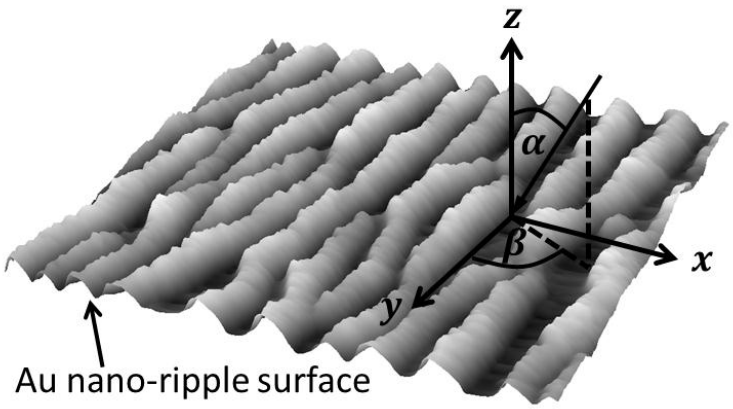

Figure 7.5: A plane wave is incident onto a nano-rippled surface at a polar angle and an azimuthal angle with respect to the coordinate system. Ripples are perpendicular to the x direction.

For conservation of momentum, equalize the surface plasmon wave vector ($\boldsymbol{K_{SP}}$) to the sum of the incident photon wave vector ($\boldsymbol{K_i}$) and integral multiple of the ripple wave vector ($\boldsymbol{K_r}$). Thus,

$$\boldsymbol{K_{SP}} = \boldsymbol{k_i} + m\boldsymbol{K_r} \tag{7.1}$$

where m is an arbitrary integer which depends on the ripple dimensions. The frequency dependent surface plasmon wave vector [117] is given by,

$$\boldsymbol{K_{SP}} \cong \left(\frac{\epsilon_d \epsilon'_m}{\epsilon_d + \epsilon'_m}\right)^{1/2} k_o \hat{\boldsymbol{k}}_{\boldsymbol{SP}} \tag{7.2}$$

where, ϵ_d is the dielectric constant of a medium (with n_d is the index of refraction and $\epsilon_d = n_d^2$) above nano-ripples, $\epsilon'_m$is the real part of the dielectric constant of the metal, and $k_o = \omega/c$ is the free space wave vector of the incident photon with ω angular frequency and c is the speed of light. Also from Figure 7.5,

$$\boldsymbol{k_i} + m\boldsymbol{K_r} = n_d k_o[(\sin\alpha \sin\beta)\hat{\boldsymbol{x}} + (\sin\alpha \cos\beta)\hat{\boldsymbol{y}}] + \frac{2\pi m}{l}\hat{\boldsymbol{x}} \tag{7.3}$$

Therefore, the resonant angle for incident photons is obtained by taking the magnitudes of equation (7.1) with values from equations (7.2) and (7.3),

$$(n_d \sin\alpha)^2 + \frac{2mn_d\lambda}{l}\sin\alpha \sin\beta + \left(\frac{m\lambda}{l}\right)^2 = \frac{\epsilon_d \epsilon'_m}{\epsilon_d + \epsilon'_m} \tag{7.4}$$

Consider the situation where $\beta = 90^o$, i.e. incident photons are perpendicular to the ripples. Then equation (7.4) simplifies to,

$$\sin\alpha = -\left(\frac{m\lambda}{n_d l}\right) \pm \left(\frac{\epsilon'_m}{\epsilon_d + \epsilon'_m}\right)^{1/2} \quad (7.5)$$

Thus for a fixed incident angle (α), the intensity of the reflecting spectrum of white light can be collected and strong resonance effect will appear for transverse magnetic polarization. Figure 7.6 (a) – (e) shows surface plasmon resonance wavelength spectrum for nano-rippled Au surfaces. When Ar cluster ion angle of incidence change from 60^o to 70^o the nano ripple wavelength increases from 195 nm to 217 nm for 3×10^{16} clusters/cm^2 dosage. The measured surface plasmon resonance wavelength these to surfaces changed from 792 nm to 815 nm. This is a red-shift in the scattering light spectrum. The resonance peak becomes sharper when the ripples are well ordered. For a non-bombarded Au surface a clear resonance peak was not observed [Figure 7.6 (a)]. Since the surface roughness depends on the applied dose we saw a blue-shift in surface plasmon resonance peak for samples bombard at 60^o with 2×10^{16} clusters/cm^2 dosage, 773 nm. Also, surface plasmon resonance dependence on the type of metal used, for instants, Ag nano-ripples shows a blue shift in surface plasmon resonance, 635 nm [Figure 7.6 (f)] compared to Au nano-rippled surface (λ = 773 nm) Ar cluster ions bombarded with 2×10^{16} clusters/cm^2 dosage. The second case where the plane of incidence of light is parallel to the ripples, i.e., $\beta = 0^o$, from equation (7.4),

$$\sin\alpha = \left[\left(\frac{\epsilon'_m}{\epsilon_d + \epsilon'_m}\right) - \left(\frac{m\lambda}{n_d l}\right)^2\right]^{1/2} \quad (7.6)$$

For the Ar cluster ion bombarded nano-rippled sample with 70^o incident angle, 3×10^{16} clusters/cm^2 dosage for white light incident parallel to the ripple plane did not present

surface plasmon resonance wavelength as shown in Figure 7.6 (e).

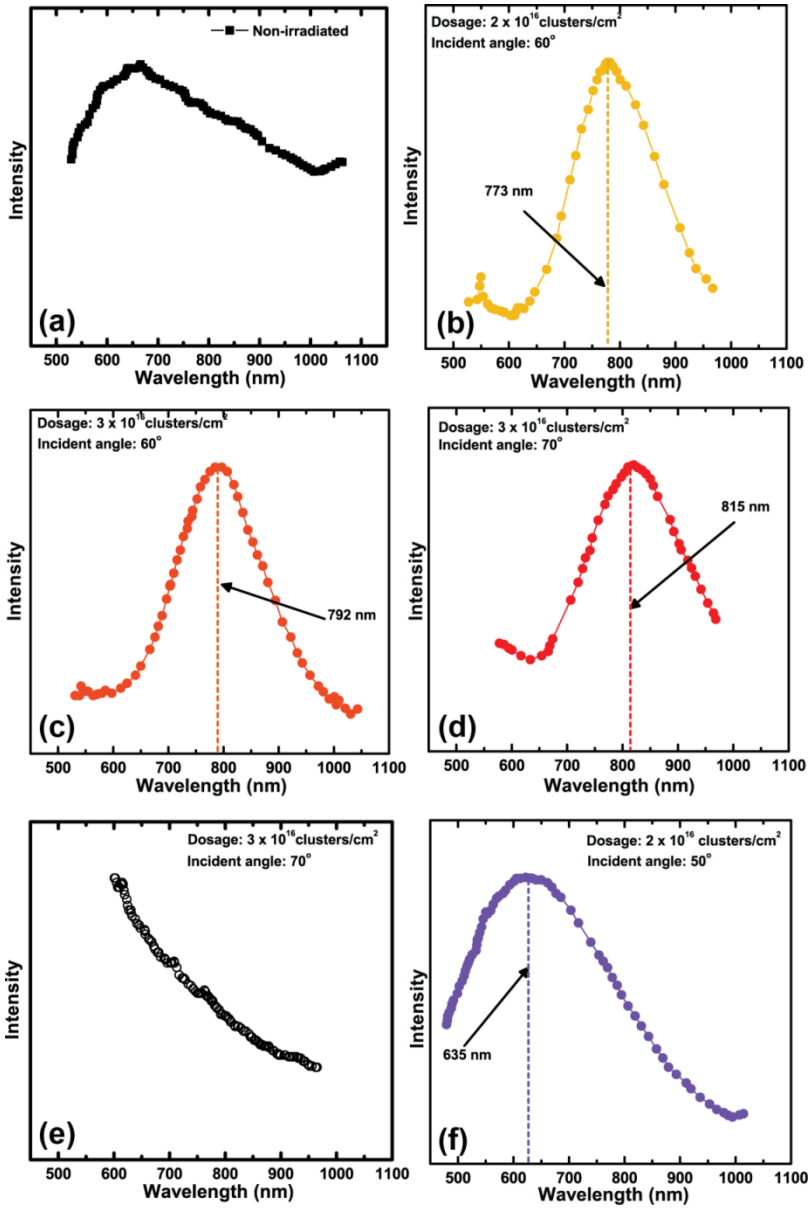

Figure 7.6: (a) Normalized intensity curve for the scattering of light from a non-bombard Au surface. Surface plasmon resonances of Au nano-ripple surface bombarded with Ar cluster ion beam; (b) – (d) Incident white light was perpendicular to ripples and (e) Incident white light was parallel to ripples. (f) Surface plasmon resonance for Ag nano-ripple surface.

Chapter 8

Summary and Future Directions

8.1 Overview

In summary, the focus of this dissertation was to determine the gas cluster ion-induced surface nano-rippling behavior under variable cluster ion beam parameters; (1) angle of incidence, (2) energy per cluster ion, and (3) dosage. Ar cluster ion consists about 3000 atoms that provide more than thousand fold throughput advantage over a monomer ion. In Chapter 5 I compared cluster and monomer ion-induced surface patterns on Si surfaces. Monomer ion-induced nano-patterning highly rely on the energy, dose, ion current density. The temperature of the target substrate rises up to about 150 ^{o}C and the surface thermal activation plays an important role in monomer ion-induced nano-pattern formation. Cluster ion beam bombardment increases the temperature instantaneously, but overall substrate temperature did not change from the room temperature value of 24.5 ^{o}C. During the cluster ion impact near-surface layer becomes amorphized and main structural

features that forms are nano-ripple patterns perpendicular to the cluster ion beam incident direction.

The surface instability depends on the incident angle of the cluster ion beam. The maximum instability was observed at an incident angle of 70^{o} for a dose of 1×10^{16} clusters/cm^2 for Si substrate. However, geometrical shadowing limits the surface roughness due to saturation with prolonged cluster ion beam bombardment. Saturation of nano-ripples also depends on the angle of incidence of cluster ions. 60^{o} angle of incidence has a higher saturation dose compared at 70^{o}. It was also observed that at a dose of 1×10^{17} clusters/cm^2, nano-ripples have a saw tooth structure at the incident angle of 70^{o}. For 60^{o} angle of incidence, the surface atomic accumulation on the upstream of nano-ripple was high, which led to nano-dune formation at a dose of 1×10^{18} clusters/cm^2.

Furthermore, in Chapter 6 I have investigated Au surface atom evolution with time during off-normal bombardment of Ar cluster ion beam. Atoms undergo several sputtering and diffusional processes on the surface depending on the applied cluster ion beam energy and dose. These processes are (1) continuous sputtering into the vacuum due to high energy collisions, (2) initial re-deposition of atoms, and (3) surface diffusion of atoms. The first process is an independent of applied dosage, thus carries minimum impact on the ripple formation. In the second process, atoms deposit close to the collision site, which acts as a barrier for the next set of sputtering atoms. Even though this starts to develop nan-ripples, ripples become well-ordered and grow due to surface diffusion and upstream sputtering.

The amount of atoms sputtered from the surface depends on the angle of incidence of cluster ions. The ripple height grows exponentially with the incident angle up to a transition angle of 60^o and then drops to a smooth surface at grazing incidence.

Additionally, in Chapter 7, I discussed two applications of Au nano-ripples, where we tested nano-ripple surface wettability for different samples prepared by varying the applied Ar cluster ion beam parameters, such as dose and angle of incidence. The contact angle that is the angle between solid-liquid and liquid-vapor interfaces expresses the degree of wetting of a surface. If CA > 90^o the surface is hydrophobic and CA < 90^o the surface is said to be hydrophilic. Understanding of CA variation with the surface roughness is important for fundamental studies as well as for practical applications. We discovered that for Au surface, CA increases with roughness up to a cluster ion beam bombardment incident angle of 60^o. At grazing incident angles, surface roughness is similar to that of a smooth surface bombarded at 0^o incident angle. Also the surface roughness increases with Ar cluster ion beam dosage. However, this is shown for well-ordered nano-ripple patterns at higher applied doses. The initial uneven variation of the surface roughness and CA are due to ripening process of nano-ripples. The most interesting CA observation of well-ordered nano-ripples was the anisotropic wetting behavior. Results indicated that when CA was measured perpendicular to nano-ripples a higher value of CA is accepted, compared to when measured parallel to nano-ripples. These kinds of surfaces are useful for applications in directional self-cleaning surface, and in biological cell guidance.

We have similarly presented that Au nano-ripple surfaces show a significant surface

plasmon resonance when the incident white light illuminates perpendicular to the nano-ripples. This is due to formation of net charge difference at nano-ripple shorter width. The imbalance in charge is created due to the displacement of conduction electrons in the direction of light incidence and generates a strong localized electromagnetic field that produces intense scattering of light around a resonance wavelength, which is similar to the response shown by a diffraction grating. Off-normal Ar cluster ions produce nano-ripples with variable dimensions, which create red or blue shift depending on the size of nano-ripples and the wavelength of the nano-ripples. When the incident white light is parallel to nano-ripples we do not observe surface plasmon resonance due to the length of nano-ripples receding nano-particle behavior, which weakens localized electromagnetic field. Surface plasmon resonance depends on the dielectric constant of the metal, size and shape of nano-ripples.

8.2 Proposed Future Directions

Majority of this study was spent on cluster ion beam parameter optimization. Thus, in future I suggest following activities for further characterization and development of a theoretical model on cluster ion-induced nano-ripple formation:

- Study cross-sectional transmission electron microscope of nano-ripples to determine amorphization of surfaces and to determine accumulation of atoms on the upstream of ripples.

- Theoretical modeling and simulation of cluster ion-induced nano-ripples for different substrates (metallic, semiconductor, alloy and polymer).
- Characterization of nano-dot formation on metallic surfaces by target rotation and ripple migration investigation by applying obstacles on ripple paths.
- Research chemical and physical effects of cluster ion beam modified surfaces on biological cell adhesion.
- Investigation of anisotropy of nano-ripple parameters on surface wetting and its applications of monolayer coating of surfactants and proteins.
- Study surfaces plasmonic resonance for Ag substrates and evaluate a correlation between nano-ripple wavelength and plasmonic resonance wavelength.
- Optimization of parameters for thermal annealing effects on nano-rippled compound materials and study structural evolution during recrystallization.
- Since nano-ripples become well-ordered at high dosage these surfaces can be used as templates for nano-rod size selection, which is useful for producing nano-sized devices. Studies on this area will lead to efficient method for nano-rod selection.
- Compare macroscopic ripple patterns to nano-ripple patterns by using pattern recognition software to determine the universality of ripple pattern formation.

Bibliography

[1] D. C. Jacobs, "The role of internal energy and approach geometry in molecule/surface reactive scattering", Journal of Physics-Condensed Matter **7** (6), 1023-1045 (1995).

[2] L. Hanley and S. B. Sinnott, "The growth and modification of materials via ion-surface processing", Surface Science **500** (1-3), 500-522 (2002).

[3] P. Jensen, "Growth of nanostructures by cluster deposition: Experiments and simple models", Reviews of Modern Physics **71** (5), 1695-1735 (1999).

[4] C. Xirouchaki, "Surface nanostructures created by cluster-surface impact", Vacuum **73** (1), 123-129 (2004).

[5] W. K. Chu, Y. P. Li, J. R. Liu, J. Z. Wu, S. C. Tidrow, N. Toyoda, J. Matsuo, and I. Yamada, "Smoothing of $YBa_2Cu_3O_{7-\delta}$ films by ion cluster beam bombardment", Applied Physics Letters **72** (2), 246-248 (1998).

[6] H. Chen, S. W. Liu, X. M. Wang, M. N. Iliev, C. L. Chen, X. K. Yu, J. R. Liu, K. Ma, and W. K. Chu, "Smoothing of ZnO films by gas cluster ion beam", Nuclear Instruments & Methods in Physics Research Section B-Beam Interactions with Materials and Atoms **241** (1-4), 630-635 (2005).

[7] X. M. Wang, X. M. Lu, L. Shao, J. R. Liu, and W. K. Chu, "Small cluster ions from source of negative ions by cesium sputtering", Nuclear Instruments & Methods in Physics Research Section B-Beam Interactions with Materials and Atoms **196** (1-2), 198-204 (2002).

[8] J. Krauser, A. K. Nix, H. G. Gehrke, H. Hofsass, C. Trautmann, and A. Weidinger, "Highly conductive ion tracks in tetrahedral amorphous carbon by irradiation with 30 mev c-60 projectiles", New Journal of Physics **13**, 1-13 (2011).

[9] I. Yamada, "New horizons in material processing with ICB", Proceedings of 14th Symposium on Ion Sources Ion-Assisted Technology, Tokyo, Japan, 227-235 (1991).

[10] J. A. Greer, D. B. Fenner, J. Hautala, L. P. Allen, V. DiFilippo, N. Toyoda, I. Yamada, J. Matsuo, E. Minami, and H. Katsumata, "Etching, smoothing, and deposition with gas-cluster ion beam technology", Surface & Coatings Technology **133**, 273-282 (2000).

[11] R. MacCrimmon, J. Hautala, M. Gwinn, and S. Sherman, "Gas cluster ion beam infusion processing of semiconductors", Nuclear Instruments & Methods in Physics Research Section B-Beam Interactions with Materials and Atoms **242** (1-2), 427-430 (2006).

[12] A. R. Kirkpatrick and V. DiFilippo, "Method and system for improving the effectiveness of artificial hip joints by the application of gas cluster ion beam technology", US Patent No. 6,491,800 B2 (2002).

[13] S. Ninomiya, K. Ichiki, H. Yamada, Y. Nakata, T. Seki, T. Aoki, and J. Matsuo, "Precise and fast secondary ion mass spectrometry depth profiling of polymer materials with large ar cluster ion beams", Rapid Communications in Mass Spectrometry **23** (11), 1601-1606 (2009).

[14] Z. Insepov and I. Yamada, "Molecular dynamics study of shock wave generation by cluster impact on solid targets", Nuclear Instruments & Methods in Physics

Research Section B-Beam Interactions with Materials and Atoms **112** (1-4), 16-22 (1996).

[15] H. Chen, F. Chen, X. M. Wang, X. K. Yu, J. R. Liu, K. B. Ma, W. K. Chu, H. H. Cheng, I. S. Yu, Y. T. Ho, and K. Y. Horng, "Smoothing of $Si_{0.7}Ge_{0.3}$ virtual substrates by gas-cluster-ion beam", Applied Physics Letters **87**, 103,504 (2005).

[16] H. Chen, M. N. Iliev, J. R. Liu, K. B. Ma, W. K. Chu, N. Badi, A. Bensaoula, and E. B. Svedberg, "Room-temperature deposition of diamond-like carbon field emitter on flexible substrates", Nuclear Instruments & Methods in Physics Research Section B-Beam Interactions with Materials and Atoms **243** (1), 75-78 (2006).

[17] I. Yamada, J. Matsuo, N. Toyoda, and A. Kirkpatrick, "Materials processing by gas cluster ion beams", Materials Science & Engineering R-Reports **34** (6), 231-295 (2001).

[18] R. A. Bagnold, "The physics of blown sand and desert dunes", Chapman and Hall (1941).

[19] H. Yizhaq, N. J. Balmforth, and A. Provenzale, "Blown by wind: Nonlinear dynamics of aeolian sand ripples", Physica D-Nonlinear Phenomena **195** (3-4), 207-228 (2004).

[20] R. S. Anderson, "Eolian ripples as examples of self-organization in geomorphological systems", Earth-Science Reviews **29** (1-4), 77-96 (1990).

[21] D. A. Rumpel, "Successive aeolian saltation - studies of idealized collisions", Sedimentology **32** (2), 267-280 (1985).

[22] S. Mitha, M. Q. Tran, B. T. Werner, and P. K. Haff, "The grain-bed impact process in aeolian saltation", Acta Mechanica **63** (1-4), 267-278 (1986).

[23] R. S. Anderson, "A theoretical-model for aeolian impact ripples", Sedimentology **34** (5), 943-956 (1987).

[24] L. Prigozhin, "Nonlinear dynamics of aeolian sand ripples", Physical Review E **60** (1), 729-733 (1999).

[25] J. Lindhard and M. Scharff, "Energy loss in matter by fast particles of low charge", Det Kongelige Danske Videnskabernes selskab: Matematisk-fysiske meddeleser **27** (15), 1-31 (1953).

[26] J. F. Ziegler, J. P. Biersack, and U. Littmark, "The stopping and range of ions in solids", Pergamon Press, Inc. (1985).

[27] M. Navez, D. Chaperot, and C. Sella, "Microscopie electronique - etude de lattaque du verre par bombardement ionique", Comptes Rendus Hebdomadaires Des Seances De L Academie Des Sciences **254** (2), 240-248 (1962).

[28] R. M. Bradley and J. M. E. Harper, "Theory of ripple topography induced by ion-bombardment", Journal of Vacuum Science & Technology a-Vacuum Surfaces and Films **6** (4), 2390-2395 (1988).

[29] G. Carter, "The physics and applications of ion beam erosion", Journal of Physics D-Applied Physics **34** (3), R1-R22 (2001).

[30] M. A. Makeev, R. Cuerno, and A. L. Barabasi, "Morphology of ion-sputtered surfaces", Nuclear Instruments & Methods in Physics Research Section B-Beam Interactions with Materials and Atoms **197** (3-4), 185-227 (2002).

[31] D. G. Cahill, "Morphological instabilities in thin-film growth and etching", Journal of Vacuum Science & Technology A **21** (5), S110-S116 (2003).

[32] T. Aste and U. Valbusa, "Ripples and ripples: From sandy deserts to ion-sputtered surfaces", New Journal of Physics **7** (122), 1-23 (2005).

[33] T. K. Chini, D. P. Datta, and S. R. Bhattacharyya, "Ripple formation on silicon by medium energy ion bombardment", Journal of Physics-Condensed Matter **21**, 224,004 (2009).

[34] E. Chason and W. L. Chan, "Spontaneous patterning of surfaces by low-energy ion beams", Materials Science with Ion Beams **116**, 53-71 (2010).

[35] W. L. Chan and E. Chason, "Making waves: Kinetic processes controlling surface evolution during low energy ion sputtering", Journal of Applied Physics **101**, 121,301 (2007).

[36] G. Carter, "The effects of surface ripples on sputtering erosion rates and secondary ion emission yields", Journal of Applied Physics **85** (1), 455-459 (1999).

[37] J. Munoz-Garcia, M. Castro, and R. Cuerno, "Nonlinear ripple dynamics on amorphous surfaces patterned by ion beam sputtering", Physical Review Letters **96**, 086,101 (2006).

[38] W. R. Grove, "VII. On the electro-chemical polarity of gases", Philosophical Transactions of the Royal Society of London **142**, 87-101 (1853).

[39] B. Ziberi, F. Frost, T. Hoche, and B. Rauschenbach, "Ripple pattern formation on silicon surfaces by low-energy ion-beam erosion: Experiment and theory", Physical Review B **72**, 235,310 (2005).

[40] M. Cornejo, B. Ziberi, C. Meinecke, D. Hirsch, J. W. Gerlach, T. Hoche, F. Frost, and B. Rauschenbach, "Self-organized patterning on si(001) by ion sputtering with simultaneous metal incorporation", Applied Physics a-Materials Science & Processing **102** (3), 593-599 (2011).

[41] Y. Yamamura, "Computer-simulation of ionized cluster beam bombardment on a carbon substrate", Nuclear Instruments & Methods in Physics Research Section B-Beam Interactions with Materials and Atoms **45** (1-4), 707-713 (1990).

[42] N. Toyoda, J. Matsuo, and I. Yamada, "The sputtering effects of cluster ion beams", Application of Accelerators in Research and Industry - Proceedings of the Fourteenth International Conference, Pts 1 and 2 (392), 483-486 (1997).

[43] N. Toyoda, H. Kitani, N. Hagiwara, T. Aoki, J. Matsuo, and I. Yamada, "Angular distributions of the particles sputtered with ar cluster ions", Materials Chemistry and Physics **54** (1-3), 262-265 (1998).

[44] E. W. Becker, K. Bier, and W. Henkes, "Strahlen aus kondensierten atomen und molekeln im hochvakuum", Zeitschrift Fur Physik **146** (3), 333-338 (1956).

[45] W. Henkes, "Production of plasma by injection of charged hydrogen clusters", Physics Letters **12** (4), 322-323 (1964).

[46] R. Middleton, "Survey of negative-ions from a cesium sputter source", Nuclear Instruments & Methods **144** (3), 373-399 (1977).

[47] T. G. Dietz, M. A. Duncan, D. E. Powers, and R. E. Smalley, "Laser production of supersonic metal cluster beams", Journal of Chemical Physics **74** (11), 6511-6512 (1981).

[48] G. Gantefor, H. R. Siekmann, H. O. Lutz, and K. H. Meiwesbroer, "Pure metal and metal-doped rare-gas clusters grown in a pulsed-arc cluster ion-source", Chemical Physics Letters **165** (4), 293-296 (1990).

[49] K. Sattler, J. Muhlbach, and E. Recknagel, "Generation of metal-clusters containing from 2 to 500 atoms", Physical Review Letters **45** (10), 821-824 (1980).

[50] G. H. Takaoka, H. Noguchi, and Y. Hironaka, "Production of liquid cluster ions and their application to surface etching", Nuclear Instruments & Methods in Physics Research Section B-Beam Interactions with Materials and Atoms **242** (1-2), 100-103 (2006).

[51] L. D. Landau and E. M. Lifshitz, "Fluid mechanics", Pergamon Press (1959).

[52] H. Dun, B. L. Mattes, and D. A. Stevenson, "Gas-dynamics of a conical nozzle molecular-beam sampling system", Chemical Physics **38** (2), 161-172 (1979).

[53] D. R. Miller, in "Atomic and molecular beam methods, vol. 1", edited by G. Scoles, Oxford University Press (1988).

[54] J. M. Soler, N. Garcia, O. Echt, K. Sattler, and E. Recknagel, "Microcluster growth - transition from successive monomer addition to coagulation", Physical Review Letters **49** (25), 1857-1860 (1982).

[55] O. F. Hagena, "Nucleation and growth of clusters in expanding nozzle flows", Surface Science **106** (1-3), 101-116 (1981).

[56] H. Ashkenas and F. S. Sherman, in "Rarefied gas dynamics, vol. 2", edited by J. H. DeLeeuw, Academic Press (1966).

[57] N. Toyoda, T. Mashita, and I. Yamada, "Nano structure formation by gas cluster ion beam irradiations at oblique incidence", Nuclear Instruments & Methods in Physics Research Section B-Beam Interactions with Materials and Atoms **232**, 212-216 (2005).

[58] W. K. Chu, J. W. Mayer, and M. A. Nicolet, "Backscattering spectrometry", Academic Press (1978).

[59] J. F. Ziegler, J. P. Biersack, and M. D. Ziegler, "Srim: The stopping range of ions in matter", SRIM Co. (2008).

[60] D. V. Morgan, "Channeling: Theory, observation and applications", John Wiley and Sons (1973).

[61] P. Klapetek, D. Necas, and C. Anderson, "Gwyddion 2.24", The Free Software Foundation (2011).

[62] T. Young, "An essay on the cohesion of fluids", Philosophical Transactions of Royal Society of London **95**, 65-87 (1805).

[63] R. N. Wenzel, "Resistance of solid surfaces to wetting by water", Industrial and Engineering Chemistry **28** (8), 988-994 (1936).

[64] A. B. D. Cassie and S. Baxter, "Wettability of porous surfaces", Transactions of the Faraday Society **40**, 546-551 (1944).

[65] C. F. Bohren and D. R. Huffman, "Absorption and scattering of light by small particles", Wiley (1983).

[66] U. Kreibig and M. Vollmer, "Optical properties of metal clusters, vol. 25", Springer (1995).

[67] Q. B. Xu, J. M. Bao, F. Capasso, and G. M. Whitesides, "Surface plasmon resonances of free-standing gold nanowires fabricated by nanoskiving", Angewandte Chemie-International Edition **45** (22), 3631-3635 (2006).

[68] R. Gago, L. Vazquez, R. Cuerno, M. Varela, C. Ballesteros, and J. M. Albella, "Production of ordered silicon nanocrystals by low-energy ion sputtering", Applied Physics Letters **78** (21), 3316-3318 (2001).

[69] S. Habenicht, K. P. Lieb, J. Koch, and A. D. Wieck, "Ripple propagation and velocity dispersion on ion-beam-eroded silicon surfaces", Physical Review B **65**, 115,327 (2002).

[70] A. D. Brown, J. Erlebacher, W. L. Chan, and E. Chason, "Transient topographies of ion patterned si(111)", Physical Review Letters **95**, 056,101 (2005).

[71] B. Ziberi, F. Frost, T. Hoche, and B. Rauschenbach, "Ripple pattern formation on silicon surfaces by low-energy ion-beam erosion: Experiment and theory", Physical Review B **72**, 235,310 (2005).

[72] T. K. Chini, D. P. Datta, and S. R. Bhattacharyya, "Ripple formation on silicon by medium energy ion bombardment", Journal of Physics-Condensed Matter **21**, 224,004 (2009).

[73] A. Keller, R. Cuerno, S. Facsko, and W. Moller, "Anisotropic scaling of ripple morphologies on high-fluence sputtered silicon", Physical Review B **79**, 115,437 (2009).

[74] C. S. Madi, H. B. George, and M. J. Aziz, "Linear stability and instability patterns in ion-sputtered silicon", Journal of Physics-Condensed Matter **21**, 224,010 (2009).

[75] S. K. Garg, V. Venugopal, T. Basu, O. P. Sinha, S. Rath, D. Kanjilal, and T. Som, "Evolution of ripple morphology on Si(100) by 60-keV argon ions", Applied Surface Science **258** (9), 4135-4138 (2012).

[76] S. Park, B. Kahng, H. Jeong, and A. L. Barabasi, "Dynamics of ripple formation in sputter erosion: Nonlinear phenomena", Physical Review Letters **83** (17), 3486-3489 (1999).

[77] T. Aste and U. Valbusa, "Ripples and ripples: From sandy deserts to ion-sputtered surfaces", New Journal of Physics **7** (2005).

[78] J. Munoz-Garcia, M. Castro, and R. Cuerno, "Nonlinear ripple dynamics on amorphous surfaces patterned by ion beam sputtering", Physical Review Letters **96** (8) (2006).

[79] W. L. Chan and E. Chason, "Making waves: Kinetic processes controlling surface evolution during low energy ion sputtering", Journal of Applied Physics **101** (12) (2007).

[80] H. Chen, "Cluster ion beam modification of material surfaces", Ph.D. Dissertation, University of Houston (2006).

[81] H. Kitani, N. Toyoda, J. Matsuo, and I. Yamada, "Incident angle dependence of the sputtering effect of ar-cluster-ion bombardment", Nuclear Instruments & Methods in Physics Research Section B-Beam Interactions with Materials and Atoms **121** (1-4), 489-492 (1997).

[82] D. P. Datta and T. K. Chini, "Coarsening of ion-beam-induced surface ripple in si: Nonlinear effect vs. Geometrical shadowing", Physical Review B **76**, 075,323 (2007).

[83] D. P. Datta and T. K. Chini, "Atomic force microscopy study of 60-keV Ar-ion-induced ripple patterns on Si(100)", Physical Review B **69**, 235,313 (2004).

[84] J. Lapujoulade, "The roughening of metal surfaces", Surface Science Reports **20** (4), 191-249 (1994).

[85] P. Karmakar and D. Ghose, "Nanoscale periodic and faceted structures formation on si(100) by oblique angle oxygen ion sputtering", Nuclear Instruments & Methods in Physics Research Section B-Beam Interactions with Materials and Atoms **230**, 539-544 (2005).

[86] U. Valbusa, C. Boragno, and F. B. de Mongeot, "Nanostructuring surfaces by ion sputtering", Journal of Physics-Condensed Matter **14** (35), 8153-8175 (2002).

[87] H. H. Andersen, "Nonlinear effects in collisional sputtering under cluster impact", Fundamental Processes in Sputtering of Atoms and Molecules (Sput92), 127-153 (1993).

[88] I. Yamada, J. Matsuo, Z. Insepov, T. Aoki, T. Seki, and N. Toyoda, "Nano-processing with gas cluster ion beams", Nuclear Instruments & Methods in Physics Research Section B-Beam Interactions with Materials and Atoms **164**, 944-959 (2000).

[89] J. F. Ziegler, J. P. Biersack, and M. D. Ziegler, "Srim: The stopping and range of ions in matter", SRIM Co. (2008).

[90] N. Toyoda and I. Yamada, "Cluster size dependence of surface morphology after gas cluster ion bombardments", Nuclear Instruments & Methods in Physics Research Section B-Beam Interactions with Materials and Atoms **266** (10), 2529-2532 (2008).

[91] T. Aoki, T. Seki, and J. Matsuo, "Molecular dynamics study of crater formation by core-shell structured cluster impact", Nuclear Instruments & Methods in Physics Research Section B-Beam Interactions with Materials and Atoms **282**, 29-32 (2012).

[92] P. Sigmund, "Theory of sputtering. I. Sputtering yield of amorphous and polycrystalline targets", Physical Review **184** (2), 383-416 (1969).

[93] G. K. Wehner and D. Rosenberg, "Angular distribution of sputtered material", Journal of Applied Physics **31** (1), 177-179 (1960).

[94] M. I. Rabinovich, A. B. Ezersky, and P. D. Weidman, "The dynamics of patterns", World Scientific (2000).

[95] G. Ehrlich and F. G. Hudda, "Atomic view of surface self-diffusion - tungsten on tungsten", Journal of Chemical Physics **44** (3), 1039-1049 (1966).

[96] Schwoebe.Rl, "Step motion on crystal surfaces .2.", Journal of Applied Physics **40** (2), 614-618 (1969).

[97] J. Munoz-Garcia, R. Cuerno, and M. Castro, "Coupling of morphology to surface transport in ion-beam irradiated surfaces: Oblique incidence", Physical Review B **78**, 205,408 (2008).

[98] X. M. Li, D. Reinhoudt, and M. Crego-Calama, "What do we need for a superhydrophobic surface? A review on the recent progress in the preparation of superhydrophobic surfaces", Chemical Society Reviews **36** (8), 1350-1368 (2007).

[99] R. Blossey, "Self-cleaning surfaces - virtual realities", Nature Materials **2** (5), 301-306 (2003).

[100] W. Barthlott and C. Neinhuis, "Purity of the sacred lotus, or escape from contamination in biological surfaces", Planta **202** (1), 1-8 (1997).

[101] A. Lafuma and D. Quere, "Superhydrophobic states", Nature Materials **2** (7), 457-460 (2003).

[102] H. Tsuji, P. Sommani, T. Kitamura, M. Hattori, H. Sato, Y. Gotoh, and J. Ishikawa, "Nerve-cell attachment properties of polystyrene and silicone rubber modified by carbon negative-ion implantation", Surface & Coatings Technology **201** (19-20), 8123-8126 (2007).

[103] T. Limongi, F. Cesca, F. Gentile, R. Marotta, R. Ruffilli, A. Barberis, M. Dal Maschio, E. M. Petrini, S. Santoriello, F. Benfenati, and E. Di Fabrizio, "Nanostructured superhydrophobic substrates trigger the development of 3d neuronal networks", Small, 201,201,377 (2012).

[104] T. Young, "An essay on the cohesion of fluids", Philosophical Transactions of the Royal Society of London **95**, 65-87 (1805).

[105] R. N. Wenzel, "Resistance of solid surfaces to wetting by water", Industrial & Engineering Chemistry **28** (8), 988-994 (1936).

[106] A. B. D. Cassie and S. Baxter, "Wettability of porous surfaces", Transactions of the Faraday Society **40** (0), 546-551 (1944).

[107] H. Kusumaatmaja, R. J. Vrancken, C. W. M. Bastiaansen, and J. M. Yeomans, "Anisotropic drop morphologies on corrugated surfaces", Langmuir **24** (14), 7299-7308 (2008).

[108] D. Xia, L. M. Johnson, and G. P. López, "Anisotropic wetting surfaces with one-dimesional and directional structures: Fabrication approaches, wetting properties and potential applications", Advanced Materials **24** (10), 1287-1302 (2012).

[109] D. Pines and D. Bohm, "A collective description of electron interactions: Ii. Collective vs individual particle aspects of the interactions", Physical Review **85** (2), 338-353 (1952).

[110] R. H. Ritchie, "Plasma losses by fast electrons in thin films", Physical Review **106** (5), 874-881 (1957).

[111] S. Nie and S. R. Emory, "Probing single molecules and single nanoparticles by surface-enhanced raman scattering", Science **275** (5303), 1102-1106 (1997).

[112] W. L. Barnes, A. Dereux, and T. W. Ebbesen, "Surface plasmon subwavelength optics", Nature **424** (6950), 824-830 (2003).

[113] S. Schultz, D. R. Smith, J. J. Mock, and D. A. Schultz, "Single-target molecule detection with nonbleaching multicolor optical immunolabels", Proceedings of the National Academy of Sciences of the United States of America **97** (3), 996-1001 (2000).

[114] Y. W. C. Cao, R. Jin, and C. A. Mirkin, "Nanoparticles with raman spectroscopic fingerprints for DNA and rna detection", Science **297** (5586), 1536-1540 (2002).

[115] D. Sarid and W. Challener, "Modern introduction to surface plasmons: Theory, mathematica modeling, and applications", Cambridge University Press (2010).

[116] R. W. Wood, "Anomalous diffraction gratings", Physical Review **48** (12), 928-936 (1935).

[117] J. R. Sambles, G. W. Bradbery, and F. Z. Yang, "Optical-excitation of surface-plasmons - an introduction", Contemporary Physics **32** (3), 173-183 (1991).

[118] P. Sigmund, "Mechanism of surface micro-roughening by ion-bombardment", Journal of Materials Science **8** (11), 1545-1553 (1973).

[119] R. Cuerno, H. A. Makse, S. Tomassone, S. T. Harrington, and H. E. Stanley, "Stochastic-model for surface erosion via ion sputtering - dynamical evolution from ripple morphology to rough morphology", Physical Review Letters **75** (24), 4464-4467 (1995).

[120] R. Cuerno and A. L. Barabasi, "Dynamic scaling of ion-sputtered surfaces", Physical Review Letters **74** (23), 4746-4749 (1995).

[121] R. I. Schwoebel, "Step motion on crystal surfaces .2.", Journal of Applied Physics **40** (2), 614-618 (1969).

[122] G. Costantini, S. Rusponi, F. B. de Mongeot, C. Boragno, and U. Valbusa, "Periodic structures induced by normal-incidence sputtering on ag(110) and ag(001): Flux and temperature dependence", Journal of Physics-Condensed Matter **13** (26), 5875-5891 (2001).

[123] J. Villain, "Continuum models of crystal-growth from atomic-beams with and without desorption", Journal De Physique I **1** (1), 19-42 (1991).

Appendix A

Brief Description of Models Associated with Monomer Ion-induced Surface Patterns

A.1 The Bradley and Harper Model for Surface Sputtering-based Pattern Formation

The Bradley and Harper model [28] on ripple formation on amorphous materials takes Sigmund's theory of sputtering [118] as a starting point. According to Sigmund's theory, atom sputtering is caused by a physical process. This is only applicable for amorphous materials. The probability for an atom to be sputtered from the surface is proportional to the interstitial energy transfer from the neighboring atom which was bombarded with an

ion. For example, consider point A in Figure A.1. When an ion collides with an atom located at point A energy is transferred to the nearest neighbor atom and if the energy is sufficient, that atom is sputtered from the surface. The amount of energy required must be greater than the surface binding energy of the material. Using this concept, Bradley and Harper explained in their derivation of the linear partial differential equation that when ions are incident normal to the surface, the amount of energy transferred from point ***A*** to the nearest neighbor atom downstream is larger than the energy transfer from point ***B*** to the nearest neighbor atom upstream. That is atoms in troughs sputter more compared to atoms on surface mounts. However, the amount of ions colliding at point ***B*** is greater than point ***A***. At grazing angles sputtering is greater at point ***B*** than at point ***A***. Thus, according to Bradley and Harper model at grazing incidence and periodic patterns perpendicular to the beam direction does not form due to limiting of surface instability. The model with this curvature dependent sputtering idea put forward by Sigmund, considers simultaneous surface relaxation towards creating a flat surface by surface diffusion. Thereby, the surface height is given by,

$$\frac{\partial h}{\partial t} = -v_o(\theta) + v_o'(\theta)\frac{\partial h}{\partial x} + v_x(\theta)\frac{\partial^2 h}{\partial x^2} + v_y(\theta)\frac{\partial^2 h}{\partial y^2} - D^T\nabla^4 h \qquad (A.1)$$

Here, $v_o(\theta) = (f/N)Y_o(\theta)\cos\theta$ is the sputtering rate for a flat surface when the energetic ion undergoing an elastic collision is normal to the surface. This is a simplification of Sigmund's curvature dependent sputtering rate equation.

$$v(\theta, R) \cong \frac{f}{N}Y_o\left[\cos\theta + \Gamma_1(\theta)\frac{a}{R}\right] \qquad (A.2)$$

where f is the ion flux, N is the number of atoms per unit volume in the amorphous solid, a is the depth of energy deposition, θ is the incident angle from the measured normal and the coefficient $\Gamma_1(\theta)$ is given [28]. The $v_x(\theta)$ and $v_y(\theta)$ terms can be negative or positive depending on the angle of incidence of the ion. The last term of the equation (A.1) describes the surface relaxation by thermal activation with:

$$D^T = \frac{2D\gamma v}{N^2 k_B T} \qquad (A.3)$$

where D, γ, v, T and K_B represent the surface self-diffusivity, the free energy per unit area, number of atoms per unit area moving across the surface, temperature and the Boltzmann constant, respectively. For the surface instability the partial differential equation can be solved using Fourier techniques and solution is discussed in [28].

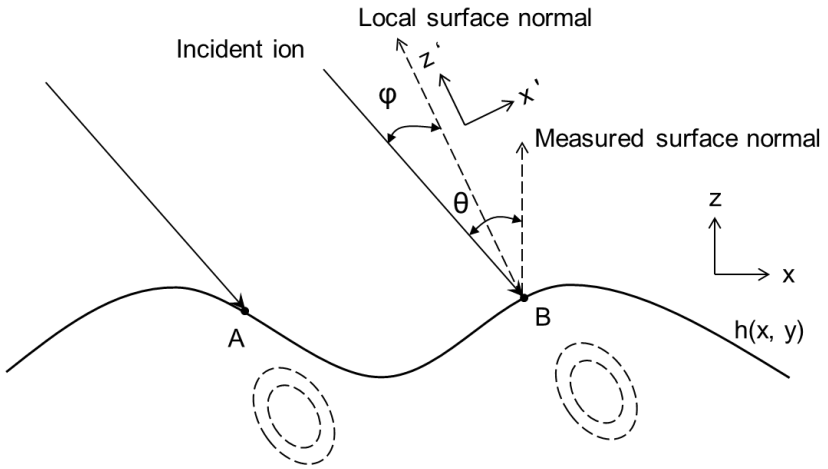

Figure A.1: Coordinate system as described by Bradley and Harper model for ion bombardment on a surface. The ellipses denote the energy deposited due to a single collision event. (The energy distribution is Gaussian) According to Sigmund's theory, the probability for an atom to be sputtered from the target material is proportional to the total energy received from the neighboring atom due to ion bombardment. The laboratory coordinate system is (x, y, z) and the local surface area coordinates are denoted by ($x^{/}$, $y^{/}$, $z^{/}$).

A.2 The Makeev, Cuerno, and Barabási Model on Surface Sputtering and Ion-induced Effective Surface Diffusion

The Bradley and Harper model was derived to adapt ripple formation on amorphous surfaces and neglected higher order non-linear terms in the partial differential equation. Consequently the model cannot explain pits and mounds formation, crystal structure dependence and ripple amplitude saturations [32, 33, 35]. Cuerno et al. [119, 120] and Makeev et al. [30] added non-linear terms into the Bradley and Harper model: (1) Slope dependent non-linear term, (2) Ion-induced effective surface diffusion, and (3) A random ion flux term. The effective surface diffusion term depends on the preferential sputtering of the surface, which portrays surface reorganization in an average height coordinate system. Thus, the modified partial differential equation is given by,

$$\partial_t h = v_{i,j}\nabla^2 h - D^I_{i,j} h + \frac{\lambda_{i,j}}{2}(\nabla h)^2 + \eta(x,y,t) \qquad (A.4)$$

Numerical calculations done on equation (A.4) [76] show an initial linear ripple growth up to a critical time (t_c) and beyond this time ripple growth becomes non-linear depending on the sign of the product of coefficients λ_x and λ_y. The t_c is given by [76],

$$t_c \sim \frac{D^I}{v^2} ln \frac{v}{\lambda} \qquad (A.5)$$

where, v, D^I and λ are perpendicular to the direction of ripples. The main differences between equations (A.1) and (A.4) are absence of the zeroth order term in equation (A.4) and instead of the thermally activated diffusion term (D^T), equation (A.4) includes ion-induced effective diffusion term (D^I). This model neglects the high beam current density heating of substrates.

A.3 The Shadowing Effect Model

The linear growth of ripples with time due to monomer ion beam bombardment is predicted by the Bradley and Harper model and the linear Makeev, Cuerno and Barabási model. According to the Makeev, Cuerno and Barabási model the non-linear regime surface structures depend on the sign of the term $\lambda_x\lambda_y$ in equation (A.4) and this is yet to be proven experimentally. The ripple height saturation with time for monomer ion bombardment is also explained using geometrical shadowing of ion beam by Carter [36]. The argument put forward by this model is once an ion beam incident onto the surface at an angle, existing surface features may block or shadow the ion beam on the upstream of surface features depending on the slope of the ripples. Figure A.2 (b) shows the limiting slope angle of surface ripples; beyond this beam becomes shadowed. The Shadowing effect is significant at grazing incident angles [Figure A.2 (c)]. The result of prolonged bombardment at grazing angles leads to saw tooth like structures and saturation as shown in Figure A.2 (d).

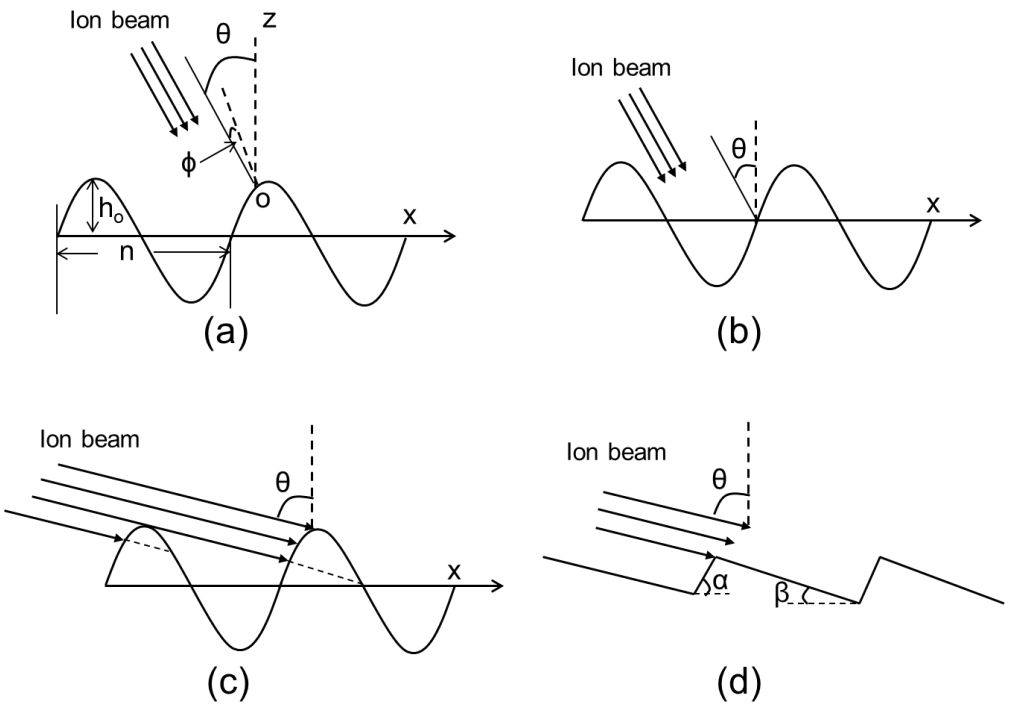

Figure A.2: Sketch of the geometrical shadowing effect on a sinusoidal surface profile. Since the sine wave is described by $h = h_o \sin(2\pi x/n)$: (a) complete surface is exposed by ion beam, (b) Critical surface slope (h_o/n) at angle θ, where shadowing occurs, (c) grazing incidence of ions shadowed by surface peaks and surface starts to develop saw tooth like structures, and (d) completely formed saw tooth structures with α and β upstream and downstream surface inclination angles.

This model assumes two-dimensional (xOz plane) fluctuations of atoms perpendicular to the ripples [figure 2.4 (a)]. The height evolution is given by

$$\partial_t h = \left(\frac{J}{N}\right) Y(\phi) \cos(\phi) \sec(\theta - \phi) \qquad (A.6)$$

where, J, N and $Y(\phi)$ are the ion flux density, target atomic density and the rate of sputtering of the surface, respectively. The local surface gradient is $\delta h/\delta x = \tan(\theta - \phi)$. For a sinusoidal ripple pattern; the surface height can be described by

$$h = h_o \cos\left(\frac{2\pi x}{n}\right) \qquad (A.7)$$

where h_o is the amplitude of ripples and n is the wavelength. When the amplitude to wavelength ratio increases the maximum pattern slope increases and as a consequence the local surface angle (φ) decreases and eventually beam shadowing processes become dominant creating saturation of ripples. To avoid ion beam shadowing, beam conditions should satisfy the following relation

$$\tan\left(\frac{\pi}{2} - \theta\right) \geq \frac{2\pi h_o}{n} \qquad (A.8)$$

A.4 The Diffusion Barrier Model (Ehrlich-Schwoebel Barrier)

Ehrlich-Schwoebel barrier [95, 121] triggered mass flow is used to study patterns formed due to sputtering on metallic surfaces such as pits, mounds, and ripples oriented with the crystal structure [122, 86]. The Bradley and Harper model is unable to predict these structures [35]. Originally the Ehrlich-Schwoebel barrier model was proposed for roughening process of epitaxial growth by Villain [123]. According to the model the Ehrlich-Schwoebel barrier induces adatom and vacancies which diffuse across step edges (Figure A.3) and cause nucleation to produce surface roughness. The model demonstrates ripple formation in crystalline directions [35]. Evidently, for amorphous surfaces this method is not applicable [83].

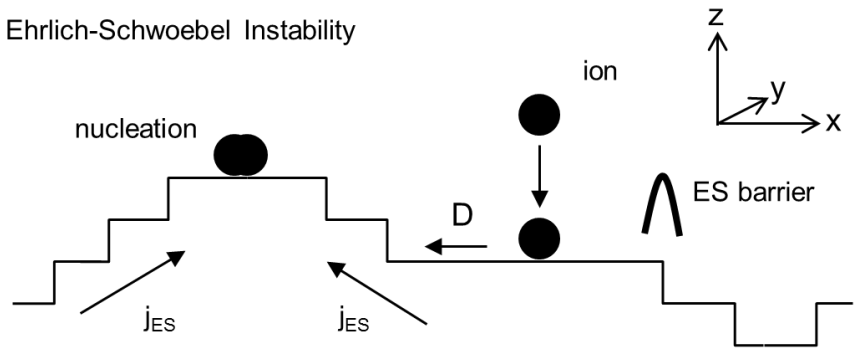

Figure A.3: Schematic diagram of Ehrlich-Schwoebel barrier instability on a crystalline metallic surface. Notation J_{ES} is the mass current due to Ehrlich-Schwoebel barrier.

A.5 The Munoz-García, Castro, and Cuerno Model on Viscous Hydrodynamic Flow of Surface Adatoms

The hydrodynamic approach [37] considers off-normal amorphous surface sputtering. According to the model part of the sputtered atoms redeposit into the beam current flow of the adatoms, and undergo surface diffusion relaxation. The main difference in this model is the reflection of a re-deposition fraction (ϕ). Also, a layer of viscous mobile surface atoms is taken into account. The height evolution equation is given by,

$$\partial_t h = \sum_{i=x,y} \left\{ -v_i \partial_i^2 h + \lambda_i^{(I)} (\partial_i h)^2 \right\} + \sum_{i,j=x,y} \left\{ -K_{ij} \partial_i^2 \partial_j^2 h + \lambda_{ij}^{(II)} \partial_i^2 \left(\partial_j h \right)^2 \right\} \qquad (A.9)$$

Similar to the Makeev, Cuerno, and Barabási model, the continuous sputtering term is neglected, because of its non-involvement in pattern formation. Here, v_i and K_{ij} are sputtering rate and surface diffusion terms, respectively. K_{ij}, $\lambda_i^{(I)}$, and $\lambda_{ij}^{(II)}$ depend on the

redeposition fraction (ϕ), ion beam angle of incidence (θ) and on the average fraction of mobile atoms that contribute to surface smoothing. Introduction of non-linear terms $\lambda_i^{(I)}$, and $\lambda_{ij}^{(II)}$ prompts ripple dynamic features such as saturation, wavelength increase, ripple rotation, and kinetic roughening.